PLASMONICS IN SEMICONDUCTORS

by

Jan Chochol

VŠB - Technical University of Ostrava

2017

To my wife.

Contents

List of Figures

List of Tables

Abstract

This thesis establishes a mathematical, physical and experimental framework for description, characterization, and application of semiconductor plasmonic properties. Plasmonic phenomena in semiconductors are found in the Terahertz and far-infrared domain, where they have the potential to improve sensors or be the basis of novel devices. III-V semiconductor samples (GaAs, InP, InSb, and InAs) with various doping were analyzed spectroscopically in broad spectral range. Fourier Transform Infrared Spectroscopy together with Terahertz time-domain spectroscopy were used for characterization of the free carrier (plasmonic) and lattice (phononic) optical properties of the samples. The Drude-Lorentz model was used to describe these properties, with the addition of magneto-optical (MO) effects. High mobility semiconductors (InSb and InAs) exhibit huge free carrier magneto-optical effect for small external magnetic field. These measurements were compared to electric Hall effect measurement using Van der Pauw method.

Based on the spectroscopic and MO characterization of the samples, the applicability of semiconductor as plasmonic materials is discussed. Huge advantage of semiconductors is the tunability their plasmonic properties. Three methods of controlling the plasmonic behavior of semiconductors were analyzed: Shifting of plasma frequency to higher frequencies by increasing of n-type doping concentration. Modification of the material permittivity (conductivity) tensor spectra by the external magnetic field. Shifting of plasmonic resonance by generation of nanogratings in the material, either by carrier concentration modulation by interference light illumination (sinusoidal grating) or by lithography (lamellar grating). The effective medium approximation of nanogratings was verified using Rigorous Coupled Wave Analysis.

An experimental application of widely tunable THz surface plasmon resonance sensor on semiconductors is presented. Generation of surface plasmon polariton at the interface between undoped InSb(InAs) and dielectric is experimentally demonstrated. This sensor has the added functionality of strong magnetic tuning. The applicability of this sensor is discussed, along with analysis of different sensor architecture.

Abstrakt

Tato práce zavádí matematický, fyzikální a experimentální rámec pro popis, charakterizaci a aplikaci plasmonických vlastností polovodičů. Plasmonické jevy v polovodičích jsou přítomny v terahertzové a daleké infračervené oblasti, kde mohou posloužit k vývoji nových zařízení nebo zlepšení stávajích senzorů.

Vzorky III-V polovodičů (GaAs, InP, InSb a InAs) s různým stupněm dopování byly analyzovány spektroskopicky v široké spektrální oblasti. Infračervné spektroskopie s Fourierovou transformací a terahertzová spektroskopie v časové doméně byly použity pro charakterizaci optických vlastností volných nosičů náboje (plasmonické vlastnosti) a optických vlastností vibrací atomové mřížky (fononické vlastnosti). K popsání těchto vlastností byl použit Drude-Lorentzův model, i s přidanou teorií pro popis magneto-optických jevů. Polovodiče s vysokou mobilitou nosičů náboje (InAs, InSb) vykazují obrovské magneto-optické jevy pro malé externí magnetické pole. Tyto optická měření byla porovnána s elektrickým měřením Hallova jevu pomocí Van der Pauwovy metody.

Z výsledků spektroskopických a magneto-optických měření vzorků je diskutována použitelnost polovodičů jako plasmonických materiálů. Výhodou polovodičů možnosti ladění jejich plasmonických vlastností. Tři metody ladění byly analyzovány: Zvyšování plasmonické frekvence pomocí n-dopování příměsemi. Změna materiálové permitivity a vodivosti pomocí magnetického pole. Změna plasmonické rezonance pomocí nanomřížek (efektivního prostředí), ať už vyrobenými pomocí změny dopování vzniklé interferenčním osvitem (sinusové mřížky) nebo litografickými metodami (lamelární mřížky). Aproximace efektivním prostředím nanomřížek byla ověřena pomocí rigorózní teorie vázaných vln.

Je prezentováno experimentální ověření široce laditelného terahertzového senzoru založeného na bázi rezonance povrchového plasmonu. Tento senzor má možné ladění díky externímu magnetickému poli. Použitelnost tohoto senzoru a analýza odlišné architektury senzoru jsou diskutovány.

List of Abbreviations and Symbols Used

E	Energy
N	Number of carriers
Q	Voigt parameter
R_H	Hall coefficient
S	Surface
Δ	Ellipsometric phase
$\Im$	Imaginary part
Λ	Period of grating
Ψ	Ellipsometric angle
$\Re$	Real part
χ	Susceptibility
ϵ	Ellipticity
γ	Damping constant
$\hat{\varepsilon}$	Permittivity tensor
$\hat{\varepsilon}^{eff}$	Effective permittivity tensor
λ	Wavelength
$\langle . \rangle$	Toeplitz matrix
$\lceil . \rceil$	Amplitudes of Fourier series expansion
$\mathbf{A}$	Vector of amplitudes
$\mathbf{B}$	Magnetic flux density
$\mathbf{D}$	Electric displacement
$\mathbf{E}$	Electric intensity
$\mathbf{E}'$	Normalized electric intensity
$\mathbf{F}$	Vector of tangential components
$\mathbf{H}$	Magnetic intensity
$\mathbf{H}'$	Normalized magnetic intensity
$\mathbf{I}$	Identity matrix
$\mathbf{J}$	Jones matrix

$\mathbf{M}$	Magnetization volume density
$\mathbf{M}$	Mueller matrix
$\mathbf{P}$	Polarization volume density
$\mathbf{P}$	Propagation matrix
$\mathbf{R}$	Reflectivity
$\mathbf{R}$	Rotation matrix
$\mathbf{T}$	Matrix of eigenvectors
$\mathbf{T}$	Transmittance
$\mathbf{V}$	Matrix of eigenvalues
$\mathbf{e}$	Electric polarization state vector
$\mathbf{f}$	Vector of tangential field components
$\mathbf{g}$	Vector of amplitudes
$\mathbf{h}$	Magnetic polarization state vector
$\mathbf{j}$	Current density
$\mathbf{k}$	Wave vector
$\mathbf{p},\ \mathbf{q}$	Matrices of tangential components
$\mathbf{r}$	Position vector
i	Imaginary unit
μ	Permeability
$\nabla\cdot$	Divergence operator
$\nabla\times$	Curl operator
ν	Normalized wave vector component
ω	Angular frequency
ω_0	Natural resonant frequency
ω_L	Lorentz term frequency
ω_c	Cyclotron frequency
ω_p	Plasma frequency
ϕ	Phase
ρ	Volume density of free charges
θ	Kerr rotation

ε	Permittivity
ε_0	Permittivity of vacuum
φ	Azimuth
c	Speed of light
e'	Normalized electric polarization state vector component
f	Frequency
h'	Normalized magnetic polarization state vector component
k_0	Wave vector magnitude
m^*	Effective mass
r	Reflection coefficient
t	Transmission coefficient
t	time
w	Width of lamells
$x,\ y,\ z$	Cartesian coordinates

EMA	Effective Medium Anisotropy

FDTD	Finite Difference Time Domain
FMM	Fourier Modal Method
FTIR	Fourier Transform Infrared Spectroscopy

IR	Infrared

MO	Magneto-optical

RCWA	Rigorous Coupled Wave Analysis

SE	Spectroscopic Ellipsometry
SP	Surface plasmon

SPP Surface plasmon polariton

SPR Surface plasmon resonance

TDS Time-domain spectroscopy

TE Transversal electric

THz Terahertz

TM Transversal magnetic

UV Ultraviolet

vis Visible

Acknowledgements

This thesis has been elaborated during a combined study at Technical University of Ostrava, Czech Republic and Dalhousie University in Halifax, Canada. I would like to express my deepest appreciation for the people who have guided me through the doctoral study, foremost Dr. Kamil Postava, Dr. Michael Čada and prof. Jaromír Pištora. Without them I wouldn't have had the excellent opportunity for this Czech-Canadian cooperation. I would also like to thank my Dalhousie committee, Dr. Yuan Ma and Dr. Alan Fine, for their help and guidance. My colleagues from Dr. Čada's group and Dr. Postava's group have my gratitude for their support, help and shared laughs. Thank you all for letting me stand on your shoulders.

My thanks also go to my wife, parents, grandparents and friends for their unconditional support and inexhaustible patience.

Chapter 1

Introduction

1.1 State of the art

Plasmonics [4–7] has been in research focus for last decades. Its promise, sub-wavelength confinement of electromagnetic waves below their diffraction limit at the boundary of negative (conductive) and positive (dielectric) permittivity material drove a search for applications that would utilize this behavior. Novel sensors [8], waveguides [9], transducers [10], couplers [11], lenses [12], nonlinear [13] and quantum phenomena [14], and improvements to scientific techniques [15] have all been based on plasmonics.

Utilizing the terahertz range for better and faster communications [2, 3, 16], sensing [17], medicine [18] and security [19] has created a need for devices, capable of operating in the desired frequency range of 0.1-30 THz. This range is home to many interesting phenomena. Organic molecules, aqueous solutions and many other compounds have a distinguishable spectra in the THz range, which together with non-ionizing properties of the terahertz radiation permits its broad use in biomedicine [20]. Absorbtion spectra from rotational transitions of gaseous analytes can be detected and analyzed through THz spectroscopy [21]. Moreover, THz spectroscopy has become indispensable in basic science and materials research, from dielectrics to superconductors [22]. The use of plasmonics has the potential to improve all of these areas. Traditional plasmonic materials usable in visible/near infrared range, noble metals, are unsuitable for uses in the THz regime due to low confinement to the metal; the wave is weakly bound to the interface, a phenomenon sometimes called the Zenneck plasmon [23]. Semiconductors with their carrier levels have their metallic properties shifted to lower frequencies - microwave, terahertz and far infrared. They are therefore suitable as building blocks for THz devices. Furthermore, they allow for much needed control of their electromagnetic properties. In the manufacturing the carrier levels can be adjusted by doping and after the manufacturing the properties

can be controlled by light [24], temperature [25], electric gating [26] and by external magnetic field [27].

The use of semiconductors in magneto-plasmonic devices for terahertz range has been suggested by Bolle et al. [28], while currently there are a number of studies, such as by Hu et al. [29], dealing with theoretical design of the devices. A correct implementation of the theoretical models is possible only when we know the exact properties of the materials used. Spectroscopic, non-destructive magneto-optical techniques give us the information we need.

The issue of semiconductor plasmonic properties in the far-infrared and terahertz range have been undertaken by several groups. The work of Palik and Furdyna [30] provides the necessary theory for optical and magneto-optical behavior of semiconductors. The experiments of Shubert et al. [31,32] and Hofmann [33] show the potential of spectroscopic techniques in investigating that behavior, while further works [34–40] demonstrate the power of terahertz time-domain spectroscopy in determining the conductive and optical functions of semiconductors.

The measurement of the free carrier magneto-optical effects in semiconductors has been called the "Optical Hall effect" by Kühne et al. [27] and Shubert et al. [31], who developed a far infrared and terahertz ellipsometric, full Mueller matrix method for semiconductor characterization. The potential of the terahertz time-domain spectroscopy (THz-TDS) in investigation of semiconductors had been recognized by Mittleman [34], (spatial inhomogeneities in GaAs), Jeon [37] (reflectivity of GaAs and Si), Grishowski [38] (properties Si, Ge, GaAs) and Ino [39] (MO effect on InAs).

InSb is a viable choice for Terahertz plasmonics, since its low effective mass, 0.015 m_0 at Γ point [41], means its electrical and optical properties can be modulated by a small magnetic fields. The area of spectroscopy of InSb in magnetic field has been pioneered by Lax et al. [42], while the subsequent theory had been summarized by Palik et al. [30], [43] and in references therein. The works of Spitzer et al. [44] combines reflectivity and electrical Hall effect characterization to derive effective mass/concentration data of n-doped InSb. The approach from microwave side of the spectrum has been established by Brodwin et al. [45] and subsequently by Singh et al. [46], to characterize polycrystalline and single crystals of InSb at 9GHz, with temperature and magnetic field dependence. The findings have also been reviewed by

Pidgeon [47] and Kushwaha [48]. Despite the wide range of semiconductors studied, the studies in the sixties and seventies were limited to the spectral range outside the terahertz gap (0.1-3 THz) due to a lack of available sources. Consequently, the authors had to use higher magnetic fields and low temperatures to observe interesting magneto-plasmonic effects in their spectral ranges, which is inconvenient for practical applications.

The surface plasmon resonance (SPR) [5] allows highly accurate sensing. This sensitivity of the properties and changes in the dielectric (analyte) has found its use primary in biomedical applications [49]. The natural high confinement of surface plasmons is valuable for investigation of samples with sub-wavelength sizes, when in THz range the wavelengths are on the order hundreds of micrometers. There is an ongoing research exploring other materials more applicable to lower frequencies SPR, with the potential candidates of conducting oxides [50], graphene [51,52], corrugated metal [53], and semiconductors [54], This ongoing research has so far remained theoretical.

The modulation of semiconductor plasmonic properties can also be utilized by spatially modulating, on subwavelength scale, the carrier concentration. Photoexcitation [55–59] of additional carries by light with energy below the band-gap of the semiconductor is a promising method. This way, arbitrary and temporary permittivity profiles can be created in the semiconductors using spatial light modulators or interference and holographic patterns. The easiest interference pattern would be the sinusoidal profile. What more, this profile arises in many other application, since represents a fundamental physical periodic modulation, which is produced phononic, magnonic [60], and thermal waves, or by diffusion processes. The sinusoidal gratings occur in volume holograms [61], liquid crystals, magneto-optic films with magnonic waves, photorefractive, and nonlinear optical media. Volume holograms in liquid-crystal polymers exhibit modulation of anisotropic optical properties described by the permittivity tensor [62]. Another example belongs to magneto-optically induced anisotropy by space modulation of magnetization, i.e. magnonic waves usualy studied by Brillouin light scattering and pump-probe time resolved magneto-optical experiments [63]. Similarly mechanic parameters of thin films are studied using generation of phononic waves [64]. Periodic modulations of mechanic properties opens new

horizons in the area of phononics [65, 66]. Despite the modelling of grating optical properties using numerical methods based on Fourier expansion – Rigorous Coupled Wave Algorithm (RCWA), Fourier Modal Method (FMM) [67], or Finite Difference Time Domain (FDTD) techniques [68] give precise results in a real computation time, it is often useful and needed to describe the system response using an approximate effective medium model. Such approximation can give (i) symbolic relations especially useful to describe and understand the complex response of anisotropic gratings and analytical dependence on a particular anisotropy parameter and (ii) for cases of subwavelength or quasistatic limit $\Lambda \ll \lambda$, where Λ and λ denote the grating period and light wavelength, the effective medium approximation (EMA) gives reasonable and precise results. The EMA is widely used to describe effective optical parameters from heterogeneous materials, nanostructures [69, 70], and also surface roughness [70]. The EMA is usually based on calculation of local field in spherical and ellipsoidal particles and it was generalized to special anisotropy [71, 72]. Effective parameters were also derived for lamellar isotropic gratings [73–75] and generalized to anisotropic media [76, 77]. On the other hand, EMA of sinusoidal grating from isotropic media was derived by Campbell and Kostuk [78], which has been applied to the holographic gratings [61].

1.2 Original contribution

The main contributions of this thesis to the field of plasmonics in semiconductors are:

1. **Spectroscopic characterization of III-V semiconductors.** Several samples of III-V semiconductors have been characterized in wide spectral range - from UV light to Terahertz range. The spectroscopic data have been modeled using Drude-Lorentz model and B-spline where appropriate. A metric has been devised to evaluate the plasmonic properties of semiconductors based on the level of doping. These findings have been published in Journal of European Optical Society - Rapid Publication [79] (First author).

2. **Magneto-optical free carrier effect in semiconductors.** A huge magneto-optical effect has been observed in the Terahertz range on InSb. The spectroscopic characterization of the samples under external magnetic field has been

compared to the model with good agreement. This effect has been verified by a electrical Hall effect measurement. The MO effect is discussed as a modulation of plasmonic properties of semiconductors. The experiment, data analysis and conclusions have been published in AIP Advances [80] (First author). The data on n-doped InSb have been used by our colleagues for the design on noreciprocal Mid-IR Isolator [81] (Third author - supplied material parameters).

3. **Experimental demonstration of surface magneto-plasmon on InSb and InAs in the terahertz range.** The magneto-plasmonic properties of semiconductors (InSb and InAs) have been utilized in construction of a plasmonic device - a surface plasmon resonance sensor. High refractive index prism is used to couple surface plasmon polariton on an interface between semiconductor and polymer film. A large tuning capability of the sensor has been demonstrated using external magnetic field. An expression of surface plasmon at anisotropic interface has also been derived. These results have been accepted to Scientific Reports [82] (First author).

4. **Application of effective medium approximation as a method for modulation plasmonic properties**. The effective medium theory is extended to subwavelength gratings with harmonic modulation of permittivity - a case which is attainable is semiconductors by spatially varying the doping levels or by illuminating the sample with interference pattern. Rigorous coupled wave analysis is used to confirm the validity of the derived formulas. An example where the subwavelength gratings are used for tuning of the surface plasmon resonance is presented [83] (Second author - RCWA calculation of harmonic gratings, validity calculation, application to semiconductors).

1.3 Thesis Organization

This thesis is divided in 3 main chapters, Introductory chapter and Conclusions and perspectives chapter. The three main chapters are:

Chapter 2 presents the necessary mathematical tools for describing spectroscopic data of multilayers and gratings. It starts with the review of electromagnetic waves

and polarized light. Then the chapter deals with finding eigenmodes in layered structure using a Berreman 4x4 matrix method and how to calculate experimental observables. This approach is extended into 1D periodic gratings, also with formulas for calculation of effective medium anisotropy from subwavelength gratings. This chapter is not necessary for understanding the key concepts and main results of the thesis.

Chapter 3 outlines the methods for spectroscopic characterization of semiconductors and presents the results of measurement of several samples of III-V semiconductors (InP-n, GaAs-n,p, InSb-n,p,undoped, InAs undoped). The methods are Ellipsometry, Fourier Transform Infrared Spectroscopy and Terahertz Time-Domain Spectroscopy. The description of optical properties of semiconductors is extended to the influence of external magnetic field. This effect has been measured and described in InSb with different levels of doping.

Chapter 4 deals with the application of semiconductors in plasmonics. The general framework for understanding surface plasmon polaritons is established both classically and with the matrix tools derived in Chapter 2. Appropriate figures of merit are estimated to establish suitable ranges for room temperature semiconductor plasmonics applications. A surface magneto-plasmon resonance sensor is experimentally demonstrated and analyzed, along with designs for different sensor architectures. The effective medium approximation is also applied for a design of SPR sensor covering broad range of usable frequencies.

Chapter 2

Polarized light in multilayers and gratings

2.1 Multilayers

2.1.1 Electromagnetic waves

There is no other way of explaining the electromagnetic nature of light than beginning with the four Maxwell's equations. First we define all the necessary symbols and operators: $\mathbf{r}$ is the position vector, t is the time, $\nabla\times$ denotes the curl operator, $\nabla\cdot$ is the divergence operator, $\mathbf{H}(\mathbf{r},t)$ is the vector of magnetic intensity and $\mathbf{E}(\mathbf{r},t)$ is the vector of electric intensity. $\mathbf{D}(\mathbf{r},t)$ is the vector of electric displacement and $\mathbf{B}(\mathbf{r},t)$ is the magnetic flux density. Vectors $\mathbf{P}(\mathbf{r},t)$ and $\mathbf{M}(\mathbf{r},t)$ denote the polarization and magnetization volume density, respectively. μ_0 and ε_0 are the permeability and the permittivity of vacuum. Finally, $\rho(\mathbf{r},t)$ is the volume density of free charges and $\mathbf{j}(\mathbf{r},t)$ is the current density. The four Maxwell's equations are

$$\nabla \times \mathbf{H}(\mathbf{r},t) = \mathbf{j}(\mathbf{r},t) + \frac{\partial \mathbf{D}(\mathbf{r},t)}{\partial t}, \tag{2.1a}$$

$$\nabla \times \mathbf{E}(\mathbf{r},t) = -\frac{\partial \mathbf{B}(\mathbf{r},t)}{\partial t}, \tag{2.1b}$$

$$\nabla \cdot \mathbf{D}(\mathbf{r},t) = \rho(\mathbf{r},t), \tag{2.1c}$$

$$\nabla \cdot \mathbf{B}(\mathbf{r},t) = 0. \tag{2.1d}$$

To these four equations we add the constitution relations for polarization and magnetization

$$\mathbf{D}(\mathbf{r},t) = \varepsilon_0 \mathbf{E}(\mathbf{r},t) + \mathbf{P}(\mathbf{r},t), \tag{2.2a}$$

$$\mathbf{B}(\mathbf{r},t) = \mu_0 \mathbf{H}(\mathbf{r},t) + \mu_0 \mathbf{M}(\mathbf{r},t). \tag{2.2b}$$

Since we will be using only optical frequencies, we can assume that $\mathbf{M}(\mathbf{r},t) = 0$. Also, we shall not deal with any free charges, therefore $\rho(\mathbf{r},t) = 0$. For a linear, homogeneous and non-dispersive medium we can define the polarization density vector

$\mathbf{P}$ using the relative electric susceptibility tensor $\hat{\chi}$

$$\mathbf{P}(\mathbf{r},t) = \varepsilon_0 \hat{\chi} \mathbf{E}(\mathbf{r},t). \tag{2.3}$$

The permittivity tensor for the medium can also be expressed using the susceptibility as

$$\hat{\varepsilon} = \varepsilon_0(\hat{\mathrm{I}} + \hat{\chi}) = \varepsilon_0 \hat{\varepsilon}_R, \tag{2.4}$$

where $\hat{\varepsilon}_R$ denotes the relative permittivity tensor. Now we can substitute relations (2.3) and (2.4) with the condition of $\mathbf{M}$=0 into (2.2a) and (2.2b), thus yielding

$$\mathbf{D}(\mathbf{r},t) = \hat{\varepsilon} \mathbf{E}(\mathbf{r},t), \tag{2.5a}$$

$$\mathbf{B}(\mathbf{r},t) = \mu_0 \mathbf{H}(\mathbf{r},t). \tag{2.5b}$$

Furthermore, we can express the current density vector $\mathbf{j}$ using the electric conductivity tensor $\hat{\sigma}$

$$\mathbf{j}(\mathbf{r},t) = \hat{\sigma} \mathbf{E}(\mathbf{r},t) \tag{2.6}$$

and the Maxwell's equations can be rewritten in this form:

$$\nabla \times \mathbf{H}(\mathbf{r},t) = \hat{\varepsilon} \frac{\mathrm{d}\mathbf{E}(\mathbf{r},t)}{\mathrm{d}t} + \hat{\sigma} \mathbf{E}(\mathbf{r},t), \tag{2.7a}$$

$$\nabla \times \mathbf{E}(\mathbf{r},t) = -\mu_0 \frac{\mathrm{d}\mathbf{H}(\mathbf{r},t)}{\mathrm{d}t}, \tag{2.7b}$$

$$\nabla \cdot [\hat{\varepsilon} \mathbf{E}(\mathbf{r},t)] = 0, \tag{2.7c}$$

$$\nabla \cdot \mathbf{H}(\mathbf{r},t) = 0. \tag{2.7d}$$

In the following theory and examples we shall deal only with monochromatic waves. All components of electric and magnetic field are harmonic functions of time with the same frequency f, or more conveniently with the same angular frequency $\omega = 2\pi f$. The electric and magnetic field then takes the form

$$\mathbf{E}(\mathbf{r},t) = \mathbf{E}(\mathbf{r}) \exp(-\mathrm{i}\omega t), \tag{2.8a}$$

$$\mathbf{H}(\mathbf{r},t) = \mathbf{H}(\mathbf{r}) \exp(-\mathrm{i}\omega t), \tag{2.8b}$$

where $\mathbf{E}(\mathbf{r})$ and $\mathbf{H}(\mathbf{r})$ are the complex amplitudes. Now, excluding the time dependence and substituting (2.8a) and (2.8b) into (2.7a) and (2.7b), we shall simplify

them into

$$\nabla \times \mathbf{H}(\mathbf{r}) = -\mathrm{i}\omega\hat{\varepsilon}\mathbf{E}(\mathbf{r}) + \hat{\sigma}\mathbf{E}(\mathbf{r}), \tag{2.9a}$$

$$\nabla \times \mathbf{E}(\mathbf{r}) = \mathrm{i}\omega\mu_0\mathbf{H}(\mathbf{r}). \tag{2.9b}$$

As we can from (2.9a), there is linear dependency of the curl of the magnetic field on the electric field. Such dependency implies the existence of the *complex permittivity tensor*, a material function describing its interaction with electromagnetic field $\hat{\varepsilon}'$

$$\hat{\varepsilon}' = \hat{\varepsilon} + \frac{i}{\omega}\hat{\sigma}. \tag{2.10}$$

The first two Maxwell's equations become

$$\nabla \times \mathbf{H}(\mathbf{r}) = -\mathrm{i}\omega\hat{\varepsilon}'\mathbf{E}(\mathbf{r}) \tag{2.11a}$$

$$\nabla \times \mathbf{E}(\mathbf{r}) = \mathrm{i}\omega\mu_0\mathbf{H}(\mathbf{r}) \tag{2.11b}$$

and with the other equations (2.7c) and (2.7d) can be used in any homogeneous material. For simplicity, we won't distinguish between complex and only real permittivity and all permittivity tensors will be denoted $\hat{\varepsilon}$. When it is necessary to talk about real or imaginary part of permittivity, it is so stated in text.

2.1.2 Polarization of light

The spatial orientation of the electric vector of the electromagnetic wave is called its polarization. The polarization of light is used in large number of physical applications, such as computer imaging, lasers, photography, and many others. We shall deal with monochromatic plane wave, which can be described using complex representation of the field vectors

$$\mathbf{E}(\mathbf{r}, t) = E_0\mathbf{e}\exp[\mathrm{i}(\mathbf{kr} - \omega t)], \tag{2.12a}$$

$$\mathbf{H}(\mathbf{r}, t) = H_0\mathbf{h}\exp[\mathrm{i}(\mathbf{kr} - \omega t)], \tag{2.12b}$$

where $\mathbf{k}$ is the wave vector with magnitude $k_0 = \omega/c$, c being the speed of light and $\mathbf{e}$ and $\mathbf{h}$ are the corresponding polarization state vectors. As we follow these vectors in plane perpendicular to the propagation direction, we discover their endpoints trace an ellipse. Such ellipse is defined by two parameters, φ and ϵ, the azimuth and the

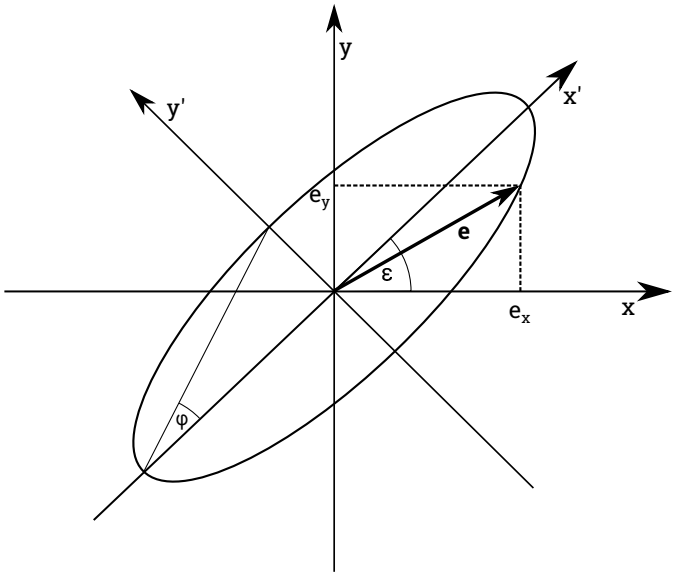

Figure 2.1: Schematic of the elliptical path of the real part of the electric polarization vector

ellipticity, respectively, shown in Figure 2.1. We can define several significant cases of light polarization. First one being the most general, the elliptical. Then we have two sets of polarizations: circular (right and left) and linear (s and p). The electric field component of s-polarized wave (*senkrecht* from German), or transversal electric (TE) wave oscillates in the direction perpendicular to the plane of incidence. The electric field component p-polarized wave (parallel), or transversal magnetic (TM) wave oscillates parallel to the plane of incidence. Both waves are mutually orthogonal and so we can derive any linear polarization as a combination of these two.

2.1.3 Permittivity tensor

As mentioned in Section 2.1.1, the permittivity tensor is a material function which describes how the given material alters reflected, transmitted and propagating light. It is a tensor with elements, labeled in this way (aka the general permittivity tensor):

$$\hat{\varepsilon} = \begin{bmatrix} \varepsilon_{xx} & \varepsilon_{xy} & \varepsilon_{xz} \\ \varepsilon_{yx} & \varepsilon_{yy} & \varepsilon_{yz} \\ \varepsilon_{zx} & \varepsilon_{zy} & \varepsilon_{zz} \end{bmatrix}. \tag{2.13}$$

There are several special cases of the permittivity tensor

- **isotropic medium**

  Isotropic medium is such a medium, which changes the flow of light irregardless of the incoming/propagating direction. Mathematically speaking, the tensor is only diagonal with all elements the same. The refractive index of isotropic material is defined as $n = \sqrt{\varepsilon_{xx}}$

$$\hat{\varepsilon} = \begin{bmatrix} \varepsilon_{xx} & 0 & 0 \\ 0 & \varepsilon_{xx} & 0 \\ 0 & 0 & \varepsilon_{xx} \end{bmatrix}. \tag{2.14}$$

- **uniaxial anisotropic medium**

  Medium with such anisotropy exhibits different behavior along one axis. In this case, y-axis. Such anisotropy induces the birefringence effect known from e.g calcite.

$$\hat{\varepsilon} = \begin{bmatrix} \varepsilon_{xx} & 0 & 0 \\ 0 & \varepsilon_{yy} & 0 \\ 0 & 0 & \varepsilon_{xx} \end{bmatrix}. \tag{2.15}$$

- **biaxial anisotropic medium**

  Material with biaxial anisotropy has all diagonal elements different.

$$\hat{\varepsilon} = \begin{bmatrix} \varepsilon_{xx} & 0 & 0 \\ 0 & \varepsilon_{yy} & 0 \\ 0 & 0 & \varepsilon_{zz} \end{bmatrix}. \tag{2.16}$$

- **rotation** The latter two previous tensors are valid only if the axes correspond with given coordinate system. In case they do not, we must use the rotation matrix $\mathbf{R}$,

$$\mathbf{R}_x = \begin{bmatrix} 1 & 0 & 0 \\ 0 & \cos\rho & -\sin\rho \\ 0 & \sin\rho & \cos\rho \end{bmatrix} \mathbf{R}_y = \begin{bmatrix} \cos\rho & 0 & -\sin\rho \\ 0 & 1 & 0 \\ \sin\rho & 0 & \cos\rho \end{bmatrix} \mathbf{R}_z = \begin{bmatrix} \cos\rho & -\sin\rho & 0 \\ \sin\rho & \cos\rho & 0 \\ 0 & 0 & 1 \end{bmatrix}, \tag{2.17}$$

  where the subscript denotes the axis around which the system is rotated and ρ is the angle of such rotation. The permittivity tensor is then altered in this fashion:

$$\hat{\varepsilon}_{rotated} = \mathbf{R}^{-1}\hat{\varepsilon}\mathbf{R} \tag{2.18}$$

- **magneto-optical anisotropy**

  Another case of permittivity tensor is the magneto-optical anisotropy, where a permittivity change is induced by the magnetization of the sample. Here comes in question the orientation of the magnetization in respect to plane of incidence. There are three cases of magneto-optical anisotropy configurations, polar, longitudinal and transversal, as depicted in Figure 2.2. The magneto-optical effect is usually defined through the Voigt parameter Q. Depending on the configuration, it affects different off-diagonal elements of the permittivity tensor, always in the $\pm$ symmetry.

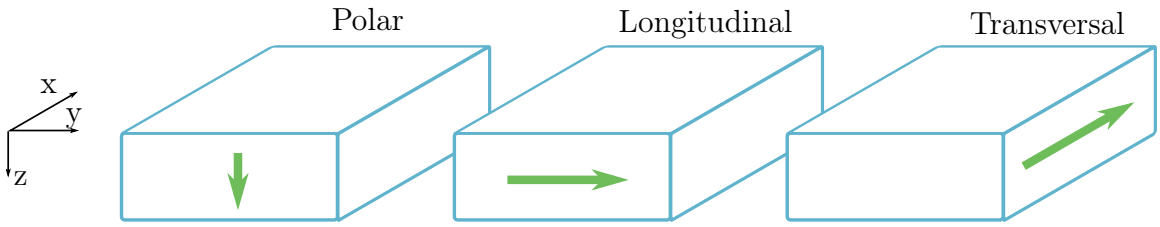

Figure 2.2: Different orientations of the magnetic field. The plane of incidence is in the $y-z$ plane.

- polar

$$\hat{\varepsilon} = \begin{bmatrix} \varepsilon_{xx} & iQ & 0 \\ -iQ & \varepsilon_{yy} & 0 \\ 0 & 0 & \varepsilon_{zz} \end{bmatrix} \tag{2.19}$$

- longitudinal

$$\hat{\varepsilon} = \begin{bmatrix} \varepsilon_{xx} & 0 & -iQ \\ 0 & \varepsilon_{yy} & 0 \\ iQ & 0 & \varepsilon_{zz} \end{bmatrix} \tag{2.20}$$

- transversal

$$\hat{\varepsilon} = \begin{bmatrix} \varepsilon_{xx} & 0 & 0 \\ 0 & \varepsilon_{yy} & iQ \\ 0 & -iQ & \varepsilon_{zz} \end{bmatrix} \tag{2.21}$$

2.1.4 Berreman approach

We now have from the previous sections the description of polarized light, and the description of material parameters through permittivity. In this section we will join them together to analyze optical response of multilayer structures. We will be using the Berreman 4×4 matrix approach [84]. In the following theory and examples we shall deal only with monochromatic waves [85]. All components of electric and magnetic field are harmonic functions of time with the same angular frequency ω, as shown in (2.8a) and (2.8b). We assume that light is incident on the upper layer in the form of a plane wave. Numbering of following layers is shown in Figure 2.3, along with system coordinates.

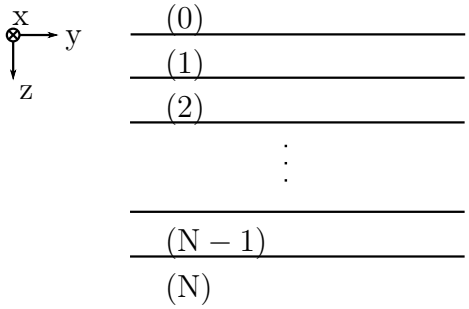

Figure 2.3: Numbering of layers

We start off with normalization of (2.11a) and (2.11b) as derived by Berreman [84].

$$\mathbf{E}'(\mathbf{r}) = \sqrt[4]{\mu_0^{-1}\varepsilon_0}\mathbf{E}(\mathbf{r}), \tag{2.22a}$$

$$\mathbf{H}'(\mathbf{r}) = \sqrt[4]{\mu_0^{-1}\varepsilon_0}\mathbf{H}(\mathbf{r}). \tag{2.22b}$$

Such notion lead to equations in the form of

$$\nabla \times \mathbf{H}'(\mathbf{r}) = -\mathrm{i}k_0\hat{\varepsilon}_R\mathbf{E}'(\mathbf{r}), \tag{2.23a}$$

$$\nabla \times \mathbf{E}'(\mathbf{r}) = \mathrm{i}k_0\mathbf{H}'(\mathbf{r}), \tag{2.23b}$$

where $k_0 = \frac{\omega}{c}$ denotes the wave vector in free space. The next step is rewriting these equations in the compact matrix form. From the tensor theory, we can easily deduce that the curl operator has this matrix form

$$\nabla \times \begin{bmatrix} \mathbf{H}'_{\mathbf{x}}(\mathbf{r}) \\ \mathbf{H}'_{\mathbf{y}}(\mathbf{r}) \\ \mathbf{H}'_{\mathbf{z}}(\mathbf{r}) \end{bmatrix} = \begin{bmatrix} 0 & -\frac{\partial}{\partial z} & \frac{\partial}{\partial y} \\ \frac{\partial}{\partial z} & 0 & -\frac{\partial}{\partial x} \\ -\frac{\partial}{\partial y} & \frac{\partial}{\partial x} & 0 \end{bmatrix} \begin{bmatrix} \mathbf{H}'_{\mathbf{x}}(\mathbf{r}) \\ \mathbf{H}'_{\mathbf{y}}(\mathbf{r}) \\ \mathbf{H}'_{\mathbf{z}}(\mathbf{r}) \end{bmatrix}. \tag{2.24}$$

That allows us to rewrite (2.23a) and (2.23b) with general permittivity tensor, with all 9 elements, in the form

$$\begin{bmatrix} 0 & -\frac{\partial}{\partial z} & \frac{\partial}{\partial y} \\ \frac{\partial}{\partial z} & 0 & -\frac{\partial}{\partial x} \\ -\frac{\partial}{\partial y} & \frac{\partial}{\partial x} & 0 \end{bmatrix} \begin{bmatrix} \mathbf{H'_x}(\mathbf{r}) \\ \mathbf{H'_y}(\mathbf{r}) \\ \mathbf{H'_z}(\mathbf{r}) \end{bmatrix} = -\mathrm{i}k_0 \begin{bmatrix} \varepsilon_{xx} & \varepsilon_{xy} & \varepsilon_{xz} \\ \varepsilon_{yx} & \varepsilon_{yy} & \varepsilon_{yz} \\ \varepsilon_{zx} & \varepsilon_{zy} & \varepsilon_{zz} \end{bmatrix} \begin{bmatrix} \mathbf{E'_x}(\mathbf{r}) \\ \mathbf{E'_y}(\mathbf{r}) \\ \mathbf{E'_z}(\mathbf{r}) \end{bmatrix} \tag{2.25a}$$

$$\begin{bmatrix} 0 & -\frac{\partial}{\partial z} & \frac{\partial}{\partial y} \\ \frac{\partial}{\partial z} & 0 & -\frac{\partial}{\partial x} \\ -\frac{\partial}{\partial y} & \frac{\partial}{\partial x} & 0 \end{bmatrix} \begin{bmatrix} \mathbf{E'_x}(\mathbf{r}) \\ \mathbf{E'_y}(\mathbf{r}) \\ \mathbf{E'_z}(\mathbf{r}) \end{bmatrix} = \mathrm{i}k_0 \begin{bmatrix} \mathbf{H'_x}(\mathbf{r}) \\ \mathbf{H'_y}(\mathbf{r}) \\ \mathbf{H'_z}(\mathbf{r}) \end{bmatrix}. \tag{2.25b}$$

Plane wave solution without time dependence can be reduced to in-plane (x- and y-) direction as

$$\mathbf{E}'(\mathbf{r}) = E'_0 \mathbf{e}' \exp[\mathrm{i}k_0(\nu_x x + \nu_y y)], \tag{2.26a}$$

$$\mathbf{H}'(\mathbf{r}) = H'_0 \mathbf{h}' \exp[\mathrm{i}k_0(\nu_x x + \nu_y y)], \tag{2.26b}$$

ν_x and ν_y being components of normalized wave vector $\mathbf{k} = k_0(\nu_x + \nu_y + \nu_z)$ and $\mathbf{e}'$ and $\mathbf{h}'$ are the polarization state unit vectors. This leads to reduced matrix equations, where E'_0 and H'_0 are equal due to normalization conditions and are factored out

$$\begin{bmatrix} 0 & -\frac{\partial}{\partial z} & \mathrm{i}k_0\nu_y \\ \frac{\partial}{\partial z} & 0 & -\mathrm{i}k_0\nu_x \\ -\mathrm{i}k_0\nu_y & \mathrm{i}k_0\nu_x & 0 \end{bmatrix} \begin{bmatrix} h'_x(z) \\ h'_y(z) \\ h'_z(z) \end{bmatrix} = -ik_0 \begin{bmatrix} \varepsilon_{xx} & \varepsilon_{xy} & \varepsilon_{xz} \\ \varepsilon_{yx} & \varepsilon_{yy} & \varepsilon_{yz} \\ \varepsilon_{zx} & \varepsilon_{zy} & \varepsilon_{zz} \end{bmatrix} \begin{bmatrix} e'_x(z) \\ e'_y(z) \\ e'_z(z) \end{bmatrix} \tag{2.27a}$$

$$\begin{bmatrix} 0 & -\frac{\partial}{\partial z} & \mathrm{i}k_0\nu_y \\ \frac{\partial}{\partial z} & 0 & -\mathrm{i}k_0\nu_x \\ -\mathrm{i}k_0\nu_y & \mathrm{i}k_0\nu_x & 0 \end{bmatrix} \begin{bmatrix} e'_x(z) \\ e'_y(z) \\ e'_z(z) \end{bmatrix} = \mathrm{i}k_0 \begin{bmatrix} h'_x(z) \\ h'_y(z) \\ h'_z(z) \end{bmatrix}. \tag{2.27b}$$

We know that tangential components of electric and magnetic field are continuous at boundaries, so we need to derive them from the reduced equations

$$\begin{bmatrix} 0 & -\frac{\partial}{\partial z} \\ \frac{\partial}{\partial z} & 0 \end{bmatrix} \begin{bmatrix} h'_x(z) \\ h'_y(z) \end{bmatrix} + ik_0 \begin{bmatrix} \nu_y h'_z(z) \\ -\nu_x h'_z(z) \end{bmatrix} = -\mathrm{i}k_0 \begin{bmatrix} \varepsilon_{xx} & \varepsilon_{xy} \\ \varepsilon_{yx} & \varepsilon_{yy} \end{bmatrix} \begin{bmatrix} e'_x(z) \\ e'_y(z) \end{bmatrix} - ik_0 \begin{bmatrix} \varepsilon_{xz} e'_z(z) \\ \varepsilon_{yz} e'_z(z) \end{bmatrix}, \tag{2.28a}$$

$$\begin{bmatrix} 0 & -\frac{\partial}{\partial z} \\ \frac{\partial}{\partial z} & 0 \end{bmatrix} \begin{bmatrix} e'_x(z) \\ e'_y(z) \end{bmatrix} + \mathrm{i}k_0 \begin{bmatrix} \nu_y e'_z(z) \\ -\nu_x e'_z(z) \end{bmatrix} = ik_0 \begin{bmatrix} h'_x(z) \\ h'_y(z) \end{bmatrix}. \tag{2.28b}$$

Furthermore, from the reduced equation we shall extract the normal field components (z-direction)

$$e'_z(z) = \varepsilon_{zz}^{-1}[\nu_y h'_x(z) - \nu_x h'_y(z) - \varepsilon_{zx} e'_x(z) - \varepsilon_{zy} e'_z(z)], \tag{2.29a}$$

$$h'_z(z) = -\nu_y e'_x(z) + \nu_x e'_y(z) \tag{2.29b}$$

and the define the vector of tangential field components

$$\mathbf{f}(z) = [e'_x(z), h'_y(z), e'_y(z), h'_x(z)]^T. \tag{2.30}$$

Now we can implement (2.29a)-(2.29b) and vector $\mathbf{f}(z)$ into (2.28a) and (2.28b), giving us series of differential equations, written in matrix form

$$\left\{ \begin{bmatrix} 0 & -\frac{\partial}{\partial z} & 0 & 0 \\ 0 & 0 & 0 & \frac{\partial}{\partial z} \\ 0 & 0 & -\frac{\partial}{\partial z} & 0 \\ \frac{\partial}{\partial z} & 0 & 0 & 0 \end{bmatrix} + ik_0 \begin{bmatrix} -\nu_y^2 & 0 & \nu_y\nu_x & 0 \\ \nu_x\nu_y & 0 & -\nu_x^2 & 0 \\ -\nu_y\varepsilon_{zz}^{-1}\varepsilon_{zx} & -\nu_y\varepsilon_{zz}^{-1}\nu_x & -\nu_y\varepsilon_{zz}^{-1}\varepsilon_{zy} & \nu_y\varepsilon_{zz}^{-1}\nu_y \\ \nu_x\varepsilon_{zz}^{-1}\varepsilon_{zx} & \nu_x\varepsilon_{zz}^{-1}\nu_x & \nu_x\varepsilon_{zz}^{-1}\varepsilon_{zy} & -\nu_x\varepsilon_{zz}^{-1}\nu_y \end{bmatrix} \right\} \mathbf{f}(z) =$$

$$\mathrm{i}k_0 \left\{ \begin{bmatrix} -\varepsilon_{xx} & 0 & -\varepsilon_{xy} & 0 \\ -\varepsilon_{yx} & 0 & -\varepsilon_{yy} & 0 \\ 0 & 0 & 0 & 1 \\ 0 & 1 & 0 & 0 \end{bmatrix} + \begin{bmatrix} \varepsilon_{xz}\varepsilon_{zz}^{-1}\varepsilon_{zx} & \varepsilon_{xz}\varepsilon_{zz}^{-1}\nu_x & \varepsilon_{xz}\varepsilon_{zz}^{-1}\varepsilon_{zy} & -\varepsilon_{xz}\varepsilon_{zz}^{-1}\nu_y \\ \varepsilon_{yz}\varepsilon_{zz}^{-1}\varepsilon_{zx} & \varepsilon_{yz}\varepsilon_{zz}^{-1}\nu_x & \varepsilon_{yz}\varepsilon_{zz}^{-1}\varepsilon_{zy} & -\varepsilon_{yz}\varepsilon_{zz}^{-1}\nu_y \\ 0 & 0 & 0 & 0 \\ 0 & 0 & 0 & 0 \end{bmatrix} \right\} \mathbf{f}(z), \tag{2.31}$$

which can be rewritten, with some rearrangements in the simple form

$$\frac{\partial}{\partial z}\mathbf{f}(z) = \mathrm{i}k_0\mathbf{C}\mathbf{f}(z). \tag{2.32}$$

The matrix $\mathbf{C}$ includes material tensor and components of the wave vector in the form

$$\mathbf{C} = \begin{bmatrix} -\nu_x\varepsilon_{zz}^{-1}\varepsilon_{zx} & 1-\nu_x\varepsilon_{zz}^{-1}\nu_x & -\nu_x\varepsilon_{zz}^{-1}\varepsilon_{zy} & \nu_x\varepsilon_{zz}^{-1}\nu_y \\ -\nu_y^2+\varepsilon_{xx}-\varepsilon_{xz}\varepsilon_{zz}^{-1}\varepsilon_{zx} & -\varepsilon_{xz}\varepsilon_{zz}^{-1}\nu_x & \nu_y\nu_x+\varepsilon_{xy}-\varepsilon_{xz}\varepsilon_{zz}^{-1}\varepsilon_{zy} & \varepsilon_{xz}\varepsilon_{zz}^{-1}\nu_y \\ -\nu_y\varepsilon_{zz}^{-1}\varepsilon_{zx} & -\nu_y\varepsilon_{zz}^{-1}\nu_x & -\nu_y\varepsilon_{zz}^{-1}\varepsilon_{zy} & -\nu_y\varepsilon_{zz}^{-1}\nu_y-1 \\ -\nu_x\nu_y-\varepsilon_{yx}+\varepsilon_{yz}\varepsilon_{zz}^{-1}\varepsilon_{zx} & \varepsilon_{yz}\varepsilon_{zz}^{-1}\nu_x & \nu_x^2-\varepsilon_{yy}+\varepsilon_{yz}\varepsilon_{zz}^{-1}\varepsilon_{zy} & -\varepsilon_{yz}\varepsilon_{zz}^{-1}\nu_y \end{bmatrix} \tag{2.33}$$

Equation (2.32) can be solved in number of ways, we use eigenvectors and eigenvalues solution. We introduce the matrix $\mathbf{T}$, with eigenvectors of the matrix $\mathbf{C}$ on its columns and matrix $\mathbf{V}$ with eigenvalues of $\mathbf{C}$ on its diagonal. The relation between $\mathbf{C}$, $\mathbf{T}$ and $\mathbf{V}$ can be summarized as

$$(\mathbf{C}-\mathbf{V})\mathbf{T} = \mathbf{0}. \tag{2.34}$$

Now we will introduce the vector of amplitudes $\mathbf{g}(z)$ related to the eigenmodes satisfying

$$\mathbf{f}(z) = \mathbf{T}\mathbf{g}(z). \tag{2.35}$$

Then (2.32) becomes

$$\frac{\partial}{\partial z}\mathbf{g}(z) = \mathrm{i}k_0\mathbf{T}^{-1}\mathbf{C}\mathbf{T}\mathbf{g}(z) = \mathrm{i}k_0\mathbf{V}\mathbf{g}(z), \tag{2.36}$$

with the expansion using vector $\mathbf{A}$ of amplitudes for $z = 0$

$$\mathbf{g}(z) = \exp(ik_0z\mathbf{V})\mathbf{A}. \tag{2.37}$$

The eigenvectors in matrix $\mathbf{T}$ correspond to the modes propagating through the medium without the change of polarization. For layered structure, there are 4 of them, two propagating up and two propagating down, with generally elliptic polarization. To determine optical properties of our system, we need to put up the matrix $\mathbf{C}$ for every layer, including superstrate and substrate, and find its corresponding matrices $\mathbf{V}$ and $\mathbf{T}$.

Numerical calculation of eigenmodes and eigenvectors returns unordered values. To find measurable quantities, we need to specifically define elements of $\mathbf{T}$ and $\mathbf{V}$ in

the top and bottom media - which column corresponds to which mode. We do this by doing an analytical calculation for isotropic material and choosing the propagating waves in the top and bottom media as linearly polarized. For calculation of reflectivity, only the top layer needs to have known order of modes. Modes inside the structure need to be organized only based in up-down fashion. This calculation is also extended to biaxial anisotropic material.

Isotropic case

For the simplified calculation of $\mathbf{T}$ and $\mathbf{V}$ matrices, we shall use the isotropic permittivity tensor (diagonal). We are also assuming no azimuthal angle, so that $\nu_x = 0$ and in our configuration, the component ν_y is defined as $\nu_y = \sqrt{\varepsilon_0}\sin\theta$, where ε_0 is the permittivity of the isotropic superstrate and θ is the angle of incidence. The matrix C will take form

$$\mathbf{C} = \begin{bmatrix} 0 & 1 & 0 & 0 \\ \varepsilon_{xx} - \nu_y^2 & 0 & 0 & 0 \\ 0 & 0 & 0 & \nu_y \varepsilon_{xx}^{-1} \nu_y - 1 \\ 0 & 0 & \varepsilon_{xx}^{-1} & 0 \end{bmatrix}. \tag{2.38}$$

The eigenvalue problem is now considerably simpler, we have the eq.

$$(\mathbf{C} - \nu_z \mathbf{I})\mathbf{f} = \mathbf{0}, \tag{2.39}$$

where $\mathbf{I}$ is 4×4 identity matrix. Determinant of the bracketed expression must be zero and therefore we arrive at formula

$$(\nu_z^2 + \nu_y^2 - \varepsilon_{xx})^2 = 0, \tag{2.40}$$

with couple of two identical solutions:

$$\begin{aligned} \nu_{z,1} = \nu_{z,3} &= \sqrt{\varepsilon_{xx} - \nu_y^2}, \\ \nu_{z,2} = \nu_{z,4} &= -\sqrt{\varepsilon_{xx} - \nu_y^2}. \end{aligned} \tag{2.41}$$

Eigenvectors are derived from (2.39) and for the magnetic components we have the relations

$$h'_x = -\frac{\varepsilon_{xx}}{\nu_z} e'_y, \qquad h'_y = \nu_z e'_x. \tag{2.42}$$

Normalized polarization vector has the property

$$\|\mathbf{e}'\| = e_x'^2 + e_y'^2 + e_z'^2 = 1 \tag{2.43}$$

and first we take $e_x' = 1$ and second $e_x' = 0$ to express the eigenvectors of TE and TM polarized wave. We arrange them in the matrix $\mathbf{T}$,

$$\mathbf{T}_{isotropic} = \begin{bmatrix} 1 & 1 & 0 & 0 \\ \sqrt{\varepsilon_{xx} - \nu_y^2} & -\sqrt{\varepsilon_{xx} - \nu_y^2} & 0 & 0 \\ 0 & 0 & (\sqrt{\varepsilon_{xx}})^{-1}\sqrt{\varepsilon_{xx} - \nu_y^2} & (\sqrt{\varepsilon_{xx}})^{-1}\sqrt{\varepsilon_{xx} - \nu_y^2} \\ 0 & 0 & -\sqrt{\varepsilon_{xx}} & \sqrt{\varepsilon_{xx}} \end{bmatrix} \tag{2.44}$$

with ordering TE-down, TE-up, TM-down and TM-up on its columns.

Biaxial case with symmetry axis aligned with coordinate system

Most anisotropic problems are better solved numerically. Analytical solution can however provide understanding of the problem at hand. Such case might be with anisotropic biaxial layer, where all diagonal components of the permittivity tensor are different, as shown in (2.16). In this case, the determinant of the expression $\mathbf{C} - \nu_z\mathbf{I}$ is not straightforward. Here we adopt a method from another formalism, Yeh's [86], which leads to the same results as the Berreman formalism. Lets start with the wave equation of an electromagnetic wave

$$k_0^2\hat{\varepsilon}\mathbf{E} - \mathbf{k}^2\mathbf{E} + \mathbf{k}[\mathbf{k}\mathbf{E}] = 0, \tag{2.45}$$

which, assuming biaxial permittivity can be rewritten in the matrix form as

$$\begin{bmatrix} \varepsilon_{xx} - \nu_y^2 - \nu_z^2 & 0 & 0 \\ 0 & \varepsilon_{yy} - \nu_z^2 & \nu_y\nu_z \\ 0 & \nu_y\nu_z & \varepsilon_{zz} - \nu_y^2 \end{bmatrix} = \begin{bmatrix} E_x \\ E_y \\ E_z \end{bmatrix}, \tag{2.46}$$

where the electric field can be expressed through the eigen-polarization $\mathbf{e}_j$, $j = x, y, z$ as

$$\mathbf{E}_{j0} = A_j\mathbf{e}_j, \tag{2.47}$$

A_j is the amplitude. Magnetic field is then similarly

$$\mathbf{H}_j = \frac{1}{\omega\mu_0}\mathbf{k}_j \times \mathbf{E}_j = \sqrt{\frac{\varepsilon_0}{\mu_0}}\mathbf{h}_j. \tag{2.48}$$

As with the isotropic case, we need to find the eigenvectors propagating through the structure. We start with finding the solution for ν_z. For (2.46) to have non-trivial solutions, determinant of the matrix must equal zero. The symmetry of the matrix allows us to divide the solution into two parts. The only non-zero element in the top row leads to two solutions

$$\nu_{z,1,3} = \pm\sqrt{\varepsilon_{xx} - \nu_y^2}, \tag{2.49}$$

as with the isotropic case and the solution to the remaining 2×2 matrix (its determinant equal zero) is

$$\nu_{z,2,4} = \pm\sqrt{\frac{\varepsilon_{yy}(\varepsilon_{zz} - \nu_y^2)}{\varepsilon_{zz}}} \tag{2.50}$$

We can again set the desired polarization as s ($e_x = 1$), with results same as in isotropic case and p ($h_x = 1$). To find the h_x elements, we start with last row

$$\nu_y \nu_z E_y + (\varepsilon_{zz} - \nu_y^2) E_z = 0. \tag{2.51}$$

For that equation to be true, we set

$$\begin{aligned} \nu_y \nu_z &= -E_z \\ (\varepsilon_{zz} - \nu_y^2) &= E_y, \end{aligned} \tag{2.52}$$

so that

$$\mathbf{E}_0 = \begin{bmatrix} 0 \\ \varepsilon_{zz} - \nu_y^2 \\ -\nu_y \nu_z \end{bmatrix} \tag{2.53}$$

and thus the magnetic field is

$$\mathbf{H}_0 = \begin{bmatrix} \nu_y E_z - \nu_z E_y \\ 0 \\ 0 \end{bmatrix}, \tag{2.54}$$

with the elements H_x as

$$H_x = \nu_y(-\nu_y \nu_z) - \nu_z(\varepsilon_{zz} - \nu_y^2) = -\nu_z \varepsilon_{zz} = \pm\sqrt{\varepsilon_{zz}\varepsilon_{yy}(\varepsilon_{yy} - \nu_y^2)}, \tag{2.55}$$

plus for up mode and minus for down mode. The **T**-matrix of the biaxial layer is

$$\mathbf{T}_{biaxial} = \begin{bmatrix} 1 & 1 & 0 & 0 \\ \sqrt{\varepsilon_{xx} - \nu_y^2} & -\sqrt{\varepsilon_{xx} - \nu_y^2} & 0 & 0 \\ 0 & 0 & \varepsilon_{zz} - \nu_y^2 & \varepsilon_{zz} - \nu_y^2 \\ 0 & 0 & -\sqrt{\varepsilon_{zz}\varepsilon_{yy}(\varepsilon_{zz} - \nu_y^2)} & \sqrt{\varepsilon_{zz}\varepsilon_{yy}(\varepsilon_{zz} - \nu_y^2)} \end{bmatrix}, \tag{2.56}$$

with the same ordering of modes as the isotropic **T** matrix.

Boundary conditions, M-matrix

Now we obtained the eigenmodes and eigenvalues for each layer of our system and we need to connect then together. Geometry of our system is shown in Figure 2.4. We do this by connecting tangential field component vector at boundaries. As we know, the tangential components must equal at the boundary. The tangential components vector in the n-th layer is expressed using matrices **T**, **V**, and the vector of amplitudes **A**:

$$\mathbf{F}^{(n)}(\mathbf{r}, t) = \mathbf{T}^{(n)} \exp\left[\mathrm{i}k_0 z_n \mathbf{V}^{(n)}\right] \mathbf{A}^{(n)} \exp\left[i(k_0\nu_x x + k_0\nu_y y - \omega t)\right]. \tag{2.57}$$

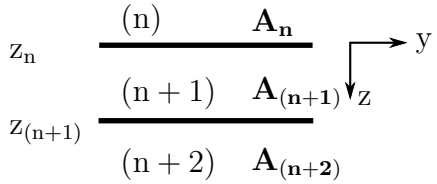

Figure 2.4: Ordering of the layers

Since the tangential components must equal at each boundary, we can write

$$\mathbf{T}^{(n)} \exp\left[\mathrm{i}k_0 z_n \mathbf{V}^{(n)}\right] \mathbf{A}^{(n)} = \mathbf{T}^{(n+1)} \exp\left[\mathrm{i}k_0 z_n \mathbf{V}^{(n+1)}\right] \mathbf{A}^{(n+1)}. \tag{2.58}$$

Expression $\exp\left[i(k_0\nu_x x + k_0\nu_y y - \omega t)\right]$ is same throughout the system, therefore is factored out of the equation. By the same approach, we link any neighboring layers. Notion for $n+1$ layer with $n+2$ layer yields

$$\mathbf{T}^{(n+1)} \exp\left[\mathrm{i}k_0 z_{n+1} \mathbf{V}^{(n+1)}\right] \mathbf{A}^{(n+1)} = \mathbf{T}^{(n+2)} \exp\left[\mathrm{i}k_0 z_{n+1} \mathbf{V}^{(n+2)}\right] \mathbf{A}^{(n+2)}. \tag{2.59}$$

Expression $\exp\left[-\mathrm{i}k_0 z_{n+1} \mathbf{V}^{(n+1)}\right]$ is for simplification labeled $\mathbf{P}^{(n+1)}$ and has the meaning as propagation factor through the layer with thickness $z_n - z_{n+1}$. Note the negative

sign in the exponent, it is because we shall do the inverse of this matrix. And so we can express $\mathbf{A}^{(n+1)}$ as

$$\mathbf{A}^{(n+1)} = \mathbf{P}^{(n+1)} \left[\mathbf{T}^{(n+1)}\right]^{-1} \mathbf{T}^{(n+2)} \exp\left[\mathrm{i}k_0 z_{n+1} \mathbf{V}^{(n+2)}\right] \mathbf{A}^{(n+2)} \tag{2.60}$$

and substitute it into (2.58), resulting in

$$\begin{aligned} &\mathbf{T}^{(n)} \exp\left[\mathrm{i}k_0 z_n \mathbf{V}^{(n+1)}\right] \mathbf{A}^{(n)} = \\ &\mathbf{T}^{(n+1)} \mathbf{P}^{(n+1)} \left[\mathbf{T}^{(n+1)}\right]^{-1} \mathbf{T}^{(n+2)} \exp\left[\mathrm{i}k_0 z_{n+1} \mathbf{V}^{(n+2)}\right] \mathbf{A}^{(n+2)}. \end{aligned} \tag{2.61}$$

By connecting all the following N layers using N-1 boundary conditions, we shall get a matrix, describing the whole system of layers, called **M**-matrix, or total transfer matrix [87], derived as

$$\mathbf{A}^{(0)} = \left[\mathbf{T}^{(0)}\right]^{-1} \prod_{m=1}^{N-1} \left(\mathbf{T}^{(m)} \mathbf{P}^{(m)} \left[\mathbf{T}^{(m)}\right]^{-1}\right) \mathbf{T}^{(N)} \mathbf{A}^{(N)} = \mathbf{M} \mathbf{A}^{(N)}. \tag{2.62}$$

2.1.5 Experimental observables

Reflection and transmission

In this section, we will be shown how to determine reflection coefficients and reflectivity from M-matrix. Elements of matrix M describe the relation between light amplitudes in the superstrate and substrate. For our case we shall consider light incident only from the superstrate. Providing the superstrate and substrate are isotropic and therefore the vectors are ordered, the notation (2.62) has the form

$$\begin{bmatrix} A^{(0)}_{s-down} \\ A^{(0)}_{s-up} \\ A^{(0)}_{p-down} \\ A^{(0)}_{p-up} \end{bmatrix} = \begin{bmatrix} M_{11} & M_{12} & M_{13} & M_{14} \\ M_{21} & M_{22} & M_{23} & M_{24} \\ M_{31} & M_{32} & M_{33} & M_{34} \\ M_{41} & M_{42} & M_{43} & M_{44} \end{bmatrix} \begin{bmatrix} A^{(N)}_{s-down} \\ 0 \\ A^{(N)}_{p-down} \\ 0 \end{bmatrix}. \tag{2.63}$$

Reflection coefficients are complex numbers that denote the ratio between reflected and incident wave. By the same logic, transmission coefficients are the ratio between propagated and incident wave, assuming that the amplitude of the other polarization is 0. They are expressed as

$$r_{ij}^{(kl)} = \frac{A_j^{(k)}}{A_i^{(k)}}, \qquad t_{ij}^{(kl)} = \frac{A_j^{(l)}}{A_i^{(k)}}, \tag{2.64}$$

where $k, l = \{0, N+1\}$, i and j can be either s or p, representing the polarization. We can easily deduce the analytical form of the four reflection coefficients:

$$r_{ss} = \frac{M_{21}M_{33} - M_{23}M_{31}}{M_{11}M_{33} - M_{31}M_{31}} \tag{2.65a}$$

$$r_{pp} = \frac{M_{41}M_{33} - M_{43}M_{31}}{M_{11}M_{33} - M_{31}M_{31}} \tag{2.65b}$$

$$r_{sp} = \frac{M_{11}M_{23} - M_{21}M_{13}}{M_{11}M_{33} - M_{31}M_{31}} \tag{2.65c}$$

$$r_{ps} = \frac{M_{11}M_{43} - M_{41}M_{13}}{M_{11}M_{33} - M_{31}M_{31}}. \tag{2.65d}$$

However, detected quantity is intensity, not amplitude. Intensity is defined as power through perpendicular surface and can be defined as

$$I = \frac{A^2}{2\eta} = \frac{\varepsilon^2}{2}\sqrt{\frac{\mu_0}{\varepsilon_0}}A^2. \tag{2.66}$$

Reflectivity, defined as ratio between reflected intensity and incident intensity has now this notion

$$R = \frac{I_r S_r}{I_i S_i}. \tag{2.67}$$

Surfaces of incident and reflected light are the same and we are in the same medium, so therefore

$$R_{ij} = \frac{I_r}{I_i} = |r_{ij}|^2. \tag{2.68}$$

Based on the established definitions in optical textbooks, [88] reflectivity is a material parameter, while reflectance is applied to multilayer systems, where the interference effects need to be accounted for. Here, they are both calculated using the same formula, as the absolute value of reflection coefficient squared. There is no distinction in this thesis between the reflectivity and reflectance.

2.1.6 Jones, Mueller matrices and Stokes vector

For the mathematical description of polarized light and components of optical setup it is very convenient to use either Jones formalism or Mueller formalism. They are equivalent for non-depolarizing samples. The Jones formalism uses vectors to describe the polarized light and matrices to describe optical components. The Jones vector consists of complex envelopes, as

$$\mathbf{J} = \begin{bmatrix} A_x \\ A_y \end{bmatrix} \tag{2.69}$$

Linear polarization occurs, when one of the elements A_x or A_y is zero or their phase difference is zero or π. Followings relations show the s- and p- representation, respectively.

$$\mathbf{J}_s = \begin{bmatrix} 1 \\ 0 \end{bmatrix}, \mathbf{J}_p = \begin{bmatrix} 0 \\ 1 \end{bmatrix}. \tag{2.70}$$

The intensity of the polarizer light is calculated as the product of Jones vector and its Hermitian adjoint $\mathbf{J}^+$, as

$$I = \mathbf{J}\mathbf{J}^+ = A_x^2 + A_y^2. \tag{2.71}$$

The polarization devices are described as a system that takes input wave $\mathbf{J}_1$ and returns output wave J_2,

$$\mathbf{J}_2 = \mathbf{T}_\mathbf{J}\mathbf{J}_1. \tag{2.72}$$

Hence $\mathbf{T}_\mathbf{J}$ is a 2×2 matrix with components

$$\mathbf{T}_\mathbf{J} = \begin{bmatrix} T_{1,1} & T_{1,2} \\ T_{2,1} & T_{2,2} \end{bmatrix}. \tag{2.73}$$

Frequently, in modern ellipsometry, a Mueller matrix description is needed. Here, the time-averaged polarized light is described by a 4-element Stokes vector, defined as

$$\mathbf{S} = \begin{bmatrix} S_0 \\ S_1 \\ S_2 \\ S_3 \end{bmatrix} = \begin{bmatrix} I_0 \\ I_x - I_y \\ I_{45} - I_{-45} \\ I_{\mathrm{RCP}} - I_{\mathrm{LCP}} \end{bmatrix} = \begin{bmatrix} A_x A_x^* + A_y A_y^* \\ A_x A_x^* - A_y A_y^* \\ 2\Re(A_x^* A_y) \\ 2\Im(A_x^* A_y) \end{bmatrix}. \tag{2.74}$$

The meaning of the elements is total intensity, difference between linearly polarized light in x and y direction, difference between linearly polarized light in $45°$ and $-45°$ and difference between right handed circularly polarized light and left handed circularly polarized light.

The Mueller matrix is the system that turns input wave $\mathbf{S}_1$ into output $\mathbf{S}_2$. It is therefore a 4×4 matrix. For non-depolarizing samples it can be calculated from the Jones matrix, through a coherency matrix $\mathbf{T}_\mathbf{C}$

$$\mathbf{T}_\mathbf{C} = \begin{bmatrix} T_{1,1}T_{1,1}^* & T_{1,1}T_{1,2}^* & T_{1,2}T_{1,1}^* & T_{1,2}T_{1,2}^* \\ T_{1,1}T_{2,1}^* & T_{1,1}T_{2,2}^* & T_{1,2}T_{2,1}^* & T_{1,2}T_{2,2}^* \\ T_{2,1}T_{1,1}^* & T_{2,1}T_{1,2}^* & T_{2,2}T_{1,1}^* & T_{2,2}T_{1,2}^* \\ T_{2,1}T_{2,1}^* & T_{2,1}T_{2,2}^* & T_{2,2}T_{2,1}^* & T_{2,2}T_{2,2}^* \end{bmatrix} \tag{2.75}$$

and transformation matrix

$$\mathbf{B} = \begin{bmatrix} 1 & 0 & 0 & 1 \\ 1 & 0 & 0 & -1 \\ 0 & 1 & 1 & 0 \\ 0 & -i & i & 0 \end{bmatrix} \tag{2.76}$$

as

$$\mathbf{M} = \mathbf{B}\mathbf{T}_\mathbf{C}\mathbf{B}^{-1}. \tag{2.77}$$

An example of Jones formalism in practice used in this work is a configuration polarizer-sample-analyzer. The polarizer and analyzer are polarization filters, rotated to desired angles $\theta_{1,2}$, respectively. The sample is described as the Jones matrix

$$\mathbf{T}_{\mathbf{J}S} = \begin{bmatrix} r_{ss} & r_{sp} \\ r_{ps} & r_{pp} \end{bmatrix}. \tag{2.78}$$

The whole system is then

$$\mathbf{J}_2 = \begin{bmatrix} \cos^2\theta_2 & \cos\theta_2 \sin\theta_2 \\ \cos\theta_2 \sin\theta_2 & \sin^2\theta_2 \end{bmatrix} \begin{bmatrix} r_{ss} & r_{sp} \\ r_{ps} & r_{pp} \end{bmatrix} \begin{bmatrix} \cos\theta_1 \\ \sin\theta_2 \end{bmatrix}. \tag{2.79}$$

The intensity of $\mathbf{J}_2$ is the measured and modeled quantity. This approach is used in Section 3.4.3 dor measurement of anisotropic data.

2.2 Rigorous Coupled Wave Analysis

The method for dealing with layers with periodic modulation of permittivity is called the Rigorous coupled wave analysis (RCWA). Fourier series are used for the description of lateral dependence of permittivity tensor and basically the algorithm for layers is repeated with expanded permittivity tensors and according to the Floquet-Bloch theorem also wave vectors of the gratings. As with layers, we start with Maxwell equations (2.11a) and (2.11b). This time, however the permittivity tensor will not have only 9 elements, but will be expanded using the Fourier series. Provided that permittivity has periodicity in y-direction (our case), Fourier series are in the form

$$\varepsilon_{ij}(\mathbf{r}) = \sum_{n=-\infty}^{\infty} \varepsilon_{ij,n} \exp\left[\mathrm{i}n\frac{2\pi}{\Lambda}y\right], \tag{2.80}$$

where Λ is the period of the profile and $\varepsilon_{ij,n}$ is the n-th Fourier coefficient of the series. The process is illustrated in Figure 2.5. The electromagnetic field in such media is

Figure 2.5: Illustration of the idea behind the RCWA. The permittivity profile of the grating (here rectangular) is expanded using the Fourier series. Fourier series are infinite, but we can take only finite number of modes. This causes a the ringing on permittivity profile.

also expanded using Fourier series with the same period. Expansion needs to be done for all the layers and it will give us all the diffracted modes which arise from this system. Next steps in the derivation can be simplified for the implementation to the matrix form. First, let us have the expanded field vectors

$$\mathbf{E}'(\mathbf{r}) = \sum_{n=-\infty}^{\infty} \mathbf{e}_n(z) \exp[\mathrm{i}k_0(\nu_x x + \nu_y y)] \exp\left[\mathrm{i}n\frac{2\pi}{\Lambda}y\right], \tag{2.81a}$$

$$\mathbf{H}'(\mathbf{r}) = \sum_{n=-\infty}^{\infty} \mathbf{h}_n(z) \exp[\mathrm{i}k_0(\nu_x x + \nu_y y)] \exp\left[\mathrm{i}n\frac{2\pi}{\Lambda}y\right]. \tag{2.81b}$$

Using (2.11a) and (2.11b) with the previous eq. yields

$$\nabla \times \sum_{n=-\infty}^{\infty} \mathbf{h}_n(z) \exp[\mathrm{i}k_0(\nu_x x + \nu_y y)] \exp\left[\mathrm{i}n\frac{2\pi}{\Lambda}y\right] =$$

$$= -\mathrm{i}k_0 \sum_{n=-\infty}^{\infty} \sum_{m=-\infty}^{\infty} \hat{\varepsilon}_{ij,n} \mathbf{e}_m(z) \exp[\mathrm{i}k_0(\nu_x x + \nu_y y)] \exp\left[\mathrm{i}n\frac{2\pi}{\Lambda}y\right], \tag{2.82a}$$

$$\nabla \times \sum_{n=-\infty}^{\infty} \mathbf{e}_n(z) \exp[\mathrm{i}k_0(\nu_x x + \nu_y y)] \exp\left[\mathrm{i}n\frac{2\pi}{\Lambda}y\right] =$$

$$= \mathrm{i}k_0 \sum_{n=-\infty}^{\infty} \mathbf{h}_n(z) \exp[\mathrm{i}k_0(\nu_x x + \nu_y y)] \exp\left[\mathrm{i}n\frac{2\pi}{\Lambda}y\right] \tag{2.82b}$$

By using the compact matrix notation, we arrive at

$$\nabla \times \{\mathrm{F}\lceil\mathbf{h}(z)\rceil \exp[\mathrm{i}k_0(\nu_x x + \nu_y y)]\} = -\mathrm{i}k_0 \mathrm{F}\langle\hat{\varepsilon}\rangle\lceil\mathbf{e}(z)\rceil \exp[\mathrm{i}k_0(\nu_x x + \nu_y y)] \tag{2.83a}$$

$$\nabla \times \{\mathrm{F}\lceil\mathbf{e}(z)\rceil \exp[\mathrm{i}k_0(\nu_x x + \nu_y y)]\} = \mathrm{i}k_0 \mathrm{F}\lceil\mathbf{h}(z)\rceil \exp[\mathrm{i}k_0(\nu_x x + \nu_y y)], \tag{2.83b}$$

where the matrix $\mathbf{F}$ is $(2N+1) \times (2N+1)$ matrix with Fourier exponents on its diagonal, N being the number of chosen diffraction orders (total number of orders is $2N+1$ - negative, zeroth, and positive), symbol $\lceil . \rceil$ denotes the amplitudes of Fourier

series expansion and $\langle . \rangle$ is the Toeplitz matrix, defined as

$$\langle A \rangle = \begin{bmatrix} a_0 & a_{-1} & a_{-2} & \cdots & a_N \\ a_1 & a_0 & a_{-1} & \ddots & \vdots \\ a_2 & a_1 & a_0 & \ddots & a_{-2} \\ \vdots & \ddots & \ddots & \ddots & a_{-1} \\ a_N & \cdots & a_2 & a_1 & a_0 \end{bmatrix}. \tag{2.84}$$

For clarification, the $\mathbf{F}$ matrix can be written using the Kronecker delta

$$\mathbf{F} = \delta_{ij} \exp\left[\left((i(j-N-1)n\frac{2\pi}{\Lambda}y\right]\right). \tag{2.85}$$

The rest of the algorithm is basically the same as for layered system, however here we need to be mindful about order of operation, since nearly all values have matrix or vector form. Now we evaluate the curl operator and we can easily see, that the F matrices cancel each other out. This gives us equations

$$\begin{bmatrix} 0 & -\frac{\partial}{\partial z} & \mathrm{i}k_0\mathbf{q} \\ \frac{\partial}{\partial z} & 0 & -\mathrm{i}k_0\mathbf{p} \\ -\mathrm{i}k_0\mathbf{q} & \mathrm{i}k_0\mathbf{p} & 0 \end{bmatrix} \begin{bmatrix} \lceil h_x(z) \rceil \\ \lceil h_y(z) \rceil \\ \lceil h_z(z) \rceil \end{bmatrix} = -ik_0 \begin{bmatrix} \langle \varepsilon_{xx} \rangle & \langle \varepsilon_{xy} \rangle & \langle \varepsilon_{xz} \rangle \\ \langle \varepsilon_{yx} \rangle & \langle \varepsilon_{yy} \rangle & \langle \varepsilon_{yz} \rangle \\ \langle \varepsilon_{zx} \rangle & \langle \varepsilon_{zy} \rangle & \langle \varepsilon_{zz} \rangle \end{bmatrix} \begin{bmatrix} \lceil e_x(z) \rceil \\ \lceil e_y(z) \rceil \\ \lceil e_z(z) \rceil \end{bmatrix} \tag{2.86a}$$

$$\begin{bmatrix} 0 & -\frac{\partial}{\partial z} & \mathrm{i}k_0\mathbf{q} \\ \frac{\partial}{\partial z} & 0 & -\mathrm{i}k_0\mathbf{p} \\ -\mathrm{i}k_0\mathbf{q} & \mathrm{i}k_0\mathbf{p} & 0 \end{bmatrix} \begin{bmatrix} \lceil e_x(z) \rceil \\ \lceil e_y(z) \rceil \\ \lceil e_z(z) \rceil \end{bmatrix} = \mathrm{i}k_0 \begin{bmatrix} \lceil h_x(z) \rceil \\ \lceil h_y(z) \rceil \\ \lceil h_z(z) \rceil \end{bmatrix}, \tag{2.86b}$$

where the $\mathbf{p}$ and $\mathbf{q}$ are $(2N+1)\times(2N+1)$ matrices represent the tangential components of the diffracted modes, with elements defined as

$$p_{ij} = \delta_{ij}\nu_x, \tag{2.87a}$$

$$q_{ij} = \delta_{ij}\left[\nu_y + (j-N-1)\frac{\lambda}{\Lambda}\right]. \tag{2.87b}$$

Vector $\mathbf{f}$(z) ((2.30)) is also expanded in the form

$$\lceil \mathbf{f}(z) \rceil = [\lceil e_x(z) \rceil, \lceil h_y(z) \rceil, \lceil e_y(z) \rceil, \lceil h_x(z) \rceil]^T. \tag{2.88}$$

With repeating the procedures from the layer algorithm (expression of normal components, rearrangement), we obtain similar set of differential equations:

$$\frac{\partial}{\partial z}\lceil \mathbf{f}(z) \rceil = ik_0\mathbf{C}\lceil \mathbf{f}(z) \rceil. \tag{2.89}$$

C-matrix is now 4(2N+1) × 4(2N+1) large, with ν_x and ν_y replaced by **p** and **q** matrices, respectively, and every element of permittivity tensor expanded in the form of the Toeplitz matrix, resulting in

$$\mathbf{C} = [\mathbf{C}_1, \mathbf{C}_2, \mathbf{C}_4, \mathbf{C}_4]\,, \tag{2.90a}$$

$$\mathbf{C}_1 = \begin{bmatrix} -\mathbf{p}\langle\varepsilon_{zz}\rangle^{-1}\langle\varepsilon_{zx}\rangle \\ -\mathbf{q}^2 + \langle\varepsilon_{xx}\rangle - \langle\varepsilon_{xz}\rangle\langle\varepsilon_{zz}\rangle^{-1}\langle\varepsilon_{zx}\rangle \\ -\mathbf{q}\langle\varepsilon_{zz}\rangle^{-1}\langle\varepsilon_{zx}\rangle \\ -\mathbf{pq} - \langle\varepsilon_{yx}\rangle + \langle\varepsilon_{yz}\rangle\langle\varepsilon_{zz}\rangle^{-1}\langle\varepsilon_{zx}\rangle \end{bmatrix}, \tag{2.90b}$$

$$\mathbf{C}_2 = \begin{bmatrix} \mathrm{I} - \mathbf{p}\langle\varepsilon_{zz}\rangle^{-1}\mathbf{p} \\ -\langle\varepsilon_{xz}\rangle\langle\varepsilon_{zz}\rangle^{-1}\mathbf{p} \\ -\mathbf{q}\langle\varepsilon_{zz}\rangle^{-1}\mathbf{p} \\ \langle\varepsilon_{yz}\rangle\langle\varepsilon_{zz}\rangle^{-1}\mathbf{p} \end{bmatrix}, \tag{2.90c}$$

$$\mathbf{C}_3 = \begin{bmatrix} -\mathbf{p}\langle\varepsilon_{zz}\rangle^{-1}\langle\varepsilon_{zy}\rangle \\ \mathbf{qp} + \langle\varepsilon_{xy}\rangle - \langle\varepsilon_{xz}\rangle\langle\varepsilon_{zz}\rangle^{-1}\langle\varepsilon_{zy}\rangle \\ -\mathbf{q}\langle\varepsilon_{zz}\rangle^{-1}\langle\varepsilon_{zy}\rangle \\ \mathbf{p}^2 - \langle\varepsilon_{yy}\rangle + \langle\varepsilon_{yz}\rangle\langle\varepsilon_{zz}\rangle^{-1}\langle\varepsilon_{zy}\rangle \end{bmatrix}, \tag{2.90d}$$

$$\mathbf{C}_4 = \begin{bmatrix} \mathbf{p}\langle\varepsilon_{zz}\rangle^{-1}\mathbf{q} \\ \langle\varepsilon_{xz}\rangle\langle\varepsilon_{zz}\rangle^{-1}\mathbf{q} \\ -\mathbf{q}\langle\varepsilon_{zz}\rangle^{-1}\mathbf{q} - \mathrm{I} \\ -\langle\varepsilon_{yz}\rangle\langle\varepsilon_{zz}\rangle^{-1}\mathbf{q} \end{bmatrix}. \tag{2.90e}$$

Equation (2.89) is solved in the same way as with the layered structure. For each layer we find T and V matrices by calculating the eigenvalues and eigenvectors of expanded matrix C. Solution for isotropic layer is not only possible, but necessary. With knowledge of which vector corresponds to what wave, we are able to calculate experimental observables. The algorithm is rather robust, so we just need to know the ordering for superstrate and substrate and solution in the inner layers can be just ordered in up-down fashion, which easily recognizable from sign convention.

2.2.1 Scattering matrix algorithm

There is one significant problem with calculating measurable quantities of layers with gratings. Due to use of higher diffraction orders, the arguments of exponential function are higher and the algorithm looses its numerical precision. Therefore we use a different algorithm called the scattering matrix algorithm, or the S-matrix algorithm [89]. The idea behind S-matrix algorithm is to separate up and down modes and sum or subtract them them in opposite direction, thus modifying the exponential arguments. It is also convenient to use the S-matrix, because its components have direct meaning as reflection and transmission coefficients of the system.

S-matrix definition

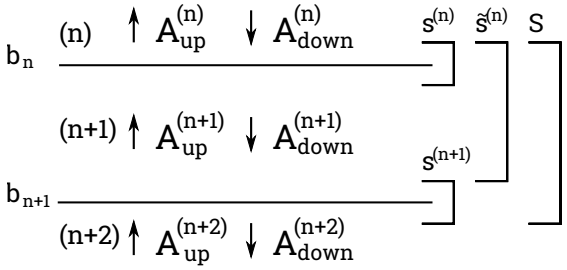

Figure 2.6: S-matrix geometry

S-matrix algorithm can be explained in few steps. Figure 2.6 shows the necessary geometry. Let us have the $\mathbf{T}$- and $\mathbf{V}$-matrices for our layers/gratings. These matrices must be rearranged and up and down modes must be separated. Then we can use the formula for relation between amplitudes

$$\mathbf{A}^{(n)}_{(b_n)} = \underbrace{(\mathbf{T}^{(n)})^{-1}\mathbf{T}^{(n+1)}}_{\mathbf{M}^{(n)}}\mathbf{A}^{(n+1)}_{(b_n)}. \tag{2.91}$$

With separated modes the previous equation is

$$\begin{bmatrix} \mathbf{A}^{(n)}_{up(b_n)} \\ \mathbf{A}^{(n)}_{down(b_n)} \end{bmatrix} = \begin{bmatrix} \mathbf{M}^{(n)}_{11} & \mathbf{M}^{(n)}_{12} \\ \mathbf{M}^{(n)}_{21} & \mathbf{M}^{(n)}_{22} \end{bmatrix} \begin{bmatrix} \mathbf{A}^{(n+1)}_{up(b_n)} \\ \mathbf{A}^{(n+1)}_{down(b_n)} \end{bmatrix} \tag{2.92}$$

and we rearrange this relation to satisfy our S-matrix idea of connecting in and out

amplitudes, as

$$\begin{bmatrix} \mathbf{A}^{(n)}_{up(b_n)} \\ \mathbf{A}^{(n+1)}_{down(b_n)} \end{bmatrix} = \underbrace{\begin{bmatrix} \mathbf{s}^{(n)}_{11} & \mathbf{s}^{(n)}_{12} \\ \mathbf{s}^{(n)}_{21} & \mathbf{s}^{(n)}_{22} \end{bmatrix}}_{\mathbf{s}^{(n)}} \begin{bmatrix} \mathbf{A}^{(n+1)}_{up(b_n)} \\ \mathbf{A}^{(n)}_{down(b_n)} \end{bmatrix}, \tag{2.93}$$

where the elements of $\mathbf{s}^{(n)}$ matrix are easily derived as follows:

$$\begin{bmatrix} \mathbf{s}^{(n)}_{11} & \mathbf{s}^{(n)}_{12} \\ \mathbf{s}^{(n)}_{21} & \mathbf{s}^{(n)}_{22} \end{bmatrix} = \begin{bmatrix} \mathbf{M}^{(n)}_{11} - \mathbf{M}^{(n)}_{12}\mathbf{M}^{(n)^{-1}}_{22}\mathbf{M}^{(n)}_{21} & \mathbf{M}^{(n)}_{12}\mathbf{M}^{(n)^{-1}}_{22} \\ -\mathbf{M}^{(n)^{-1}}_{22}\mathbf{M}^{(n)}_{21} & \mathbf{M}^{(n)^{-1}}_{22} \end{bmatrix} = \begin{bmatrix} \tilde{\mathbf{T}} & \mathbf{R} \\ \tilde{\mathbf{R}} & \mathbf{T} \end{bmatrix}. \tag{2.94}$$

Now for a single boundary, relation (2.93) is satisfactory and gives us the necessary measurable quantities. For layers and gratings, there are two more challenges: including the propagation in the layers to the algorithm and tying of consequential layers together in the s-matrix of the whole system. First, let us look at the propagation problem. As we now know, propagation in layers is described by matrix $\mathbf{P}$. Here we repeat the separation of *up* and *down* modes and include the propagation matrices in the algorithm:

$$\mathbf{A}^{(n+1)}_{up(b_n)} = \mathbf{P}^{(n+1)}_{up}\mathbf{A}^{(n+1)}_{up(b_{n+1})} \tag{2.95a}$$

$$\mathbf{A}^{(n+1)}_{down(b_n)} = \mathbf{P}^{(n+1)}_{down}\mathbf{A}^{(n+1)}_{down(b_{n+1})}. \tag{2.95b}$$

Now we can define matrix $\tilde{s}$ and its elements:

$$\begin{bmatrix} \mathbf{A}^{(n)}_{up(b_n)} \\ \mathbf{A}^{(n+1)}_{down(b_{n+1})} \end{bmatrix} = \underbrace{\begin{bmatrix} \mathbf{s}^{(n)}_{11}\mathbf{P}^{(n+1)}_{up} & \mathbf{s}^{(n)}_{12} \\ \mathbf{P}^{(n+1)}_{down}\mathbf{s}^{(n)}_{21}\mathbf{P}^{(n+1)}_{up} & \mathbf{P}^{(n+1)}_{down}\mathbf{s}^{(n)}_{22} \end{bmatrix}}_{\tilde{\mathbf{s}}^{(n)}} \begin{bmatrix} \mathbf{A}^{(n+1)}_{up(b_{n+1})} \\ \mathbf{A}^{(n)}_{down(b_n)} \end{bmatrix}. \tag{2.96}$$

Note that if $\mathbf{P}^{(n+1)}_{up}$ and $\mathbf{P}^{(n+1)}_{down}$ were equal, the equation (2.96) would have to have the $\mathbf{P}^{(n+1)}_{down}$ matrices inverted. However, for the sake of numerical implementation of this algorithm and the nature of P-matrices, it is easier to express them in the following fashion a thus eliminating the necessity of using inversion in our algorithm:

$$\mathbf{P}^{(n+1)}_{up} = \exp(-\mathrm{i}k_0 d_{n+1}\mathbf{V}_{up}), \tag{2.97a}$$

$$\mathbf{P}^{(n+1)}_{down} = \exp(\mathrm{i}k_0 d_{n+1}\mathbf{V}_{down}). \tag{2.97b}$$

The goal is to link incident and outgoing amplitudes of the whole system. Unlike M-matrix, here we have to connect all $\tilde{\mathrm{s}}$ matrices recurrently. In the equation

$$\begin{bmatrix} \mathbf{A}^{(n)}_{up(b_n)} \\ \mathbf{A}^{(n+2)}_{down(b_n+1)} \end{bmatrix} = \mathbf{S} \begin{bmatrix} \mathbf{A}^{(n+2)}_{up(b_{n+1})} \\ \mathbf{A}^{(n)}_{down(b_n)} \end{bmatrix} \tag{2.98}$$

the elements of the S - matrix are defined:

$$\mathbf{S}_{11} = \tilde{\mathbf{s}}_{11}^{(n)}(\mathbf{I} - \tilde{\mathbf{s}}_{12}^{(n+1)}\mathbf{s}_{21}^{(n)})^{-1}\mathbf{s}_{11}^{(n+1)}, \tag{2.99a}$$

$$\mathbf{S}_{12} = \tilde{\mathbf{s}}_{12}^{(n)} + \tilde{\mathbf{s}}_{11}^{(n)}(\mathbf{I} - \tilde{\mathbf{s}}_{12}^{(n+1)}\mathbf{s}_{21}^{(n)})^{-1}\mathbf{s}_{12}^{(n+1)}\tilde{\mathbf{s}}_{22}^{(n)}, \tag{2.99b}$$

$$\mathbf{S}_{21} = \mathbf{s}_{22}^{(n+1)}\tilde{\mathbf{s}}_{21}^{(n)}(\mathbf{I} - \tilde{\mathbf{s}}_{12}^{(n+1)}\mathbf{s}_{21}^{(n)})^{-1}\mathbf{s}_{11}^{(n+1)} + \mathbf{s}_{21}^{(n+1)}, \tag{2.99c}$$

$$\mathbf{S}_{22} = \mathbf{s}_{22}^{(n+1)}[\mathbf{I} + \tilde{\mathbf{s}}_{21}^{(n)}(\mathbf{I} - \tilde{\mathbf{s}}_{12}^{(n+1)}\mathbf{s}_{21}^{(n)})^{-1}\mathbf{s}_{12}^{(n+1)}]\tilde{\mathbf{s}}_{22}^{(n)}. \tag{2.99d}$$

In the same fashion as with (2.98) and (2.99), always adding the following $\tilde{\mathrm{s}}$ matrix to the newly calculated S-matrix, we can deduce the complete S-matrix of the system, that being:

$$\begin{bmatrix} \mathbf{A}_{up(b_0)}^{(0)} \\ \mathbf{A}_{down(b_N-1)}^{(N)} \end{bmatrix} = \mathbf{S} \begin{bmatrix} \mathbf{A}_{up(b_{N-1})}^{(N)} \\ \mathbf{A}_{down(b_0)\cdot}^{(0)} \end{bmatrix} \tag{2.100}$$

Physical meaning of the S-matrix elements

One of the benefits of using S-matrix is the fact that we obtain the direct measurable quantities. S-matrix can be broken into 4 sectors

$$\begin{bmatrix} \mathbf{A}_{up(b_0)}^{(0)} \\ \mathbf{A}_{down(b_N-1)}^{(N)} \end{bmatrix} = \begin{bmatrix} \tilde{\mathbf{t}} & r \\ \tilde{\mathbf{r}} & t \end{bmatrix} \begin{bmatrix} \mathbf{A}_{up(b_{N-1})}^{(N)} \\ \mathbf{A}_{down(b_0)\cdot}^{(0)} \end{bmatrix}. \tag{2.101}$$

Each sector contains optical coefficients matching its label. The symbol tilde symbol here denotes the backward coefficients, for layer incident on the substrate. The structure of each sector can be easily deduced from (2.64). For $N = 1$, sector r is composed

$$r = \begin{bmatrix} \square & \square & \square & \square & \square & \square \\ r_{ss}^{(-1)} & r_{ss}^{(0)} & r_{ss}^{(1)} & r_{ps}^{(-1)} & r_{ps}^{(0)} & r_{ps}^{(1)} \\ \square & \square & \square & \square & \square & \square \\ \square & \square & \square & \square & \square & \square \\ r_{sp}^{(-1)} & r_{sp}^{(0)} & r_{sp}^{(1)} & r_{pp}^{(-1)} & r_{pp}^{(0)} & r_{pp}^{(1)} \\ \square & \square & \square & \square & \square & \square \end{bmatrix}. \tag{2.102}$$

Elements replaced with box have very little physical meaning and are hard to obtain from experiments. Elements for other sectors are defined in a similar way.

2.2.2 Grating profiles

Harmonic modulation

In this subsection we shall look on how the calculation is done for harmonic modulation of dielectric function. First, we need to take a look on the Fourier series, the hearth of grating solutions. Let's have a real valued function $f(y)$ with periodicity Λ. Its corresponding complex Fourier series is defined as

$$f(y) = \sum_{n=-\infty}^{\infty} A_n e^{i(n2\pi y/\Lambda)}. \tag{2.103}$$

The Fourier component A_n can be expressed as

$$A_n = \frac{1}{\Lambda} \int_{-\frac{\Lambda}{2}}^{\frac{\Lambda}{2}} f(y) e^{-i(n2\pi y/\Lambda)} dy. \tag{2.104}$$

For harmonic modulation of permittivity tensor, we can choose either sine or cosine function. The remaining function can be always calculated using phase shift $\frac{\pi}{2}$. Cosine function is odd and thereby the integration is somewhat simpler. So let's choose

$$f(y) = a \cos\left(\frac{2\pi y}{\Lambda} + \phi\right) + b, \tag{2.105}$$

where ϕ is the phase shift. Integration (2.104) yields only three nonzero amplitudes

$$\begin{aligned} A_{-1} &= \frac{1}{2} a e^{-i\phi}, \\ A_0 &= b, \\ A_{+1} &= \frac{1}{2} a e^{i\phi}. \end{aligned} \tag{2.106}$$

However, for numerical accuracy, higher zero modes must be taken into account. The number of diffraction modes needed in the calculation is determined by a convergence tests, where we follow a observable quantity with increasing number of diffraction orders and find a sufficient number of orders, where the value converges. For the implementation, we need to determine the values of a and b. We set upper ε_{max} and lower ε_{min} limit, between which the permittivity value should oscillate. That gives us

$$\begin{aligned} a &= \frac{\varepsilon_{max} - \varepsilon_{min}}{2}, \\ b &= \frac{\varepsilon_{max} + \varepsilon_{min}}{2}. \end{aligned} \tag{2.107}$$

The Toeplitz matrix of $N = 1$ has the form

$$\varepsilon_{ij} = \begin{bmatrix} \frac{\varepsilon_{max}+\varepsilon_{min}}{2} & \frac{\varepsilon_{max}-\varepsilon_{min}}{4}e^{-i\phi} & 0 \\ \frac{\varepsilon_{max}-\varepsilon_{min}}{4}e^{i\phi} & \frac{\varepsilon_{max}+\varepsilon_{min}}{2} & \frac{\varepsilon_{max}-\varepsilon_{min}}{4}e^{-i\phi} \\ 0 & \frac{\varepsilon_{max}-\varepsilon_{min}}{4}e^{i\phi} & \frac{\varepsilon_{max}+\varepsilon_{min}}{2} \end{bmatrix}. \tag{2.108}$$

For higher orders, the rules to follow for Toeplitz matrix elements $a_{i,j}$, i, j being the indices in matrix, are

$$\begin{aligned} a_{i=j} &= A_0 \\ a_{i=j-1} &= A_{-1} \\ a_{j=i-1} &= A_{+1}, \end{aligned} \tag{2.109}$$

with all other elements zero.

Lamellar grating

Another important (perhaps the defining) example of grating is the 1D lamellar grating, shown in Figure 2.7. It consist of two lamellas made from materials ε_1 and ε_2 and repeated with period Λ. The lamellas have the same thickness d and the respective widths w_1 and w_2. The ratio of the widths is called the fill factor $f = \frac{w_2}{w_1}$. The Toeplitz matrix needed for the calculation of RCWA is derived the same way as for the harmonic grating. Now the function $f(y)$ in (2.104) is a step function with values ε_1 and ε_2

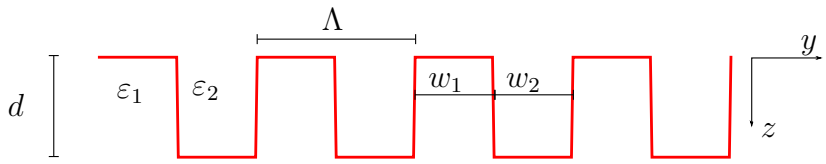

Figure 2.7: 1D lamellar grating

The Fourier amplitudes up to order N for the lamellar grating are

$$\begin{aligned} A_0 &= f\varepsilon_1 + (1-f)\varepsilon_2 \\ A_{n=2:N} &= \frac{\varepsilon_1}{-2i\pi n}[\exp(-2i\pi nf) - 1] + \frac{\varepsilon_2}{-2i\pi n}[\exp(-2i\pi n) - \exp(-2i\pi nf)] \\ A_{-n=-2:-N} &= \frac{\varepsilon_1}{2i\pi n}[\exp(2i\pi nf) - 1] + \frac{\varepsilon_2}{2i\pi n}[\exp(2i\pi n) - \exp(2i\pi nf)]. \end{aligned} \tag{2.110}$$

These elements make up the Toeplitz matrix of the lamellar grating. Li's Fourier factorization is used to improve the accuracy of numerical calculations of lamellar gratings made of conductive materials [90]. The same approach for factorization of lamellar gratings is used for derivation of effective medium approximation, described in the next section.

2.2.3 Effective medium approximation

When the period of grating is much smaller then the wavelength, it behaves as an anisotropic layer without any diffraction - only the specular reflection and transmission from the grating occur. In this case the optical response of the grating can be described using the effective medium. The effective anisotropy can be mathematically described and gives us analytical insight into the behavior of subwavelength gratings without a need to rely on the complex and demanding numerical computation. This approach has been established for lamellar gratings, here we extend it to the harmonic gratings.

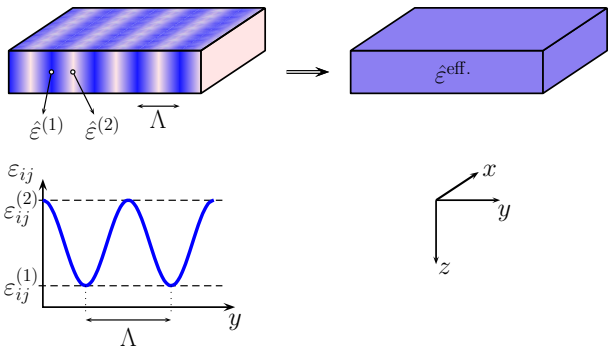

Figure 2.8: Grating with sinusoidal variation of permittivity tensor by is described by the effective medium approximation. The coordinate system used in this paper is shown.

Figure 2.8 shows schematically the main target of this section. The anisotropic grating with sinusoidal profiles of the permittivity tensor components is described using the effective permittivity tensor $\hat{\varepsilon}^{\text{eff.}}$. Lower subplot shows lateral variation of the permittivity tensor component ε_{ij}, which oscillate between the values $\varepsilon_{ij}^{(1)}$ and $\varepsilon_{ij}^{(2)}$. Calculation of the effective parameters using the rigorous RCWA method is presented in Sec. 4.3.3 and validity of EMA is discussed.

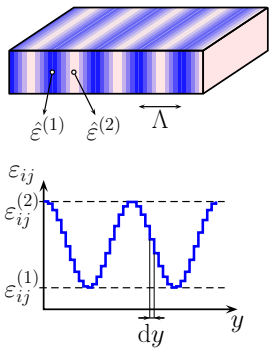

Figure 2.9: Description of continuously modulated sinusoidal grating using fine lamellar grating.

In this section the procedure to derive analytical forms of the effective medium tensor components in the quasistatic approximation ($\Lambda \ll \lambda$) is presented. It is based on ensuring of the boundary conditions for the field components perpendicular to the grating gradient. For this purpose we approximate the continuosly modulated grating using a lamellar grating as schematically shown in Figure 2.9.

Here we generalize the procedure to obtain the effective parameters of lamellar grating presented by Foldyna et al. [76]. The effective permittivity is calculated as a weighted average of the permittivity profile including proper Fourier factorization, which represents the zero-order (quasistatic) approximation of RCWA [76]. The factorization is performed in y-direction, which represents the highest gradient of the profile. This approach is extandable to any arbitrary modulation of the permittivity tensor components $\varepsilon_{ij}(y)$.

We perform the calculation in three steps. First, the permittivity tensor is transformed in order to ensure continuity boundary conditions inside the grating. On layers, we have to tangential components of electric field continuous, but with the addition of gratings in y direction, the boundary is normal to the field in the y direction. This leads to discontinuity in the field calculation. We take the material relation of electric displacement and field

$$\begin{bmatrix} D_x \\ D_y \\ D_z \end{bmatrix} = \hat{\varepsilon} \begin{bmatrix} E_x \\ E_y \\ E_z \end{bmatrix} \tag{2.111}$$

and regroup it into

$$\begin{bmatrix} D_x \\ D_z \\ E_y \end{bmatrix} = \hat{\mathcal{E}}(y) \begin{bmatrix} E_x \\ E_z \\ D_y \end{bmatrix}, \tag{2.112}$$

which relates continuous (right) and discontinuous (left) field components. Tensor $\hat{\mathcal{E}}(y)$ is defined as

$$\hat{\mathcal{E}}(y) = \begin{bmatrix} \varepsilon_{xx} - \varepsilon_{xy}\varepsilon_{yy}^{-1}\varepsilon_{yx} & \varepsilon_{xz} - \varepsilon_{xy}\varepsilon_{yy}^{-1}\varepsilon_{yz} & \varepsilon_{xy}\varepsilon_{yy}^{-1} \\ \varepsilon_{zx} - \varepsilon_{zy}\varepsilon_{yy}^{-1}\varepsilon_{yx} & \varepsilon_{zz} - \varepsilon_{zy}\varepsilon_{yy}^{-1}\varepsilon_{yz} & \varepsilon_{zy}\varepsilon_{yy}^{-1} \\ -\varepsilon_{yy}^{-1}\varepsilon_{yx} & -\varepsilon_{yy}^{-1}\varepsilon_{yz} & \varepsilon_{yy}^{-1} \end{bmatrix}. \tag{2.113}$$

In the second step its components are averaged using the integral

$$\mathcal{E}_{ij}^{\text{eff}} = \frac{1}{\Lambda}\int_0^{\Lambda} \mathcal{E}_{ij}(y)\,\mathrm{d}y \tag{2.114}$$

and finally we transform the effective components of the tensor $\mathcal{E}^{\text{eff}}$ back to the effective permittivity tensor

$$\begin{bmatrix} D_x \\ D_y \\ D_z \end{bmatrix} = \hat{\varepsilon}^{\text{eff}} \begin{bmatrix} E_x \\ E_y \\ E_z \end{bmatrix} \tag{2.115}$$

of the grating with modulated optical parameters

$$\hat{\varepsilon}^{\text{eff}} = \begin{bmatrix} \mathcal{E}_{11}^{\text{eff}} - \mathcal{E}_{13}^{\text{eff}}\left[\mathcal{E}_{33}^{\text{eff}}\right]^{-1}\mathcal{E}_{31}^{\text{eff}} & \mathcal{E}_{13}^{\text{eff}}\left[\mathcal{E}_{33}^{\text{eff}}\right]^{-1} & \mathcal{E}_{12}^{\text{eff}} - \mathcal{E}_{13}^{\text{eff}}\left[\mathcal{E}_{33}^{\text{eff}}\right]^{-1}\mathcal{E}_{32}^{\text{eff}} \\ -\left[\mathcal{E}_{33}^{\text{eff}}\right]^{-1}\mathcal{E}_{31}^{\text{eff}} & \left[\mathcal{E}_{33}^{\text{eff}}\right]^{-1} & -\left[\mathcal{E}_{33}^{\text{eff}}\right]^{-1}\mathcal{E}_{32}^{\text{eff}} \\ \mathcal{E}_{21}^{\text{eff}} - \mathcal{E}_{23}^{\text{eff}}\left[\mathcal{E}_{33}^{\text{eff}}\right]^{-1}\mathcal{E}_{31}^{\text{eff}} & \mathcal{E}_{32}^{\text{eff}}\left[\mathcal{E}_{33}^{\text{eff}}\right]^{-1} & \mathcal{E}_{22}^{\text{eff}} - \mathcal{E}_{23}^{\text{eff}}\left[\mathcal{E}_{33}^{\text{eff}}\right]^{-1}\mathcal{E}_{32}^{\text{eff}} \end{bmatrix}. \tag{2.116}$$

First we consider the grating with arbitrary modulation of isotropic optical properties in y-axis direction $\varepsilon(y) = [n(y)]^2$. The effective medium exhibits a form uniaxial anisotropy described according to Eqs. (2.113-2.116) using the ordinary and extraordinary permittivity:

$$\varepsilon_o^{\text{eff}} = \left[n_o^{\text{eff}}\right]^2 = \varepsilon_{xx}^{\text{eff}} = \varepsilon_{zz}^{\text{eff}} = \frac{1}{\Lambda}\int_0^{\Lambda}\varepsilon(y)\mathrm{d}y, \qquad \frac{1}{\varepsilon_e^{\text{eff}}} = \frac{1}{\left[n_e^{\text{eff}}\right]^2} = \frac{1}{\varepsilon_{yy}^{\text{eff}}} = \frac{1}{\Lambda}\int_0^{\Lambda}\frac{\mathrm{d}y}{\varepsilon(y)}. \tag{2.117}$$

The procedure can be applied for arbitrary profile of the permittivity tensor in the y-direction grating. Table 2.1 summarizes ordinary and extraordinary effective

Table 2.1: Effective medium approximation for various permittivity profiles.

Permittivity profile	$\varepsilon_o^{\text{eff}}$ – ordinary ($\varepsilon_{xx}^{\text{eff}} = \varepsilon_{zz}^{\text{eff}}$)	$\varepsilon_e^{\text{eff}}$ – extraordinary ($\varepsilon_{yy}^{\text{eff}}$)
Lamellar 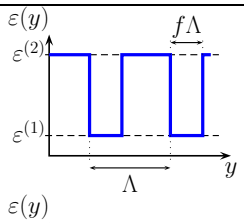	$\varepsilon_o^{\text{eff}} = f\varepsilon^{(1)} + (1-f)\varepsilon^{(2)}$	$\dfrac{1}{\varepsilon_e^{\text{eff}}} = \dfrac{f}{\varepsilon^{(1)}} + \dfrac{1-f}{\varepsilon^{(2)}}$
Sinusoidal 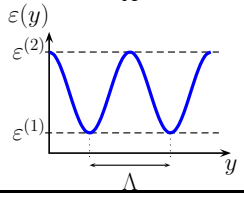	$\varepsilon_o^{\text{eff}} = \dfrac{\varepsilon^{(1)} + \varepsilon^{(2)}}{2}$	$\varepsilon_e^{\text{eff}} = \sqrt{\varepsilon^{(1)}\varepsilon^{(2)}}$

permittivity for lamellar and sinusoidal modulations of grating optical properties. The ordinary effective permittivity of the lamellar grating is obtained as weighted sum of both permittivity, while in the case the extraordinary permittivity (perpendicular to lamellas) we have to sum the inverse permittivities of lamellas. Those formulas have been applied to explain the form birefringence [76, 88, 91–94].

The second line of the table shows the effective parameters of the grating with sinusoidal modulation of optical properties

$$\varepsilon(y) = \frac{\varepsilon^{(1)} + \varepsilon^{(2)}}{2} + \frac{\varepsilon^{(2)} - \varepsilon^{(1)}}{2} \sin\frac{2\pi\, y}{\Lambda}. \tag{2.118}$$

The effective permittivity $\varepsilon_e^{\text{eff}}$ was obtained with help of the definite integral

$$\int_0^{2\pi} \frac{\mathrm{d}x}{a + b\,\sin x} = \frac{2\,\pi}{\sqrt{a^2 - b^2}}. \tag{2.119}$$

The effective medium is anisotropic with the geometric mean of the minimal and maximal permittivity along the modulation gradient (in agreement with [61]), while the permittivities along x and z-direction are obtained as the arithmetic means.

Case without mode conversion

Here we consider the case, for which the diagonal permitivities can differ, describing a biaxial crystal in special non-mode conversion geometry (symmetry axes are parallel to the coordinate ones). This case is described by the diagonal permittivity tensor:

$$\hat{\varepsilon}(y) = \begin{bmatrix} \varepsilon_{xx}(y) & 0 & 0 \\ 0 & \varepsilon_{yy}(y) & 0 \\ 0 & 0 & \varepsilon_{zz}(y) \end{bmatrix}, \tag{2.120}$$

where

$$\varepsilon_{ii}(y) = \frac{\varepsilon_{ii}^{(1)} + \varepsilon_{ii}^{(2)}}{2} + \frac{\varepsilon_{ii}^{(2)} - \varepsilon_{ii}^{(1)}}{2} \sin\frac{2\pi\, y}{\Lambda} \tag{2.121}$$

Note that an isotropic medium is a special case for $\varepsilon_{xx}(y) = \varepsilon_{yy}(y) = \varepsilon_{zz}(y)$. Using the procedure described in previous section, the effective properties of the grating are obtained in the form:

$$\hat{\varepsilon}^{\text{eff}} = \begin{bmatrix} \dfrac{\varepsilon_{xx}^{(1)} + \varepsilon_{xx}^{(2)}}{2} & 0 & 0 \\ 0 & \sqrt{\varepsilon_{yy}^{(1)}\varepsilon_{yy}^{(2)}} & 0 \\ 0 & 0 & \dfrac{\varepsilon_{zz}^{(1)} + \varepsilon_{zz}^{(2)}}{2} \end{bmatrix} \tag{2.122}$$

Mode conversion case – magneto-optical configuration

In special configurations like samples with magnonic waves [60,95], there is combination of polar and longitudinal mode and the modulation is in those elements only.

$$\hat{\varepsilon}(y) = \begin{bmatrix} \varepsilon_{xx} & \varepsilon_{xy}(y) & -\varepsilon_{zx}(y) \\ -\varepsilon_{xy}(y) & \varepsilon_{yy} & 0 \\ \varepsilon_{zx}(y) & 0 & \varepsilon_{zz}(y) \end{bmatrix}, \tag{2.123}$$

where

$$\varepsilon_{xy}(y) = \frac{\varepsilon_{xy}^{(1)} + \varepsilon_{xy}^{(2)}}{2} + \frac{\varepsilon_{xy}^{(2)} - \varepsilon_{xy}^{(1)}}{2} \sin\frac{2\pi\, y}{\Lambda}, \tag{2.124}$$

$$\varepsilon_{zx}(y) = \frac{\varepsilon_{zx}^{(1)} + \varepsilon_{zx}^{(2)}}{2} + \frac{\varepsilon_{zx}^{(2)} - \varepsilon_{zx}^{(1)}}{2} \cos\frac{2\pi\, y}{\Lambda} \tag{2.125}$$

The effective permittivity tensor is obtained in the form

$$\hat{\varepsilon}^{\text{eff}} = \begin{bmatrix} \varepsilon_{xx} + \dfrac{\left(\varepsilon_{xy}^{(2)} - \varepsilon_{xy}^{(1)}\right)^2}{8\varepsilon_{yy}} & \dfrac{\varepsilon_{xy}^{(1)} + \varepsilon_{xy}^{(2)}}{2} & -\dfrac{\varepsilon_{xz}^{(1)} + \varepsilon_{xz}^{(2)}}{2} \\ -\dfrac{\varepsilon_{xy}^{(1)} + \varepsilon_{xy}^{(2)}}{2} & \varepsilon_{yy} & 0 \\ \dfrac{\varepsilon_{xz}^{(1)} + \varepsilon_{xz}^{(2)}}{2} & 0 & \varepsilon_{zz} \end{bmatrix} \tag{2.126}$$

General case

The most general case is where there is modulation between arbitrary anisotropic materials. The permittivity tensor is

$$\hat{\varepsilon}(y) = \begin{bmatrix} \varepsilon_{xx}(y) & \varepsilon_{xy}(y) & \varepsilon_{xz}(y) \\ \varepsilon_{yx}(y) & \varepsilon_{yy}(y) & \varepsilon_{yz}(y) \\ \varepsilon_{zx}(y) & \varepsilon_{zy}(y) & \varepsilon_{zz}(y) \end{bmatrix}, \tag{2.127}$$

where

$$\varepsilon_{ij}(y) = \frac{\varepsilon_{ij}^{(1)} + \varepsilon_{ij}^{(2)}}{2} + \frac{\varepsilon_{ij}^{(2)} - \varepsilon_{ij}^{(1)}}{2} \sin \frac{2\pi\, y}{\Lambda} \tag{2.128}$$

The effective permittivity tensor is obtained in the form

$$\hat{\varepsilon}^{\text{eff}} = \begin{bmatrix} \dfrac{\varepsilon_{xx}^{(1)}+\varepsilon_{xx}^{(2)}}{2} + \dfrac{\varepsilon_{xy}^{(2)}-\varepsilon_{xy}^{(1)}}{2}\dfrac{\varepsilon_{yx}^{(2)}-\varepsilon_{yx}^{(1)}}{2}\dfrac{B}{A^2} & \dfrac{\varepsilon_{xy}^{(1)}+\varepsilon_{xy}^{(2)}}{2} + \dfrac{\varepsilon_{xy}^{(2)}-\varepsilon_{xy}^{(1)}}{2}\dfrac{B}{A} & \dfrac{\varepsilon_{xz}^{(1)}+\varepsilon_{xz}^{(2)}}{2} + \dfrac{\varepsilon_{xy}^{(2)}-\varepsilon_{xy}^{(1)}}{2}\dfrac{\varepsilon_{yz}^{(2)}-\varepsilon_{yz}^{(1)}}{2}\dfrac{B}{A^2} \\ \dfrac{\varepsilon_{yx}^{(1)}+\varepsilon_{yx}^{(2)}}{2} + \dfrac{\varepsilon_{yx}^{(2)}-\varepsilon_{yx}^{(1)}}{2}\dfrac{B}{A} & \sqrt{\varepsilon_{yy}^{(1)}\varepsilon_{yy}^{(2)}} & \dfrac{\varepsilon_{yz}^{(1)}+\varepsilon_{yz}^{(2)}}{2} + \dfrac{\varepsilon_{yz}^{(2)}-\varepsilon_{yz}^{(1)}}{2}\dfrac{B}{A} \\ \dfrac{\varepsilon_{zx}^{(1)}+\varepsilon_{zx}^{(2)}}{2} + \dfrac{\varepsilon_{zy}^{(2)}-\varepsilon_{zy}^{(1)}}{2}\dfrac{\varepsilon_{yx}^{(2)}-\varepsilon_{yx}^{(1)}}{2}\dfrac{B}{A^2} & \dfrac{\varepsilon_{zy}^{(1)}+\varepsilon_{zy}^{(2)}}{2} + \dfrac{\varepsilon_{zy}^{(2)}-\varepsilon_{zy}^{(1)}}{2}\dfrac{B}{A} & \dfrac{\varepsilon_{zz}^{(1)}+\varepsilon_{zz}^{(2)}}{2} + \dfrac{\varepsilon_{zy}^{(2)}-\varepsilon_{zy}^{(1)}}{2}\dfrac{\varepsilon_{yz}^{(2)}-\varepsilon_{yz}^{(1)}}{2}\dfrac{B}{A^2} \end{bmatrix} \tag{2.129}$$

where $A = \left(\varepsilon_{yy}^{(2)} - \varepsilon_{yy}^{(1)}\right)/2$ and $B = \sqrt{\varepsilon_{yy}^{(1)}\varepsilon_{yy}^{(2)}} - \left(\varepsilon_{yy}^{(1)} + \varepsilon_{yy}^{(2)}\right)/2$

Chapter 3

Magneto-optical characterization of binary III-V semiconductors

3.1 Energy scale

Before describing the physical properties of semiconductors, it is useful to establish a bigger picture, to relate the energy and frequency scale to other quantities and the physical properties of both the measurement techniques and the semiconductor samples.

We describe light as electromagnetic wave with its certain frequency f (Hz), angular frequency ω (rad/s), wavelength λ (m), wavenumber $\lambda^{-1}(\mathrm{cm}^{-1})$, energy E (eV) or equivalent temperature T (K). All these quantities give us the same information about the electromagnetic wave, but each of them has its established area of use, based on historical reasons or plain simplicity of its use (i.e. not too big, not too small numbers).

The angular frequency ω is a 2 π multiplication of the frequency f, as $\omega = 2\pi f$. The wavelength λ, is the speed of electromagnetic wave (speed of light, $c = 299792458\ \mathrm{ms}^{-1}$) divided by frequency, $\lambda = \frac{c}{f}$.

The energy of the electromagnetic wave is the Planck constant $h = 6.62607 \cdot 10^{-34}$ Js, or in more used units $h = 4.135667662 \cdot 10^{-15}$ eVs ($1\mathrm{eV} = 1.602 \cdot 10^{-19}$ J), times frequency $E = hf$.

Using another important physical constant, the Boltzman constant $k_B = 1.38064852 \cdot 10^{-23}\ \mathrm{J} \cdot \mathrm{K}^{-1}$, we can express the equivalent temperature $T = \frac{E}{k_B}$. Lastly, the inverse of the wavelength expressed in cm, called the wavenumber λ^{-1} is a frequently used unit in spectroscopy.

The studied range covers light from near ultraviolet (several eV, thousand terahertz) to gigahertz frequencies. We characterize the samples using three spectroscopic

techniques, Terahertz time-domain spectroscopy (THz-TDS), Fourier transform infrared spectroscopy (FTIR) and Mueller matrix Ellipsometry, and one electric technique - Van der Pauw's measurement. Table 3.1 summarizes the energy range with the corresponding methods and our instruments.

Table 3.1: Energy range, methods and unit conversion

Method	Wavelength	Wavenumber	Energy	Temperature	Frequency
	μm	cm^{-1}	eV	K	Hz
Ellipsometry	0.193	$5.18 \cdot 10^4$	6.42	$7.45 \cdot 10^4$	$1.55 \cdot 10^{15}$
	1.7	$0.59 \cdot 10^4$	0.73	$0.85 \cdot 10^4$	$0.18 \cdot 10^{15}$
FTIR	1.33	7500	0.93	$1.08 \cdot 10^4$	$2.25 \cdot 10^{14}$
	200	50	0.0062	71.948	$1.5 \cdot 10^{12}$
THz-TDS	100	100	0.0124	143.9	$3 \cdot 10^{12}$
	5000	2	$2.48 \cdot 10^{-4}$	2.88	$0.06 \cdot 10^{12}$

As it is noticeable from the Table 3.1, it is appropriate to use different units for each method for simplicity and ease of use. For Ellipsometry, the used units are nanometers and electronvolts. For FTIR the parameter of choice is wavenumber, which is also used in Terahertz domain. Also, as the name suggests, Terahertz (1THz = 10^{12} Hz) is frequently used. To ease orientation between the units, Table 3.2 provides a tool for a quick conversion between wavenumbers used in the Terahertz and far-infrared domain and other units.

3.2 Physical properties

The physical properties in the studied range are governed by three main processes [96], band absorptions, lattice vibrations, and free carriers absorptions. The main interest of this work lies in the properties of free carriers. The lattice vibrations must be included due to their effects in the studied range. The band absorptions, i.e. optical transitions from valence band to the conduction band are modeled with an indirect method (b-spline) and study in their energy range (near IR-vis-UV) is complementary to the main work.

Table 3.2: Lookup table for conversion of wavenumbers to different units

Wavenumber cm^{-1}	Wavelength μm	Frequency THz	Energy eV
10	1000	0.3	0.00124
20	500	0.6	0.00248
30	333	0.9	0.00372
40	250	1.2	0.00496
50	200	1.5	0.00620
60	167	1.8	0.00744
70	143	2.1	0.00868
80	125	2.4	0.00992
90	111	2.7	0.01120
100	100	3	0.0124
200	50.0	6	0.0248
300	33.0	9	0.0372
400	25.0	12	0.0496
500	20.0	15	0.0620
600	16.7	18	0.0744
700	14.3	21	0.0868
800	12.5	24	0.0992
900	11.1	27	0.1120
1000	10.00	30	0.124
2000	5.00	60	0.248
3000	3.33	90	0.372
4000	2.50	120	0.496
5000	2.00	150	0.620
6000	1.67	180	0.744
7000	1.43	210	0.868
8000	1.25	240	0.992
9000	1.11	270	1.120
10000	1.00	300	1.240

This section deals with the derivation of permittivity tensor $\hat{\varepsilon}$ from the Drude-Lorentz model and its relation to other quantities - conductivity, mobility, Hall coefficient.

3.2.1 Drude-Lorentz model in magnetic field

The derivation of both permittivity $\hat{\varepsilon}$ and conductivity $\hat{\sigma}$ stems from the motion equation of free or bound charge carriers in electric and magnetic fields; for electrons it is

$$m^* \frac{d^2\mathbf{r}}{dt^2} + m^*\omega_0^2\mathbf{r} + m^*\gamma\frac{d\mathbf{r}}{dt} + e\left(\frac{d\mathbf{r}}{dt} \times \mathbf{B}\right) = -e\mathbf{E} \ , \tag{3.1}$$

where m^* is the effective mass of charge carrier, $\mathbf{r}$ is its the position, ω_0 is the natural resonant frequency of a bound oscillation, γ is the damping constant (the inverse of a scattering time), e is the elementary charge, $\mathbf{B}$ is the magnetic flux density of the external field and $\mathbf{E}$ is the electric field intensity of the electromagnetic wave. Assuming the magnetic field in the z direction and $\mathbf{E} = \mathbf{E_0}\exp(-i\omega t)$, we look for a solution in the form $\mathbf{r} = \mathbf{r_0}\exp(-i\omega t)$. Separating the coordinate components we obtain

$$-m^*\omega^2 x_0 - im^*\gamma\omega x_0 + m^*\omega_0^2 x_0 - i\omega y_0 B_z = -eE_{0x} \ , \tag{3.2a}$$

$$-m^*\omega^2 y_0 - im^*\gamma\omega y_0 + m^*\omega_0^2 y_0 + i\omega x_0 B_z = -eE_{0y} \ , \tag{3.2b}$$

$$-m^*\omega^2 z_0 - im^*\gamma\omega z_0 + m^*\omega_0^2 z_0 = -eE_{0z} \ . \tag{3.2c}$$

Here we can define an important parameter, the cyclotron frequency

$$\omega_c = \frac{eB}{m^*}. \tag{3.3}$$

Substituting Eq. (3.2a) into Eq. (3.2b) and vice versa, and using the cyclotron frequency (3.3) we obtain

$$x_0 = \frac{e}{m^*}\frac{-(\omega_0^2 - \omega^2 - i\gamma\omega)E_{0x} - i\omega_c\omega E_{0y}}{(\omega_0^2 - \omega^2 - i\gamma\omega)^2 - \omega_c^2\omega^2} \ , \tag{3.4a}$$

$$y_0 = \frac{e}{m^*}\frac{-(\omega_0^2 - \omega^2 - i\gamma\omega)E_{0y} + i\omega_c\omega E_{0x}}{(\omega_0^2 - \omega^2 - i\gamma\omega)^2 - \omega_c^2\omega^2} \ , \tag{3.4b}$$

$$z_0 = \frac{e}{m^*}\frac{-E_{0z}}{\omega_0^2 - \omega^2 - i\gamma_0\omega} \ . \tag{3.4c}$$

The electrical polarization is defined as $\mathbf{P} = N\mathbf{p} = -eN\mathbf{r} = \varepsilon_0\hat{\chi}\mathbf{E}$, where $\hat{\chi}$ is the susceptibility tensor and ε_0 is the vacuum permittivity. The permittivity components are

$$\varepsilon_{ij} = \delta_{ij} + \chi_{ij} = \delta_{ij} - \frac{Ne}{\varepsilon_0}\frac{\partial r_{0i}}{\partial E_j} \ , \tag{3.5}$$

where $i, j = x, y, z,\ r_0 = (x_0, y_0, z_0)$, which with the substitution of the plasma frequency

$$\omega_p = \left(\frac{Ne^2}{\varepsilon_0 m^*}\right)^{\frac{1}{2}} \tag{3.6}$$

yields the Lorentz term (from bound oscillations) of the permittivity. The vacuum contribution, δ_{ij} in Eq. (3.5) is omitted. In later equations this term is moved to the constant background permittivity. The Lorentz term is then

$$\varepsilon_{L,xx} = \varepsilon_{L,yy} = \frac{\omega_p^2(\omega_0^2 - \omega^2 - i\gamma\omega)}{(\omega_0^2 - \omega^2 - i\gamma\omega)^2 - \omega_c^2\omega^2} \ , \tag{3.7a}$$

$$\varepsilon_{L,xy} = -\varepsilon_{L,yx} = -i\frac{\omega_p^2\omega_c\omega}{(\omega_0^2 - \omega^2 - i\gamma\omega)^2 - \omega_c^2\omega^2} \ , \tag{3.7b}$$

$$\varepsilon_{L,zz} = \frac{\omega_p^2}{(\omega_0^2 - \omega^2 - i\gamma\omega)} \ . \tag{3.7c}$$

The Drude term is easily obtainable by setting the bound oscillation $\omega_0 = 0$, finalizing the tensor of permittivity from free carriers (omitting the vacuum contribution) in the form of

$$\varepsilon_{D,xx} = \varepsilon_{D,yy} = -\frac{\omega_p^2(\omega^2 + i\gamma_p\omega)}{(\omega^2 + i\gamma_p\omega)^2 - \omega_c^2\omega^2} \ , \tag{3.8a}$$

$$\varepsilon_{D,xy} = -\varepsilon_{D,yx} = -i\frac{\omega_p^2\omega_c\omega}{(\omega^2 + i\gamma_p\omega)^2 - \omega_c^2\omega^2} \ , \tag{3.8b}$$

$$\varepsilon_{D,zz} = -\frac{\omega_p^2}{\omega^2 + i\gamma_p\omega} \ . \tag{3.8c}$$

3.2.2 Total permittivity

The total permittivity of semiconductor can be expressed as the sum of three terms, constant (background) permittivity $\hat{\varepsilon}_\infty$, Drude term $\hat{\varepsilon}_D$ and Lorentz term $\hat{\varepsilon}_L$, as

$$\hat{\varepsilon}_r = \hat{\varepsilon}_\infty + \hat{\varepsilon}_D + \hat{\varepsilon}_L \ . \tag{3.9}$$

The background permittivity comes from the interband absorptions in higher energies. The Lorentz term comes from the lattice vibration - phonons. Although the

derivation shows a magnetic field dependence, it is rarely the case. The carriers in the lattice vibration are the atoms themselves, which means their effective mass is several orders greater than that of free electrons and subsequently their cyclotron frequency is negligible. Experiments confirm this assumption, for example there was no measured change in phonon in GaAs at external field 8 T [27]. Therefore the contribution of Lorentz term is deemed isotropic, as the zz-component in Eq. (3.7), with a slight change. For the Lorentz term, we will denote the natural resonant frequency $\omega_0 = \omega_L$ and express the plasma frequency squared as $\omega_p^2 = A_L\omega_L^2$, where A_L is the amplitude of the oscillator. The damping is denoted γ_L, to distinguish the terms. Thus,

$$\varepsilon_L = \frac{A_L\omega_L^2}{(\omega_L^2 - \omega^2 - i\gamma_L\omega)} \ . \tag{3.10}$$

The Drude term is the most crucial for this work. It describes the behavior of charged carriers - plasma. The carriers can be either electrons or holes, their difference is the effective mass, caused by the shape of the band structure [97] and the sign of the electric charge. The derivation has been done for electrons, with minus already included. The opposite charge for holes is needed for calculations with magneto-optics only. The III-V semiconductors studied all have direct symmetrical band gap - all effective masses are isotropic, unlike the case for i.e. Germanium or Silicon. Without any applied external magnetic field, the Drude terms is isotropic (with the damping denoted γ_p), as

$$\varepsilon_D = -\frac{\omega_p^2}{\omega^2 + i\gamma_p\omega}. \tag{3.11}$$

While the derivation in Section 3.2.1 was done assuming the external magnetic field (flux density) in the z-direction, the derivation holds for all orientations of the magnetic field aligned with the coordinate axes. This descriptions distinguishes three orientations, polar (z), longitudinal (y) and transversal (x), shown in Figure 2.2. The permittivity tensors changes accordingly. As with the derivation for polar magnetic field, we have three components, one diagonal unaffected by the magnetic field (the one in the direction of the magnetic field), two diagonal, perpendicular to the magnetic field, and two of-diagonal elements, with opposite elements. The resulting

tensors are as follows

$$\underbrace{\begin{bmatrix} \varepsilon_{xx} & 0 & 0 \\ 0 & \varepsilon_{yy} & 0 \\ 0 & 0 & \varepsilon_{zz} \end{bmatrix}}_{\text{Isotropic}}, \quad \underbrace{\begin{bmatrix} \varepsilon_{xx} & \varepsilon_{xy} & 0 \\ \varepsilon_{yx} & \varepsilon_{yy} & 0 \\ 0 & 0 & \varepsilon_{zz} \end{bmatrix}}_{\text{Polar}}, \quad \underbrace{\begin{bmatrix} \varepsilon_{xx} & 0 & \varepsilon_{xz} \\ 0 & \varepsilon_{yy} & 0 \\ \varepsilon_{zx} & 0 & \varepsilon_{zz} \end{bmatrix}}_{\text{Longitudinal}}, \quad \underbrace{\begin{bmatrix} \varepsilon_{xx} & 0 & 0 \\ 0 & \varepsilon_{yy} & \varepsilon_{yz} \\ 0 & \varepsilon_{zy} & \varepsilon_{zz} \end{bmatrix}}_{\text{Transversal}}. \tag{3.12}$$

The components and their relation are listed in Table 3.3.

Table 3.3: Tensor components of the Drude term

Component	Expression	Polar	Longitudinal	Transversal
Parallel	$-\frac{\omega_p^2}{\omega^2+i\gamma_p\omega}$	ε_{zz}	ε_{yy}	ε_{xx}
Perpendicular	$-\frac{\omega_p^2(\omega^2+i\gamma_p\omega)}{(\omega^2+i\gamma_p\omega)^2-\omega_c^2\omega^2}$	$\varepsilon_{xx,yy}$	$\varepsilon_{xx,zz}$	$\varepsilon_{yy,zz}$
Of-diagonal	$-i\frac{\omega_p^2\omega_c\omega}{(\omega^2+i\gamma_p\omega)^2-\omega_c^2\omega^2}$	$\varepsilon_{yx}=-\varepsilon_{xy}$	$\varepsilon_{xz}=-\varepsilon_{zx}$	$\varepsilon_{yz}=-\varepsilon_{zy}$

It is also worthwhile to analyze the limit of the permittivity functions when the frequency goes to zero (a DC limit). The Lorentz oscillator raises the constant (real) permittivity by the value of its amplitude A_L for frequencies below the oscillator frequency. This is also the origin of the background permittivity that we observe in the infrared range. The absorbtions in the visible light can all can be understood as bound oscillators, which in sum of their amplitudes create the background permittivity.

The Drude term around the plasma frequency behaves only lowers the real part of permittivity and increases absorbtions. It does however have a DC limit, for real parts of both the classical Drude term and with the addition of the cyclotron frequency. This also follows from the origin of the Drude term - free carriers, which are the cause of conductivity, which must have a finite value in DC limit (more in Section 3.2.3). The limits of Drude terms for real parts (denoted by apostrophe) are

$$\lim_{\omega\to 0} \varepsilon'_{D,xx} = -\frac{\omega_p(\gamma_p^2-\omega_c^2)}{(\gamma_p^2+\omega_c^2)^2}\ , \tag{3.13a}$$

$$\lim_{\omega\to 0} \varepsilon'_{D,xy} = -\frac{-2\omega_p^2\omega_c\gamma_p}{(-\gamma^2-\omega_c^2)^2}\ , \tag{3.13b}$$

$$\lim_{\omega\to 0} \varepsilon'_{D,zz} = -\frac{\omega_p^2}{\gamma_p^2}\ . \tag{3.13c}$$

This DC limit can be observed in the Terahertz in metals as shown in [98, 99]. The influence of the cyclotron frequency becomes important in high mobility semiconductors, when $\omega_c^2 > \gamma_p^2$ and the negative DC limit changes into positive, turning off the plasmonic properties (more in Section 3.4)

3.2.3 Hall effect, conductivity, mobility

Similarly to permittivity, which corresponds to the position/displacement of the charged particle, a complex time-dependent conductivity tensor can be derived, which pertains to the velocity of the charged particle. The conductivity tensor for magnetic field in the polar (z) direction is then

$$\hat{\sigma} = \frac{\sigma_0}{(1-i\omega\tau)^2+\omega_c^2\tau^2}\begin{bmatrix} 1-i\omega\tau & -\omega_c\tau & 0 \\ \omega_c\tau & 1-i\omega\tau & 0 \\ 0 & 0 & \frac{(1-i\omega\tau)^2+\omega_c^2\tau^2}{1-i\omega\tau} \end{bmatrix}, \tag{3.14}$$

Which can also be calculated using the formula

$$\hat{\sigma} = -i\,\varepsilon_0\,\omega\,\hat{\varepsilon}. \tag{3.15}$$

The symmetry of both the permittivity and conductivity tensors in a magnetic field illustrates the likeness of the Hall effect and the magneto-optical effect. In the Hall effect, an applied voltage in one direction causes a drift of electrons and a charge build up in the direction perpendicular to the applied voltage and magnetic field. The charge buildup creates an electric field - the Hall voltage. The magneto-optical effect works similarly; the incident light sets the carriers in motion, while the magnetic field causes a precession of their movement perpendicular to the polarization and the magnetic field, causing a rotation of polarization. This process is illustrated in Figure 3.1.

The limit of Eq. (3.14) when $\omega \to 0$ is the DC magneto-conductivity tensor

$$\hat{\sigma}_{DC} = \sigma_0 \begin{bmatrix} \frac{1}{1+\omega_c^2\tau^2} & -\frac{\omega_c\tau}{1+\omega_c^2\tau^2} & 0 \\ \frac{\omega_c\tau}{1+\omega_c^2\tau^2} & \frac{1}{1+\omega_c^2\tau^2} & 0 \\ 0 & 0 & 1 \end{bmatrix}. \tag{3.16}$$

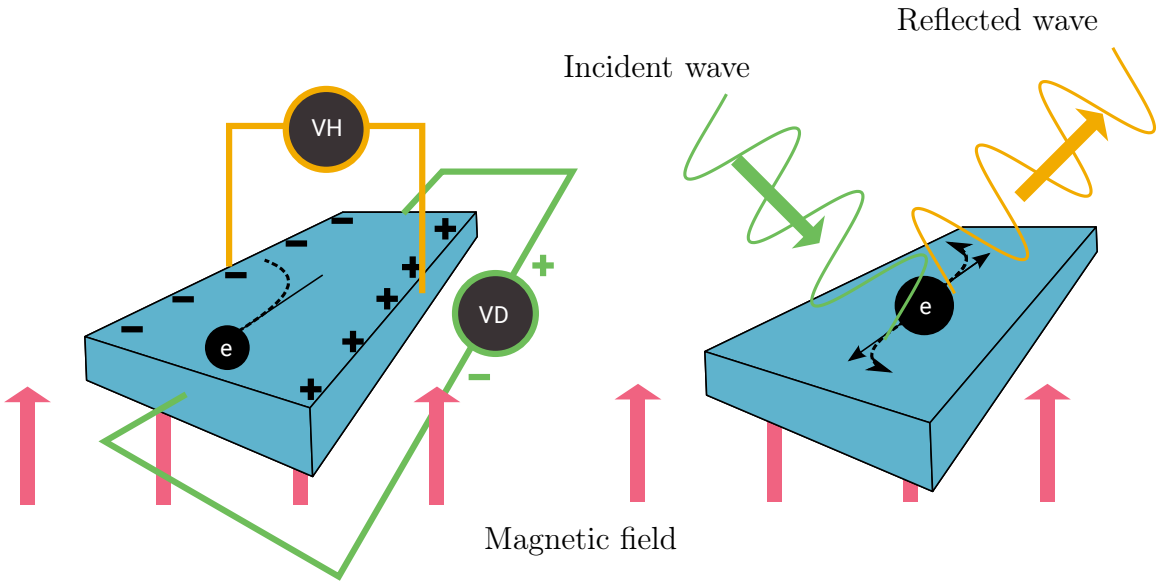

Figure 3.1: Illustration of electric (DC limit) Hall effect and Optical Hall effect

The semiconductor free carrier properties are defined by a set of parameters that are included in the permittivity/conductivity tensor: the carrier concentration N, the sign of the carrier charge e, the carrier effective mass m^*, and the carrier mobility $\mu(\mathrm{m}^2/\mathrm{Vs})$, defined as $\mu = e\tau/m^*$. The concentration $N(\mathrm{m}^{-3})$ is determined by the amount of doping for doped semiconductors, and it is a function of temperature for intrinsic semiconductors.

The optical measurements of reflectivity allows us to obtain only the plasma frequency and the scattering time, in addition to the constant term and parameters of the Lorentz oscillator, as per Eq. (3.9). Using the plasma frequency and scattering time one can calculate the DC conductivity as

$$\sigma_0 = \frac{Ne^2\tau}{m^*} = \varepsilon_0\,\omega_p^2\,\tau \ . \tag{3.17}$$

Without further information, one needs to rely on an estimate of the effective mass [100], or the ratio between the effective mass and concentration, to calculate other relevant parameters. From a measurement in a magnetic field, one can deduce the cyclotron frequency, use the Eq. (3.8) and a model of reflectivity from anisotropic layers to calculate the effective mass

$$m^* = \frac{eB}{\omega_c} \ , \tag{3.18}$$

and the concentration

$$N = \frac{\omega_p^2 \varepsilon_0 m^*}{e^2} = \frac{\omega_p^2}{\omega_c}\frac{\varepsilon_0 B}{e}. \tag{3.19}$$

Frequently used method for determining the semiconductor properties is through the measurement of the Hall effect, often by the Van der Pauw (VdP) method [101], requiring an ohmic contact with the sample. Using this method, and the knowledge of the sample thickness, one can obtain the Hall coefficient $R_H(\mathrm{m}^3/\mathrm{C})$ and the conductivity σ_0. For a single carrier system with electrons, the Hall coefficient is defined as

$$R_H = -\frac{1}{Ne} = -\frac{\mu}{\sigma_0} = -\frac{\sigma_{DC,xy}}{(\sigma_{DC,xx}^2 + \sigma_{DC,xy}^2)B_z}, \tag{3.20}$$

from which the concentration and the mobility can be calculated.

Knowing the relationship between the conductive and spectral properties allows one to crosscheck the quality of measurements or to draw conclusions about the behavior of one from the measurement of the other. This is demonstrated in Sec. 3.4.3, as a comparison of the semiconductor parameters obtained from the reflectivity fit and the parameters measured using the VdP method.

3.3 Experimental methods

3.3.1 Ellipsometry

Ellipsometry is an optical technique for characterization of material parameters and dimensions of structures by measuring the change of polarization state of light reflected or transmitted from the sample. The reflected/transmitted light is most often elliptically polarized, hence the name ellipsometry. Generally, multiple wavelengths are used, coining the term spectroscopic ellipsometry (SE). Ellipsometry is used in different wavelength ranges, but it is traditionally used in UV-visible-near infrared range. Typical ellipsometric system consist of several parts, as illustrated in Figure 3.2. The source (e.g. Xe lamp, or in our case Deuterium lamp and halogen bulb) shine light thorough the polarizer and compensator to/through the sample and the light again passes another compensator and polarizer (called analyzer) to the detector. The compensators can vary in number and principles, it can static waveplate, rotating waveplate, or modulator; their purpose is to control the polarization state of light.

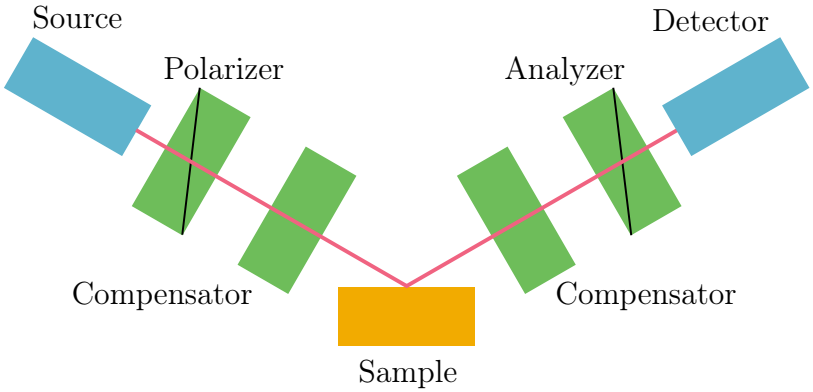

Figure 3.2: Components of an ellipsometric setup

The detected values are the complex ratios of reflective (transmissive) coefficients of different polarizations, measured through the modulation of the SE setup (photoelastic harmonics, rotating compensators). It the simplest case (isotropic sample), it is the ratio of p- and s- polarized light as

$$\frac{r_{pp}}{r_{ss}} = \tan\Psi e^{i\Delta}, \tag{3.21}$$

where $\tan\Psi$ is the amplitude of the ratio and Δ its phase. By measuring the ratio, rather than absolute values, SE eliminates the need for a reference beam. This make SE a robust and accurate method for material and structure characterization. For anisotropic or depolarizing sample, the simple Δ and Ψ measurement wouldn't capture all the information contained in the polarized light. This case needs either more ellipsometric ratios, with anisotropic coefficients,

$$\begin{aligned} \frac{r_{ps}}{r_{ss}} &= \tan\Psi_{ps} e^{i\Delta_{ps}} \\ \frac{r_{sp}}{r_{ss}} &= \tan\Psi_{sp} e^{i\Delta_{sp}}, \end{aligned} \tag{3.22}$$

which don't cover depolarization. A full Mueller matrix acquisition is suited for acquisition of data from anisotropic and/or depolarizing samples. For details on Muller matrix see Section 2.1.6. Spectroscopic Ellipsometry is an indirect method, the measured data must be compared to a model.

Our instrument is the Woolam RC2-Di, where the source is a combination of a deuterium lamp and halogen bulb, with the spectral range 0.74-6.42 eV (193-1700 nm). The system uses dual rotating compensators for full Mueller matrix measurement [102]. Typical data acquisition consists of calibration of the instrument and

measuring at several angles of incidence. The sample can be rotated and positioned automatically if needed. The proprietary software, Complete Ease allows for data analysis with a pre-built database with optical function of common materials and models for dielectric functions, such as Drude model, or B-Spline.

3.3.2 Fourier Transform Infrared Spectroscopy

Fourier Transform Infrared Spectroscopy (FTIR) is a technique that utilizes controlled interference of two beams of infrared light to extract spectral information about a measured sample. The control of the interference is done through the movement of mirrors, which changes the path lengths of the beams. Figure 3.3 shows a simplified schematic of a FTIR using a double pendulum [103]. Two corner cube retro-reflectors are mounted on a pendulum that swings about its axis. This changes the path difference and causes interference over the spectral range of the source. This is detected as change in intensity on the detector, in so called interferogram. The movement of the pendulum is measured using the interference of monochromatic He-Ne laser. Two data-sets are measured, one reference without the sample (in reflection this is with a gold mirror) and then with the sample. A Fourier transform (hence the name) is used on the detected interferograms, resulting in infrared spectra, as illustrated in Figure 3.4. The ratio of these spectra is the desired reflectivity or transmittance of the sample. FTIR is so widely used system that it doesn't really have a competition in the infrared spectroscopy [104]. Previously used systems employed grating monochromators, but this severely limited the available intensity.

Our FTIR system is the Bruker Vertex 70v, measuring in the far-infrared range 50-680 cm^{-1} and mid-infrared range 370-7500 cm^{-1}. All measurements were done in reflection, at the angle of incidence 11˙, which is approximated by a near-normal incidence. The sample chamber allowed for evacuation and mounting of polyethylene wire grid polarizer-analyzer tandem for polarization-sensitive measurement.

3.3.3 Terahertz Time-Domain Spectroscopy

Any significant use of the Terahertz range has long been limited by the lack of cheap and reliable sources, components and detectors. This changed with the advent of Terahertz time-domain spectroscopy (THz-TDS). This system uses a femtosecond

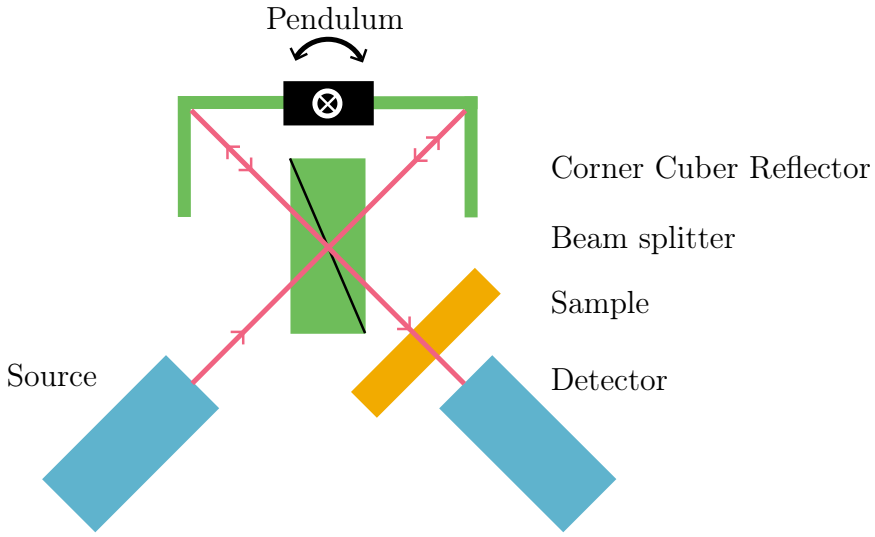

Figure 3.3: Component of FTIR setup

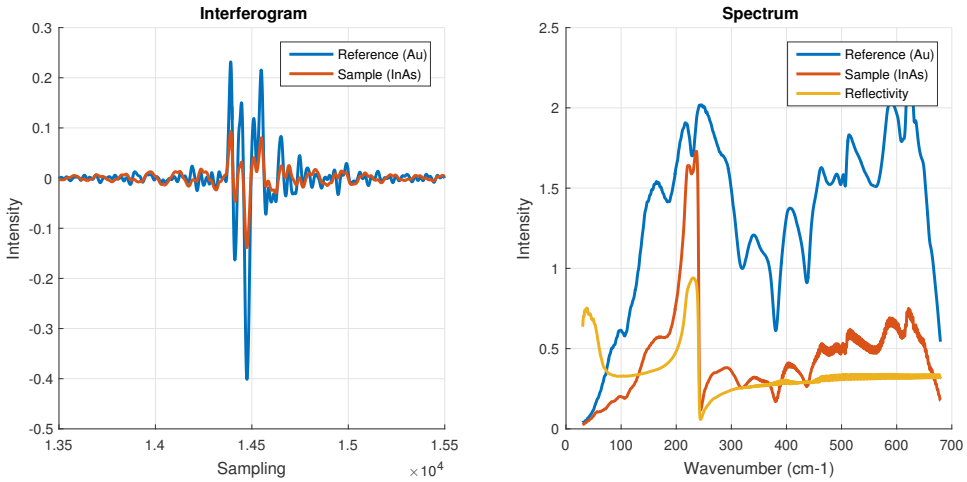

Figure 3.4: FTIR Interferogram and spectrum

pulse laser and some non-linear process, either optical rectification or ultrafast carrier scheme on a device called switch [105, 106]. Other means of generating terahertz light, such as solid-state lasers or sprintronic emmitters [107] are currently being researched. Figure 3.5 shows a schematic and illustrates the working principle of THz-TDS system. The femtosecond pulse excites a semiconductor source switch which generates a Terahertz pulse (Figure 3.6 left). The Terahertz pulse travels through an optical system and is reflected/transmitted from the sample. Then it travels to a detector switch. This switch is excited by a delayed femtosecond pulse and the detected

voltage is recorded. By varying the delay, the THz pulse is sampled, thus recording the full time dependent shape of the THz pulse signal. Using Fourier Transform, this signal is converted into both the amplitude and phase spectra (Figure 3.6 right). Similarly to FTIR, a reference measurement is needed. The ratio of sample and reference amplitude spectrum is the reflectivity/transmittance. The difference in phase is the resulting phase. Section 3.4 details the phase correction caused by misalignment of sample and reference. This provides us with a complex signal comparable to the model.

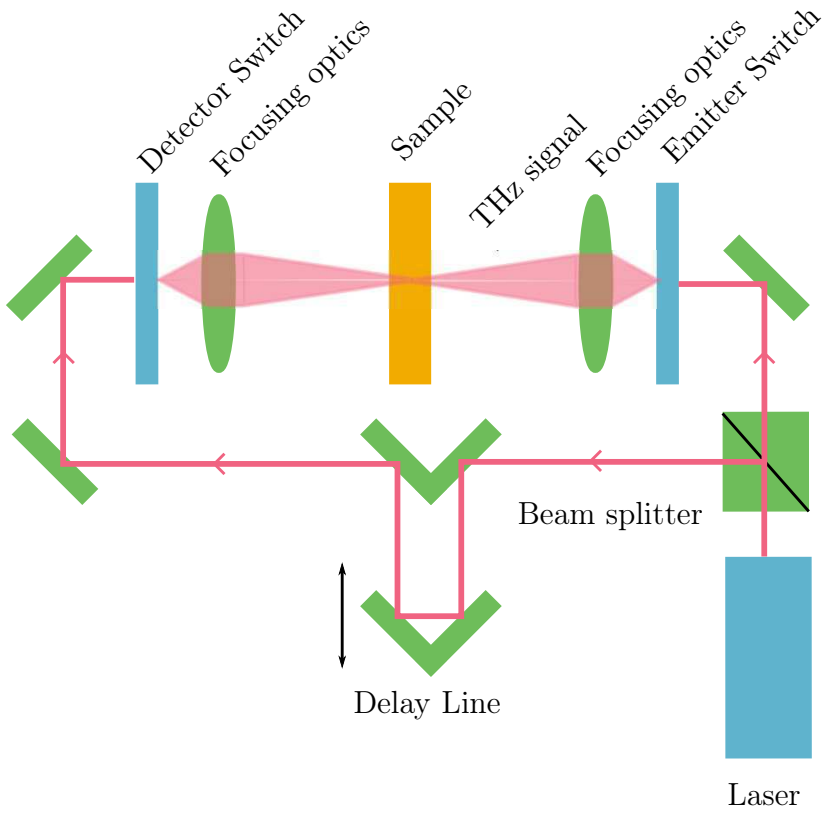

Figure 3.5: Schematic of the Terahertz time-domain setup. Curved mirrors are frequently used as focusing optics.

Our terahertz time-domain spectrometer is the TPS Spectra 3000 from TeraView Co., measuring in the THz range of 2-100 cm^{-1} (60 GHz-3 THz). This system uses femtosecond Er:doped fibre laser (Menlo) and semiconductor photoconductive switches.

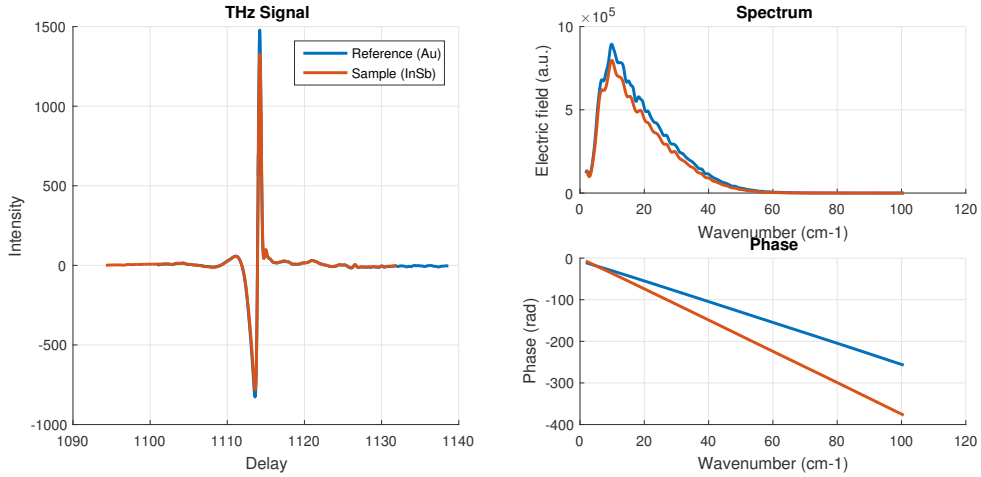

Figure 3.6: Detected Terahertz time-domain signal and phase an amplitude spectra.

3.4 Measurements and fits

3.4.1 Samples

We have measured seven representative samples of single-crystal III-V semiconductors. All were polished on one side.

The GaAs samples were 2", 0.35 mm thick wafers made by AXT, Inc. One n-doped with Si dopants, with the reported electron concentration of $(0.8-4)\times 10^{18}$ cm^{-3} and the mobility of $(1-2.5)\times 10^{3}$ cm^2/Vs. One p-doped (Zn), with the reported hole concentration of $(0.5-5)\times 10^{19}$ cm^{-3} and the mobility of $50-120$ cm^2/Vs.

The InP sample was 2", 0.35 mm thick wafer also from AXT. It is n-doped with Sulfur; the manufacturer reports values of $N=(0.8-8)\cdot 10^{18}$cm^{-3} and $\mu=(1-2.5)\cdot 10^{3}$cm^2/Vs.

Measured samples of InSb are n-doped (Te), p-doped (Ge) and undoped. All InSb samples were manufactured by MTI Corp as wafers of 2" diameter and a small 10×10 mm squares. The small samples were used for the Hall measurements by a 4-contact van der Pauw method. The thickness of the wafers was 0.5 mm for the n-doped and 0.45 mm for the undoped and p-doped. The small sample has thickness of 0.45 mm. The n-doped samples have the manufacturer's reported carrier concentration of $(0.19-0.50)\cdot 10^{18}$ cm^{-3} and the mobility of $(3.58-5.60)\cdot 10^{4}$ cm^2/Vs, both at 77 K. The p-doped samples have the following reported parameters: $N=0.5-5\cdot 10^{17}$ cm^{-3} and $\mu=4-8.4\cdot 10^{3}$ cm^2/Vs, again at 77 K.

The InAs undoped sample was provided by our colleagues at Université Lille 1.

3.4.2 Results - FTIR+THz-TDS

Figures 3.7 and 3.8 show the reflectivity spectra and the permittivity of the samples with the resulting parameters listed in Table 3.4.

The sharp minima in reflectivity between 150 and 300 cm^{-1} correspond to a crossing of the real part of the permittivity with the permittivity of vacuum due to the lattice vibrations. The fitted value of the Lorentz oscillator frequency is at the maximum of the imaginary part of the permittivity, corresponding to the transversal phonon [97]. The lattice vibrations presented here match the resonances reported by other authors (InP [108], GaAs [27], InSb [30]).

The InAs sample has two transparency windows in the infrared range, which were not included in the model. Therefore, the fitted range is smaller.

The plasma edge, a region where the real part of the permittivity crosses zero and becomes negative for lower frequencies due to the free carries is tied to the concentration and effective mass. Plasma edge is visible in the reflectivity spectra as sharp increase in reflectivity, For metals described by the Drude term, this would be where $\Re\{\varepsilon_D\} = 0$. Semiconductors however have a strong background permittivity, which from Eq. (3.9), places the crossover frequency (reduced plasma freq.) between positive and negative at $\omega = \omega_p/\sqrt{\varepsilon_\infty}$ and the reflectivity minimum at $\omega = \omega_p/\sqrt{\varepsilon_\infty - 1}$; assuming no damping and negligible effect of the phonon. Real cases show effect of the phonon and damping, i.e. the n-doped GaAs the reflectivity minimum would be at 545.2 cm^{-1} but the real one is at 573.6 cm^{-1}. The effect of damping is strongly present in the p-doped samples, where the short scattering time of the holes makes the reflectivity spectra much shallower. This effect is apparent in the GaAs samples, where there is significant difference between both the damping and the plasma frequency. It is less pronounced in undoped InSb and p-doped InSb due to similar plasma frequency.

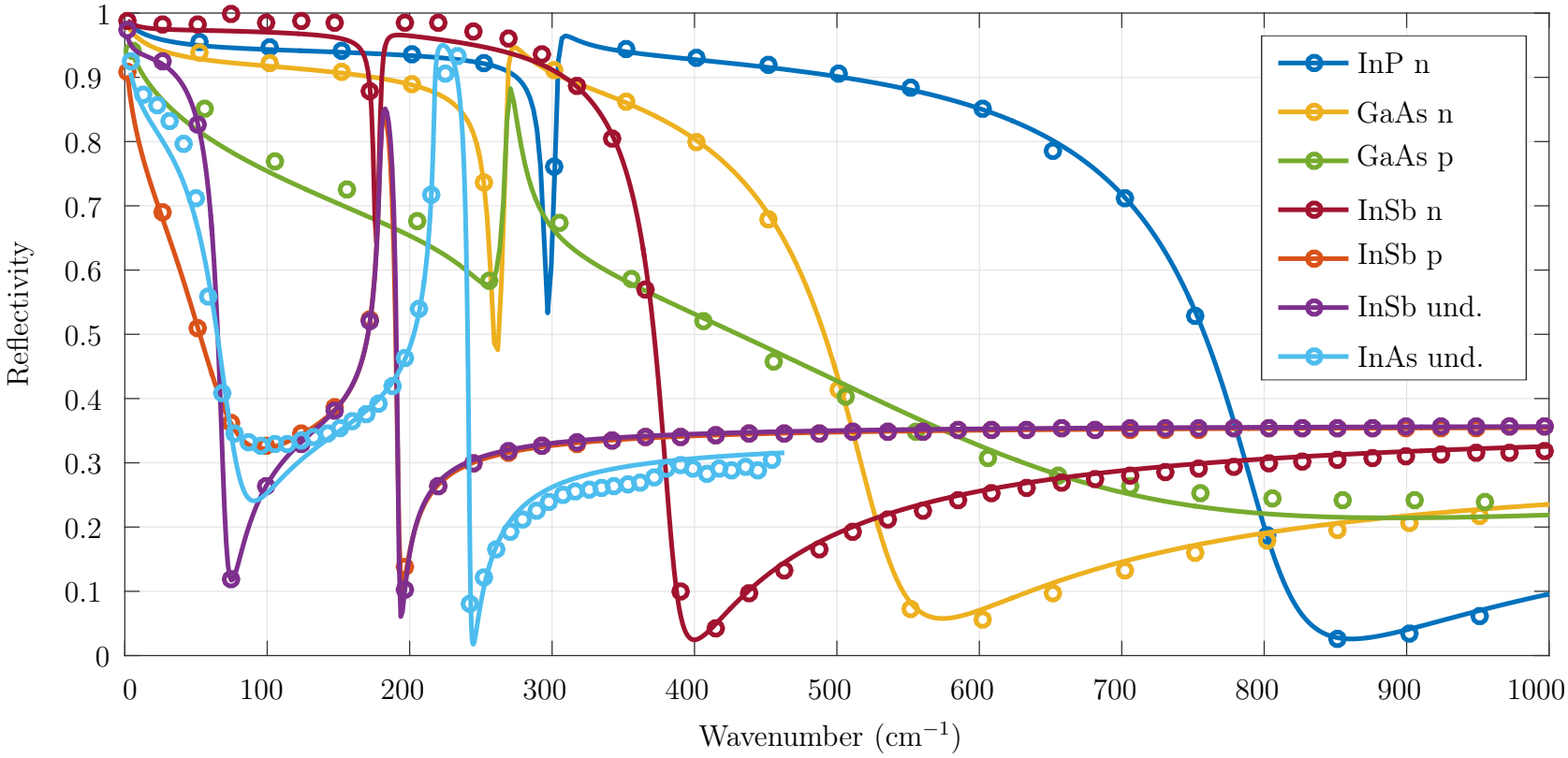

Figure 3.7: Measured and fitted reflectivity spectra of the samples in the terahertz and far-infrared range, overlapping ranges were averaged. Data (circles) reduced for clarity. Reflectivity is defined as the ratio between incident intensity and reflected intensity, see Eq. 2.67.

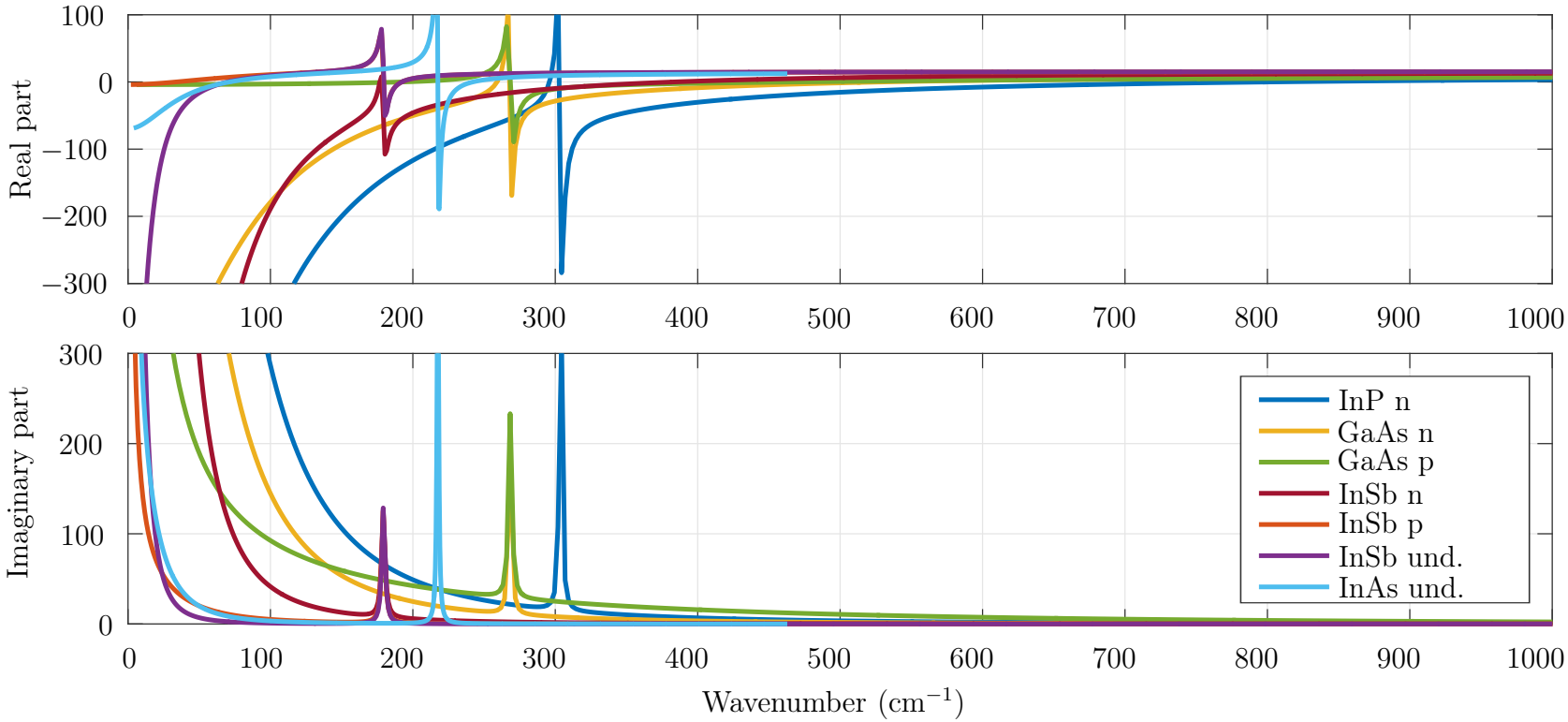

Figure 3.8: Real and imaginary part of the permittivity obtained from fitting of reflectivity data.

Table 3.4: Fitted parameters of GaAs, InP, InSb and InAs

	GaAs n-doped	GaAs p-doped	InP n-doped	InSb n-doped	InSb p-doped	InSb undoped	InAs undoped
ω_p (10^{14} rad/s)	3.33 ± 0.01	4.44 ± 0.02	4.70 ± 0.01	2.82 ± 0.01	0.63 ± 0.01	0.57 ± 0.01	0.61 ± 0.17
ω_p (cm^{-1})	1769.2 ± 1.9	2356.4 ± 9.1	2494.1 ± 1.8	1495.2 ± 1.83	332.6 ± 1.49	302.4 ± 0.33	325.3 ± 91.3534
τ_p (10^{-1} ps)	0.71 ± 0.01	0.09 ± 0.01	0.71 ± 0.01	2.65 ± 0.04	0.75 ± 0.01	5.16 ± 0.06	1.52 ± 0.06
ω_L (10^{13} rad/s)	5.06 ± 0.01	5.06 ± 0.01	5.73 ± 0.01	3.38 ± 0.01	3.38 ± 0.01	3.38 ± 0.01	4.10 ± 0.01
ω_L (cm^{-1})	268.4 ± 0.1	268.5 ± 0.2	303.9 ± 0.1	179.4 ± 0.13	179.4 ± 0.06	179.5 ± 0.06	217.67 ± 0.28
τ_L (ps)	2.79 ± 0.27	1.95 ± 0.29	3.01 ± 0.24	1.81 ± 0.13	1.90 ± 0.04	1.99 ± 0.04	3.63 ± 0.44
A_L	2.13 ± 0.03	2.15 ± 0.09	2.89 ± 0.04	2.02 ± 0.07	2.00 ± 0.01	2.02 ± 0.01	2.82 ± 0.05
ε_∞	11.58 ± 0.01	11.34 ± 0.02	10.01 ± 0.01	15.68 ± 0.03	15.74 ± 0.01	15.86 ± 0.01	13.57 ± 0.17
σ_0 (kS/m)	69.46 ± 0.54	16.54 ± 0.22	139.06 ± 0.77	186.35 ± 2.63	2.51 ± 0.04	14.83 ± 0.17	5.04 ± 0.24

3.4.3 Magnetooptics

When an external magnetic field is applied to the sample, the Drude term becomes anisotropic, as it has been shown in Section 3.2.1. This calls for modification of the measurement setup, we now need to have control over the polarization state of the incident and detected light. In the Terahertz time domain spectrometer this is done by a single polarizer, in the path of the near-normal incident beam, as shown in Figure 3.9. This configuration yields pure linear polarization. The reason for this configuration is its simplicity and limited space in the measuring cavity.

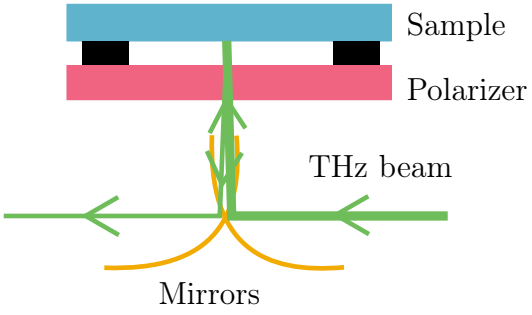

Figure 3.9: THz beam path for measuring the magneto-optical effect in InSb using a single polarizer.

For measurements using the FTIR spectrometer, we were able to employ two polarizers (i.e. polarizer and analyzer), with variable angles of rotation, as shown in Figure 3.10. We have chosen a fixed analyzer and rotating polarizer at the azimuthal angles 0°, 45°, 90°, 135° with respect to the azimuth of the fixed analyzer. The angle 0 is maximum transmission and the angle 90 means crossed polarizers. This setup has been described in Section 2.1.6 as (2.79). The detected quantities are summarized in Table 3.4.3.

Polarizer	Analyzer	Measured quantity
0°	0°	R_{ss}
45°	0°	$\sqrt{2}(R_{sp} + r_{sp}r_{ss}^* + r_{sp}^* r_{ss} + R_{ss})/2$
90°	0°	R_{sp}
135°	0°	$\sqrt{2}(R_{sp} - r_{sp}r_{ss}^* - r_{sp}^* r_{ss} + R_{ss})/2$

Table 3.5: FTIR configuration for magneto-optical measurements

First, measurements of InSb samples (n-doped, p-doped and undoped) were done and an interesting property emerged in the n-doped wafer. The carrier concentration

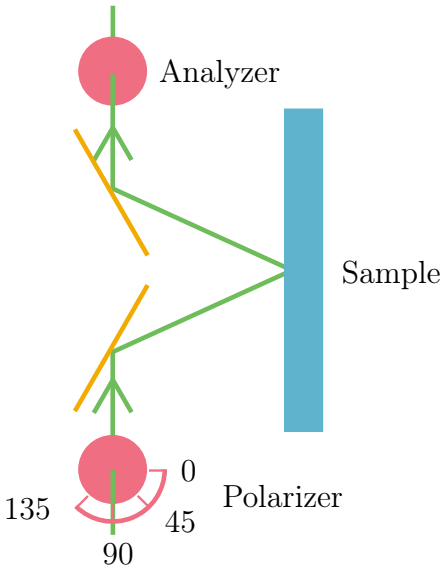

Figure 3.10: FTIR for measuring magneto-optical effect in InSb.

at the center of the wafer (N_1, shown originally in Figure 3.7 and Table 3.4) was smaller than at the edge (N_2). This is noticeable in the spectra as the different position of the plasma edge. The spectra are shown in detail in Figure 3.11.

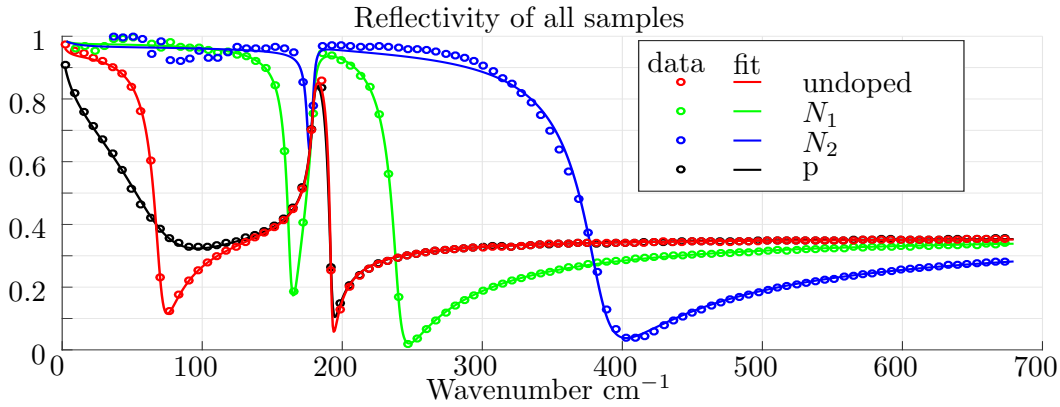

Figure 3.11: Reflectivity of all InSb samples, TDS and FTIR data joined together. The data in the small overlapping ranges were averaged, but overall there was a good match and continuity between the data.

When an external magnetic field is applied, the Drude term becomes anisotropic. The magnetic field was created by a small permanent magnet placed at the backside of the sample. Varying magnetic field was created by plastic spacers.

The undoped InSb sample's plasma edge is present in the terahertz domain, where

we are able to measure both the reflectivity and phase. The TDS reflectivity and phase of the undoped InSb in the variable magnetic field are shown in Figure 3.12. Reflection is modeled as a single interface between vacuum and the semiconductor with the permittivity ε_r, along with Jones matrices to apply the effects of the used polarizers to the model. The phase information in Figure 3.12 comes from three parts, $\varphi = \varphi_{\text{sample}} - \varphi_{\text{reference}} - \varphi_{\text{shift}}$. φ_{sample} is the phase angle of the complex reflection coefficient of the sample and φ_{shift} stems from the misalignment d of the sample and reference, as $\varphi_{\text{shift}} = 4d\pi \cos\alpha_i/\lambda$. The φ_{shift} is a fitting parameter in the data treatment (d is on the order of 1-100 μm) and is subtracted from the data for plotting. The measurements in different magnetic fields and without field were fitted together. The cyclotron frequency ω_c is 23.7 cm^{-1} for 0.43 T and the resulting effective mass of electrons in undoped InSb is $m_{eff} = (eB)/(\omega_c m_0) = 0.0169$, which in accordance to theory [109] is higher than the frequently used value of 0.015. The knowledge of both the cyclotron frequency and the plasma frequency allows also for the calculation of the carrier concentration N and the mobility $\mu = e\tau_p/m^*$ and is necessary for the correct theoretical prediction of the behavior of magneto-plasmonic devices.

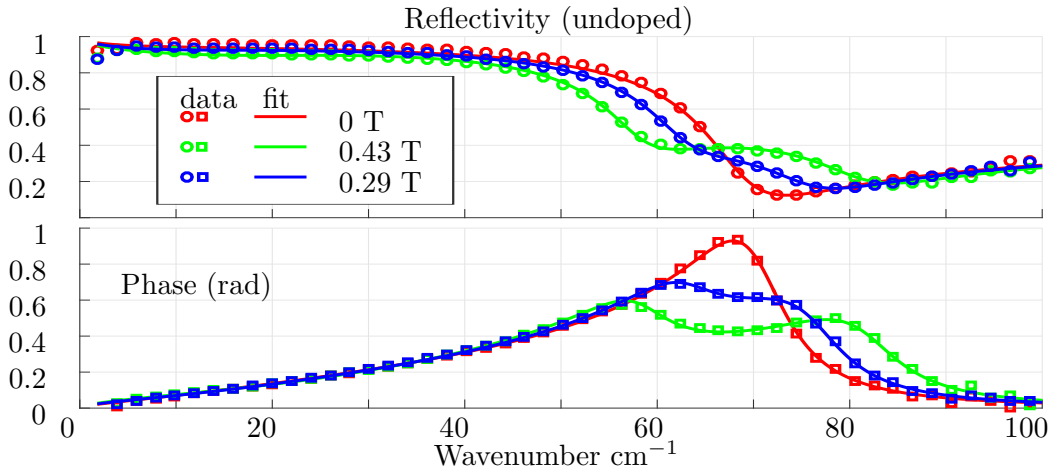

Figure 3.12: TDS polarized reflectivity and corrected phase of undoped InSb in variable magnetic field

The data from FTIR confirm the magneto-optical behavior of n-doped InSb, when the plasma frequency is pushed towards higher frequencies. Figure 3.13 shows the

reflectivity of two n-doped samples when the polarizer is at 45 degrees and the analyzer at zero. When the direction of the magnetic field is reversed, the rotation of the reflected polarization changes direction, causing a drop/increase in reflected amplitude. The same effect was obtained at the polarizer angle 135°, but for opposite signs of the magnetic field.

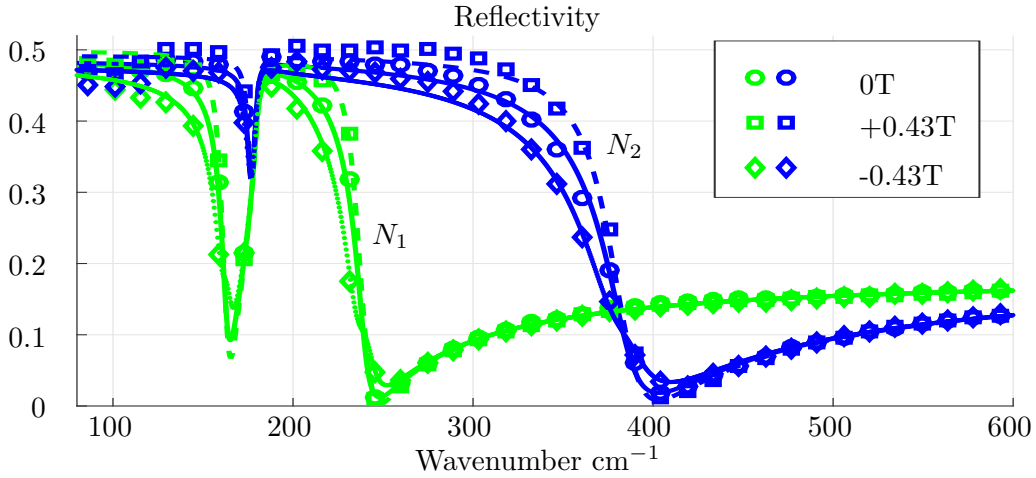

Figure 3.13: Reflectivity of two concentrations of n-doped InSb, polarizer at 45. Data (symbols) and fit (curves) are compared. The center curve (circles, solid line) is reflectivity without the magnetic field, the other two are obtained for different signs of the magnetic field.

The parameters describing all InSb samples are summarized in Table 3.6. The non-magnetic properties of the undoped InSb match those reported or used by [29, 110,111], but our measurements also allow for calculation of the correct effective mass and the carrier concentration. The samples have also been measured electrically by the van der Pauw (VDP) method [101], which is equivalent to $\omega \to 0$. The VDP data obtained are also listed in Table 3.6 and are reasonably close to those obtained by spectroscopic measurement. The differences in values obtained from electrical and spectroscopic measurement are due to different sensitivity of the measuring techniques to different mechanisms, and their systematic errors. Generally, the electric VdP measurement is used with lithographically etched pattern, but if there is a good ohmic contact (indicated by linearity of the measurement), it is possible to measure without it by placing the contact probes on to the sample. This measurement, used in our case, is prone to error due to possible misalignment of the contact probes. Moreover, the spectral characterization is sensitive only to the carriers with the highest plasma

frequency, whereas VdP includes the effect of both. These effects combined explain the differences in obtained values. The n-doped samples exhibit lower cyclotron frequency at the same magnetic field, meaning that the effective mass is higher, which is again in agreement with the theory [109].

Table 3.6: Parameters of InSb samples characterized at room temperature, undoped, n-doped with carrier concentrations N_1 and N_2 and p-doped. Subscript *spec.* means values obtained from spectroscopic magneto-optical measurement, subscript VPD means data obtained from Van der Pauw measurement.

Sample	$\omega_p/\sqrt{\epsilon_\infty}$ (cm^{-1})	τ_p 10^{-13} (s)	ω_L (cm^{-1})	τ_L 10^{-12} (s)	A_L	ω_c (cm^{-1})
und.	73.8 ± 0.1	5.53 ± 0.02	179.46 ± 0.05	2.00 ± 0.03	2.00 ± 0.01	23.76 ± 0.09
N_1	217.9 ± 0.2	4.00 ± 0.03	179.79 ± 0.03	1.66 ± 0.03	2.14 ± 0.01	11.25 ± 0.11
N_2	378.8 ± 0.3	2.01 ± 0.03	179.78 ± 0.03	1.74 ± 0.03	2.15 ± 0.01	13.99 ± 0.12
p	83.8 ± 0.3	0.75 ± 0.01	179.37 ± 0.05	1.89 ± 0.03	2.01 ± 0.01	
	ε_∞	m_{eff}	$N_{spec.}$ 10^{17} (cm^{-3})	$\mu_{spec.}$ 10^4 (cm/Vs)	N_{VDP} 10^{17} (cm^{-3})	μ_{VDP} 10^4(cm/Vs)
und.	15.68 ± 0.03	0.0169 ± 0.0001	0.17 ± 0.008	5.76 ± 0.03	0.20	6.66
N_1	15.58 ± 0.02	0.0357 ± 0.0003	2.93 ± 0.003	1.97 ± 0.02	2.37	4.12
N_2	15.68 ± 0.02	0.0287 ± 0.0002	7.20 ± 0.006	1.23 ± 0.02	-	-
p	15.84 ± 0.02	-	-	-	10.7	0.02

Figure 3.14 shows the obtained permittivity of all the samples using fitted parameters listed in Table 3.6. The presence of a cyclotron frequency changes the low frequency limit of the real part of the diagonal components $\varepsilon_{xx,yy}$, which can completely change sign, if $\omega_c^2 > \gamma_p^2$, as shown in Section 3.2.2. The magnetic field also increases absorptions (Landau level absorption) at ω_c, noticeable mainly in the undoped InSb sample. This effect is usually observed when $\omega_c > \omega_p$ and also causes changes in the effective mass, which is negligible in our case due to low magnetic field [112]. The off-diagonal elements exhibit a peak around ω_c and the quasistatic limit at low frequency (the classical Hall effect), while the imaginary part goes to infinity for low-frequencies [97].

Figure 3.15 shows the model of modulated permittivities with parameters obtained from this measurement. The change in the permittivity ε_{xx} is very sensitive to the magnetic field and it is possible to change sign for lower frequencies even using small field. The ε_{xy} components also rapidly change with the strength of the applied magnetic field and interestingly exhibit maximum for a certain magnetic field.

Using the permittivity tensors we can further obtain the normal incidence polar Kerr effect [87] which is a good metric to describe the magneto-optical behavior of materials. The polar magneto-optical Kerr effect is a change of the polarization ellipse azimuth and ellipticity upon reflection of linearly polarized light from a sample in a magnetic field perpendicular to the interface. Two eigenmodes having right-handed a left-handed circular polarizations propagate in this configuration (normal incidence). They propagate with the effective refractive indices $\nu_\pm = ck_{z\pm}/\omega$, defined as

$$\nu_\pm^2 = \varepsilon_{xx} \pm i\varepsilon_{xy}. \tag{3.23}$$

For a normal incidence with vacuum (air), the reflection coefficients are in the form

$$r_\pm = \frac{1-\nu_\pm}{1+\nu_\pm} \tag{3.24}$$

and their complex ellipsometric ratio is

$$\chi_r = \frac{r_-}{r_+}. \tag{3.25}$$

Knowing the ellipsometric ratio in the basis of circular polarizations, the azimuth

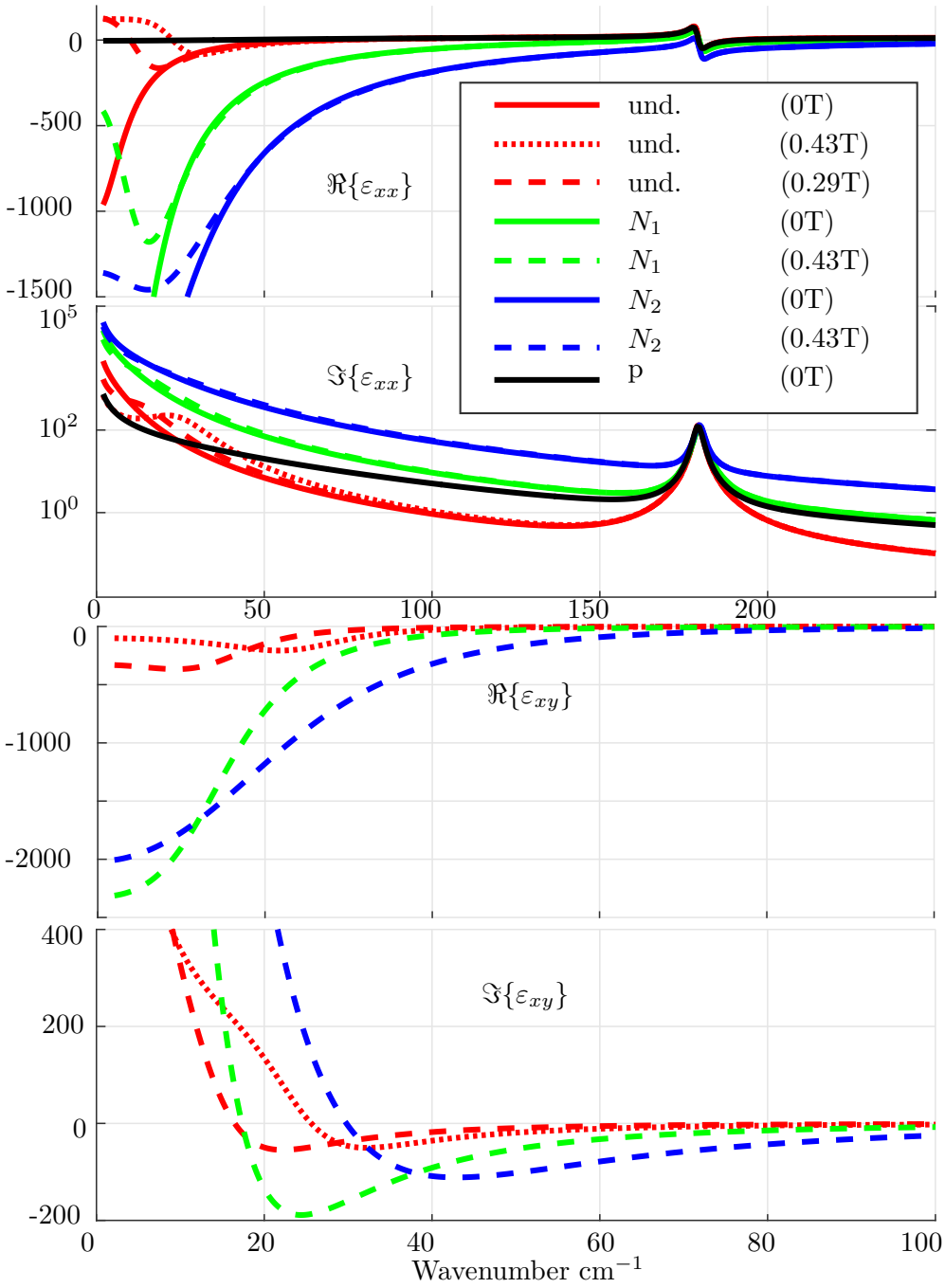

Figure 3.14: Calculated diagonal and off-diagonal complex permittivity components of all samples of InSb with and without applied magnetic field. Note the different ranges/scales to highlight important features.

change (Kerr rotation) θ and Kerr ellipticity ϵ are defined as

$$\theta = \frac{1}{2} \arg \chi_r \ , \tag{3.26a}$$

$$\tan \epsilon = \frac{1 - |\chi_r|}{1 + |\chi_r|} \ , \tag{3.26b}$$

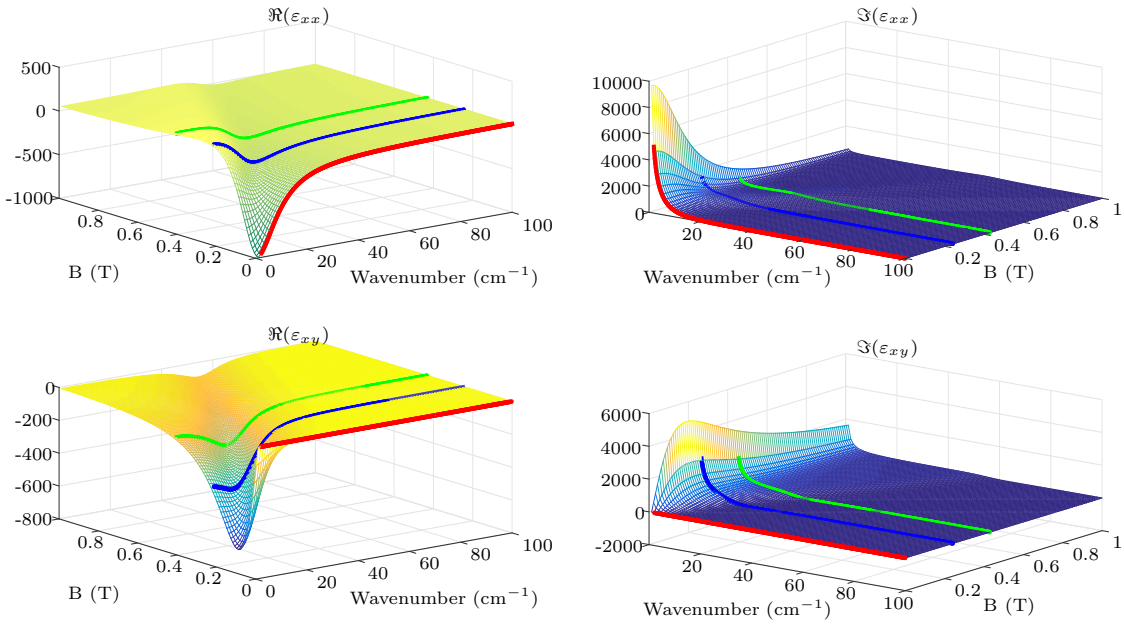

Figure 3.15: Modeled permittivity of undoped InSb in variable magnetic field in the terahertz range. Colored curves represent measurement.

where arg denotes the angle between the real axis and the complex number-origin line. A complete derivation and further discussion can be found in [87]. Figure 3.16 shows the obtained rotation and ellipticity. The Figures 3.14 and 3.16 give us the idea of the applicability of InSb as a magneto-plasmonic material. The magneto-optical effects is strongest around sharp changes in the original permittivity, either around the plasma edge or the lattice vibration. There are regions, where the materials exhibit a strong Kerr rotation, a small Kerr ellipticity while the ϵ_{zz} component remains plasmonic, for undoped InSb its bellow 50 cm^{-1} (1.5 THz). The Kerr rotation obtained here, about 20° for 0.43 T is huge compared to the millidegrees usually observed in the visible range. For the n-doped samples, the behavior is similar, only shifted towards higher frequencies. This means that even though increasing carrier concentration increases effective mass and therefore lowers the cyclotron frequency, a strong magneto-plasmonic behavior is still present, allowing for a fine-tuning of the material and device properties. The p-doped sample didn't exhibit any measurable magneto-optical activity, due to very low cyclotron frequency caused by the effective mass of the heavy holes.

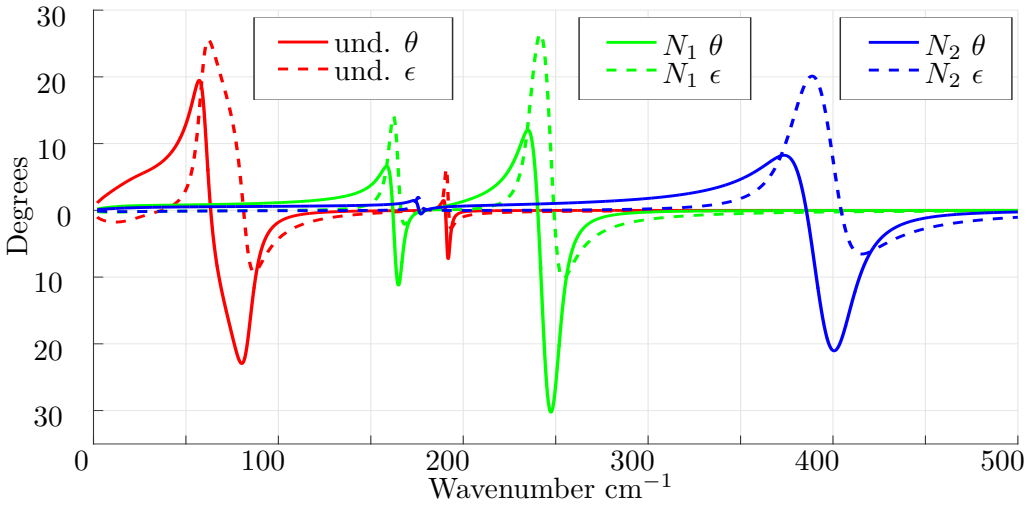

Figure 3.16: Obtained polar Kerr rotation θ and ellipticity ϵ

3.4.4 Results - Ellipsometry

While the important plasmonic properties have been extracted from the FTIR measurement, the spectroscopic ellipsometry serves as a complementary method for a more complete characterization, along with determining the thicknesses of top oxides on the wafers. The samples were measured in reflection at the incidence angles from 40° to 60°, with 5° step. The governing mechanisms for spectral function of semiconductors in the UV-visible-near IR are the optical transitions of electrons from valence band to the conduction band. This can be mathematically described as a sum of oscillators [97]. The dielectric function can also be expressed as a Kramers-Kronig consistent basis spline function (B-spline) [113]. The data analysis was as follows: First, the a thickness of a top oxide layer was fitted while the dielectric function of the semiconductor was taken from the database. Second, the top oxide thickness was fixed and the semiconductor replaced with a B-spline function with resolution (knot spacing) 0.075-1 eV. This method allows to compensate for the top oxide layer, caused by passivation. Fitting the B-spline and the top oxide thickness together would lead to a highly correlated results. We analyze the influence of doping on different semiconductors by describing the semiconductors by a B-spline function. Data for band-gap are taken from [97] used in the fitting procedure to indicate the interband absorbtion threshold.

Figure 3.17 shows the fitted permittivity of GaAs n-doped and p-doped. The top oxide has thickness 1.7 nm (n-) and 1.48 nm (p-). The data show very little change with respect to doping, only at the start of the band-gap (1.4 eV) and first absorption peak (3 eV).

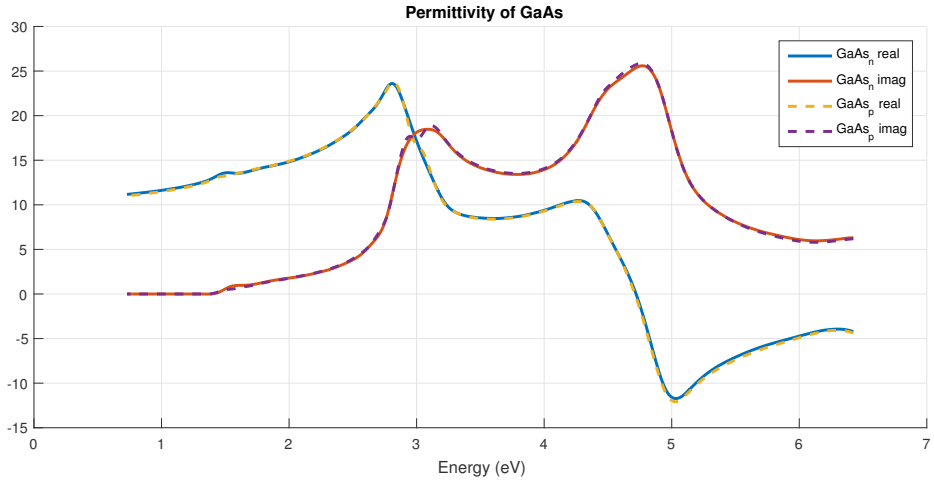

Figure 3.17: Permittivity GaAs, n-doped and p-doped as a B-spline result of fitted ellipsometric data.

Figure 3.18 shows the fitted permittivity of InP n-doped and InAs undoped. The top oxide has thickness of 1.79 nm (InP) and 2.58 nm (InAs). While these are different semiconductors, the dielectric functions offer a highlight and comparison. The band-gap, 1.35 eV for InP is clearly visible in the dielectric function as a beginning of absorptions. The band-gap of InAs, 0.36 eV is not visible in the plot but its low value is the reason for absorption in the near infrared.

Finally, Figure 3.19 provides a comparison of three cases of doping in InSb, n-doped, p-doped, and undoped. The data for the top oxide were taken from [114] and the fitted thicknesses were 3.02 nm, 6.06 nm, and 2.58 nm for n-, p- and undoped, respectively. The band-gap energy in 0.18 eV, so similarly to InAs, it is not visible in the data. However, the different concentrations and type of majority carriers are clearly present.

The thicknesses of the top oxides, measured by the spectroscopic ellipsometry are all on the order of several nanometers. The differences in thicknesses for InSb samples can be explained with the fact that without a model for surface roughness, the losses caused by any roughness on the samples will be included in the oxides.

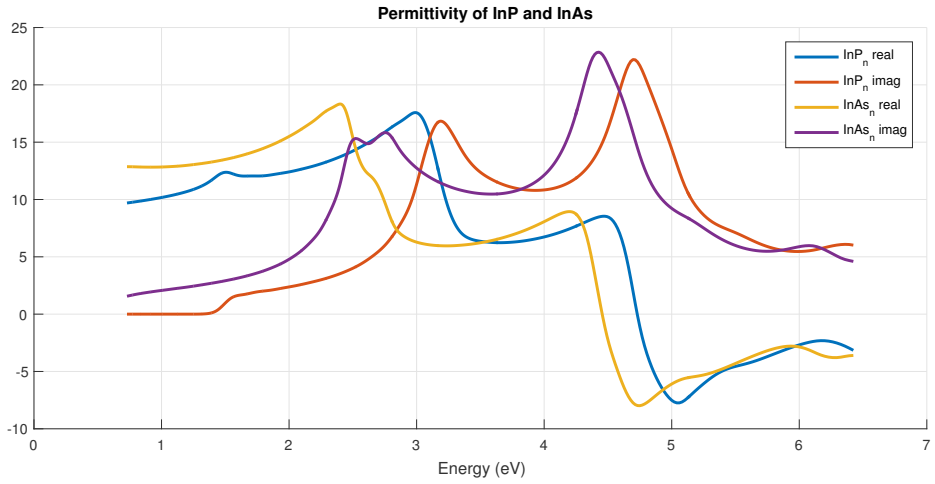

Figure 3.18: Permittivity InP, n-doped and InAs, undoped as a B-spline result of fitted ellipsometric data.

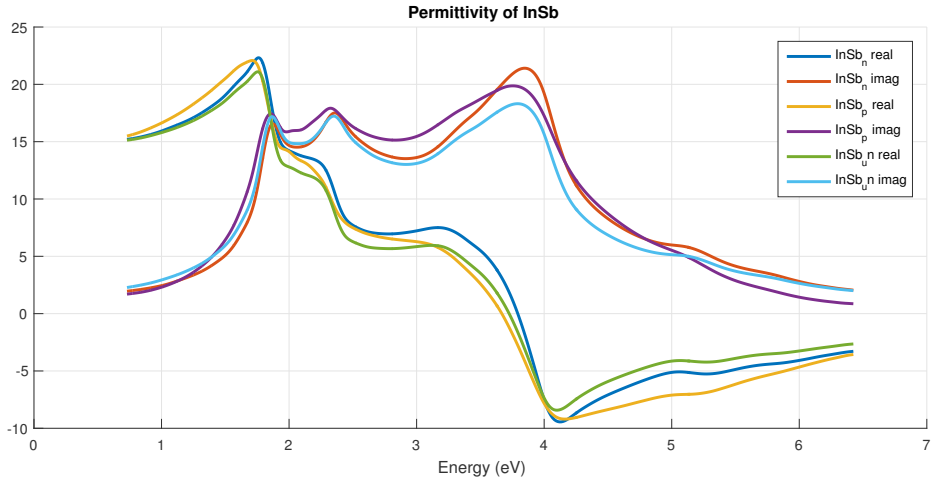

Figure 3.19: Permittivity InSb, n-doped, p-doped and undoped as a B-spline result of fitted ellipsometric data.

For smooth crystalline wafer samples, adding both top oxide and roughness would add too many correlated parameters to the model. In conclusion, the oxides should have only negligible effect on surface plasmons on the semiconductor wafers in the Terahertz spectral range.

Chapter 4

Surface Plasmons and Semiconductors

In this chapter, general information about plasmonics is reviewed. A method for finding guided modes using matrices derived in Section 2.1.4 is presented, with the addition of isotropic/anisotropic interface. Data on semiconductor permittivities obtained in the previous chapter are here evaluated in the framework of plasmonics. An experimental demonstration of Terahertz surface magneto-plasmon resonance on InSb and InAs for sensor application is presented, with discussions of different sensor architectures. Effective medium anisotropy is verified and explained as a concept of modulation of surface plasmon properties of semiconductors.

4.1 General remarks

4.1.1 Simple derivation of surface plasmon polariton

For a simple known derivation [4, 5, 7] that allows us to illustrate the basic properties of the surface plasmon, let us assume an interface between two isotropic materials with permittivities ε_1 and ε_2. We want to derive an expression for a wave that is traveling along the interface. Further assuming the electric field is in the y-z plane, the fields in the media can be described as:

$$\mathbf{H_j} = (H_{xj}, 0, 0) \exp\{i(k_y y + k_{z,j} z - \omega t)\}, \tag{4.1a}$$

$$\mathbf{E_j} = (0, E_{yj}, E_{zj}) \exp\{i(k_y y + k_{z,j} z - \omega t)\}, \tag{4.1b}$$

where $j = 1, 2$ is the index of the material. Eq. (2.7c) then yields

$$(0, ik_z H_{xj}, -ik_y H_{xj}) = (0, -i\omega\varepsilon_j E_{yj}, -i\omega\varepsilon_j E_{zj}) \tag{4.2}$$

equating the y-components

$$k_{zj} H_{xj} = \omega\varepsilon_j E_{yj}. \tag{4.3}$$

Together with the boundary conditions $E_{y1} = E_{y2}$, $H_{x1} = H_{x2}$ and $\varepsilon_1 E_{z1} = \varepsilon_2 E_{z2}$ leads to expressions for components of the wavevector $\mathbf{k}$:

$$\begin{aligned} \frac{k_{z1}}{\varepsilon_1} &= \frac{k_{z2}}{\varepsilon_2} \\ k_{y1} &= k_{y2} \end{aligned} \tag{4.4}$$

Given that $\mathbf{k}_j^2 = \varepsilon_j(\frac{\omega}{c})^2 = k_y^2 + k_{zj}^2$ inserted into (4.4) finally yields

$$k_y = \frac{\omega}{c}\sqrt{\frac{\varepsilon_1\varepsilon_2}{\varepsilon_1+\varepsilon_2}}, \tag{4.5a}$$

$$k_{zj} = \frac{\omega}{c}\sqrt{\frac{\varepsilon_j^2}{\varepsilon_1+\varepsilon_2}}, \tag{4.5b}$$

or as normalized components of the wavevector $\mathbf{k} = k_0(\nu_x, \nu_y, \nu_z)$

$$\nu_y = \sqrt{\frac{\varepsilon_1\varepsilon_2}{\varepsilon_1+\varepsilon_2}}, \tag{4.6a}$$

$$\nu_{zj} = \sqrt{\frac{\varepsilon_j^2}{\varepsilon_1+\varepsilon_2}}. \tag{4.6b}$$

For the wave to be traveling along the interface, following conditions must be fulfilled. First, the normal component of the wavevector ν_z must be imaginary, so that the wave is not radiating from the interface and second. The propagation component ν_y must be real, for a propagation in that direction. To achieve this, permittivity of one of the materials (e.g. ε_2) must be negative and in absolute value greater than ε_1. In reality permittivity is usually complex, however the condition for negative real part remains. The difference between the real a ideal scenario is discussed in the next section.

The relations (4.4) also have a constant solution at frequency ω_{op} derived by Cada et al. [115], tied directly to semiconductors. It points to a solution when the permittivity of the doped semiconductor ε_{DS} and the dielectric ε_D are equal. For simplicity lets omit absorptions and rewrite the permittivity of the semiconductor as

$$\varepsilon_{DS} = \varepsilon_S - \frac{\omega_p^2}{\omega^2}, \tag{4.7}$$

where ε_S it the total background permittivity, coupling together the constant permittivity and lattice vibrations. The solution ω_{op} is then

$$\varepsilon_D = \varepsilon_{DS} \tag{4.8}$$

$$\omega_{op}^2 = \frac{\omega_p^2}{\varepsilon_D - \varepsilon_S}. \tag{4.9}$$

With the knowledge of ε_S and ε_D the plasma frequency can be determined from the position of the minimum of reflectivity. The value of the minimum in reflectivity can be used to estimate the damping of the free carriers. [100] If the sample is non-absorbing, the minimum would be zero. For absorbing samples the the damping can be calculated as

$$\gamma_p = \frac{\omega_{op}^3}{\omega_p^2} \frac{4\sqrt{R_{min}(1 + R_{min})}}{(1 - R_{min})^2}. \tag{4.10}$$

It is worth pointing out that the plasma frequency can also be extracted from Raman scattering measurements, where the measured Raman shifts correspond to a coupled mode consisting of plasma and phonon oscillation.

4.1.2 Note on the terminology

As any scientific and engineering field, plasmonics has its own established terminology, which should be maintained for clear communication of concepts, ideas, and results. This section clarifies the use of several terms in plasmonics.

Surface plasmon is a collective oscillation of free carriers at the surface of conductor. Plasmon is a quasiparticle, a quantum of oscillation.

Surface plasmon polariton is a coupled electromagnetic wave to the free carrier oscillation at the interface between dielectric and metal. Part of the electromagnetic energy is stored in the longitudinal collective oscillation (in the direction of propagation) of the free carriers [5].

Bulk plasmon or a volume plasmon is a collective oscillation of carriers traveling through the bulk of the material. Rigorous analysis of the local currents and electric field caused by charge carrier density oscillations point to two solutions [96]. For $\omega > \omega_p$, the material can support transversal electromagnetic waves. In optics terms, this means that the material is dielectric. For frequencies below ω_p,

the electromagnetic waves are reflected. The only propagating modes possible below the plasma frequency are through the surface plasmon. For the case, when $\omega = \omega_p$, i.e. the permittivity equals zero, the system can support longitudinal, electric modes, independent of wavevector. However electromagnetic wave with frequency ω cannot excite the mode at ω_p, since electromagnetic waves are transversal and the mode purely longitudinal, except for very thin metallic films ($\sim$ 10 nm), where the modes produce a standing wave [116]. The usual way to excite and observe the volume longitudinal plasmons is through the electron loss spectroscopy, where a high energy electron beam illuminates the sample. The modes are observed as an energy loss, at quantized plasma frequency ($n\hbar\omega_p$, n being the number of plasmons excited).

4.1.3 Surface plasmon polariton properties

Dispersion Curves

The two interesting cases, where material has negative real permittivity is either due to plasmonic oscillations (Drude model) or lattice-phononic vibrations (Lorentz model). For surface waves guided by these mechanism are coined terms surface plasmon polariton and surface phonon polariton. Nomenclature notwithstanding, the physical principle of guiding the surface wave is the same - the electromagnetic wave can propagate along the surface, in dimensions smaller than the refractive limit because part of the electrical energy is carried by a different mechanism, oscillations of the free carriers or the lattice [117]. Since both of these mechanisms are wavelength dependent, we illustrate them using a dispersion curve, which links together the propagation component of the wavevector and the wavelength. The normalized components is sometimes called the propagation constant and can be thought of as an effective refractive index of a waveguide that is the interface.

Lets illustrate the dispersion curve on a theoretical example. Assume a boundary between a dielectric material with permittivity ε_1 and conductive material ε_2, which is governed by the Drude model 3.2.1 with the plasma frequency ω_p and the background permittivity $\varepsilon_\infty = 1$. First without damping, where the Drude term reduces to

$$\varepsilon_2 = \varepsilon_\infty - \frac{\omega_p^2}{\omega^2}, \tag{4.11}$$

and second with damping $\gamma_p = 0.05\ \omega_p$. Figure 4.1 shows the relation between the propagation constant and the frequency. Technically the calculation is done in reversed order, frequency →permittivity →propagation constant, but this is the prevailing method of plotting the dispersion curve. The frequency axis is normalized to the plasma frequency and the propagation constant is normalized to the propagation constant of a wave with plasma frequency ($k_{0,p} = \omega_p/c$).

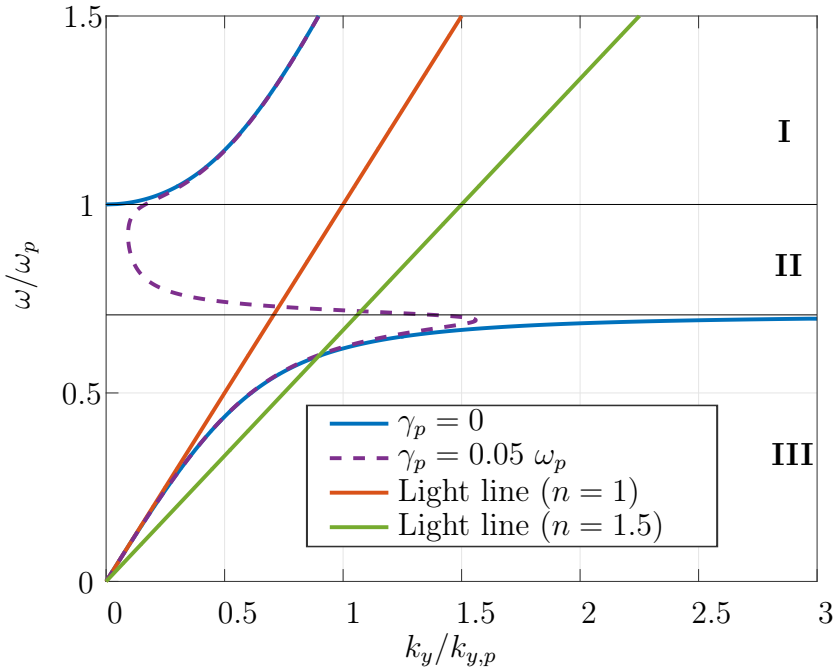

Figure 4.1: Dispersion curve of surface plasmon at the interface between Drude metal and air

For the case without damping, the dispersion curve is divided into three regions:

Region I: $\varepsilon_2 > 0$, above ω_p means that both ν_y and ν_y are real, the curve is on the right of the light line, meaning this region is radiative. In practice this is the solution to the Brewster angle. There is no guided wave possible at the interface of two dielectric isotropic materials.

Region II: $\varepsilon_2 < 0 \wedge |\varepsilon_2| < \varepsilon_1$ leading to imaginary ν_y and real ν_z, this region is sometimes called quasi-bound. The region is located between ω_p and $\frac{\omega_p}{\sqrt{\varepsilon_\infty + \varepsilon_1}}$ (which can be proved from the region's conditions).

Region III : $\varepsilon_2 < 0 \wedge |\varepsilon_2| > \varepsilon_1$. This region has real ν_y (allowing propagation) and imaginary ν_z (surface confinement). This is the region of *surface plasmon*.

The regions hold true even for the real case with damping, but now the solution of propagation constant is continuous and has a finite value. The diagonal line is called the light line, and corresponds to the propagation of an electromagnetic wave in the dispersionless material ε_1, as $k_y = \sqrt{\varepsilon_1}\ \omega/c$. In the low frequency limit, the propagation of the surface plasmon is similar to the propagation of electromagnetic wave in dielectric, in a so-called Zenneck regime [23, 118]. In this regime, the propagation attenuation is small, but the confinement to the conductor is negligible. Section 4.3.1 discusses this topic.

By looking at the full geometry, when the incident light has the propagation constant $\nu_y = \sqrt{\varepsilon_1}\sin\theta$, where θ is the angle of incidence, it is obvious that the surface plasmon cannot be excited by varying the angle of incidence only. Either a three layer system needs to be used, where higher refractive index material acts as a coupling prism, which changes the incident wavevector so that it matches the one of the surface plasmon - shown as the intersection of the green light line and SP in Figure 4.1. Further coupling schemes rely on end-fire coupling [119] use of gratings [11], where the incident wavevector is influenced by the period of the grating Λ, as

$$\nu_y = \sqrt{\varepsilon_1} + m\frac{\lambda}{\Lambda}\ , \tag{4.12}$$

where m is an integer. The dispersion curves of real materials exhibit disturbances from the ideal model. For noble metals the Drude term overlaps the interband absorbtions [4], limiting for example the use of Gold for higher frequencies [120, 121]. For our case of III-V semiconductors, the disturbance comes from lattice vibrations. Figure 4.2 shows three real cases of surface plasmon/phonon polariton on undoped InSb and n- and p- doped GaAs, derived from the permittivity measurement in Section 3.4. The dielectric material is air. The dispersion curve is plotted as the real part of the propagation constant of surface wave versus the wavenumber. In this projection, the light line in air is vertical and any wave with $\Re(\nu_y) > 1$ corresponds to a surface wave. For the case of undoped InSb there are two regions with surface waves - for lower energies it's the surface plasmon polariton and for higher energies it's the surface phonon polariton. Similar case is for the n-doped GaAs, the difference being that it's plasma frequency is higher than its phonon frequency. The possible surface wave is then a combination of both plasmon and phonon polariton. There

is one energy stop band around 250 cm^{-1} when the phonon raises the permittivity above zero. The p-doped GaAs also has higher plasma frequency, but the SPP is very damped due to low mobility of the majority carriers - heavy holes.

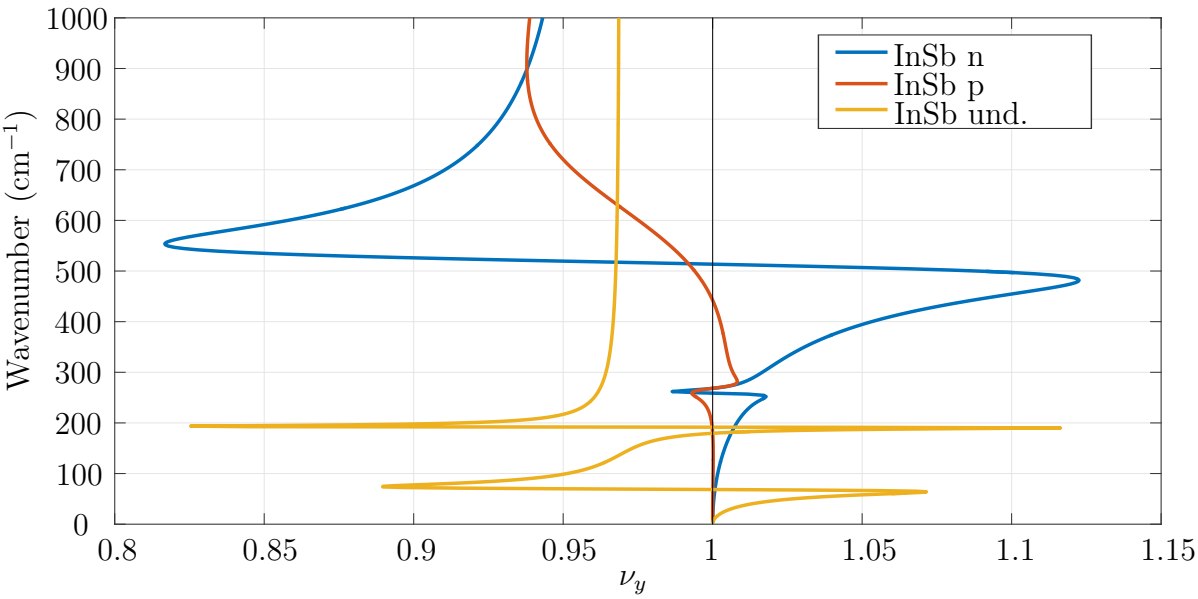

Figure 4.2: Dispersion curves for selected cases of semiconductors. For n-doped InSb, the surface plasmon region is below 500 cm − 1, but broken by the effect of lattice vibrations around 250 cm − 1. Similar case is for p-doped InSb, but the avalaible wavevectors are limited due to increased damping in the material. In undoped InSb the lattice vibrations actually allow for a brief existence of surface phonon, at around 200 cm − 1. The plasmonic region starts around 0 cm − 1.

While the dispersion curves calculated from the simple derivation are a useful tool to assert the behavior of surface plasmons, they do not cover all the aspects of SPP properties. More useful metrics can be, depending on the intended purpose the confinement and propagation length defined in the next section. Furthermore, the dispersion curves and their analytical derivation can lead to "phantom" solutions, e.g. the Brewster angle or in other cases such as the existence of leaky modes in observation of different type of surface waves, the D'yakonov waves [122]. The choice of a coupling mechanism also influences the properties of the surface plasmon, in prism configuration there is also interference in the middle layer. This is also observable on gratings, with the addition of possible cavity modes [123] for metallic gratings. A guided mode analysis and a field analysis is therefore needed for correct understanding and prediction of real surface plasmons.

Propagation and confinement characteristics

From the calculation of the complex wavevector components, we can calculate the propagation length of the surface plasmon and the penetration into the materials. There are different ways to define the figure of merit of surface plasmon, each favored by different authors. First lets look at the physical meaning of H_x, the x component of the magnetic complex amplitude of the surface plasmon in isotropic materials. It has its real and imaginary part, responsible for the wave nature (oscillation) of the surface plasmon. The absolute value of $|H_x|$ is the field amplitude and the field amplitude squared, $|H_x|^2$, normalized to the initial value is the relative intensity. Both the field amplitude and the relative intensity can be used to characterize the propagation of surface plasmon.

For illustration, lets take the real value of the magnetic field

$$H_{x,j} = \exp\left[-i(k_y y + k_{z,j} z)\right],\ j = 1, 2 \tag{4.13}$$

from our previous example ($\gamma_p = 0.05\omega_p$) at the frequency $\omega = \omega_p/2$, where $\varepsilon_2 = -2.9604 + 0.3960i$. The 2D plot of the real part of the complex amplitude is plotted in Figure 4.3. We see the field oscillation of the surface plasmon polariton along the propagation path (y-direction) and exponential decay to both materials, stronger to the conductive one.

Next, Figure 4.4 details the propagation along the y-direction. The real and imaginary part oscillate as expected, the field amplitude follows the field maxims. Both the amplitude and the intensity decay with exponential factor. The two main metrics used in literature to define the propagation length of the SPP, denoted L_{SPP} are either $1/\Im(k_y)$, when the field amplitude drops to 1/e and intensity to $1/e^2$ or $1/[2\Im(k_y)]$, when the relative intensity decreases to 1/e.

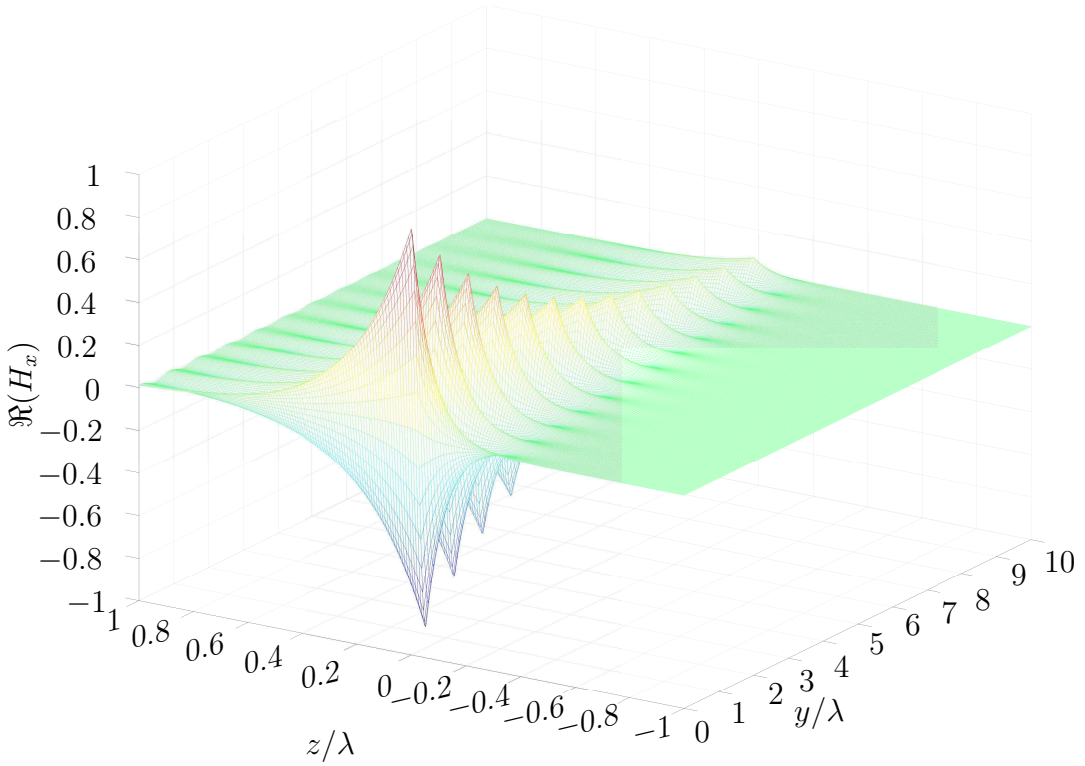

Figure 4.3: Surface plasmon field profile of the real part of H_x

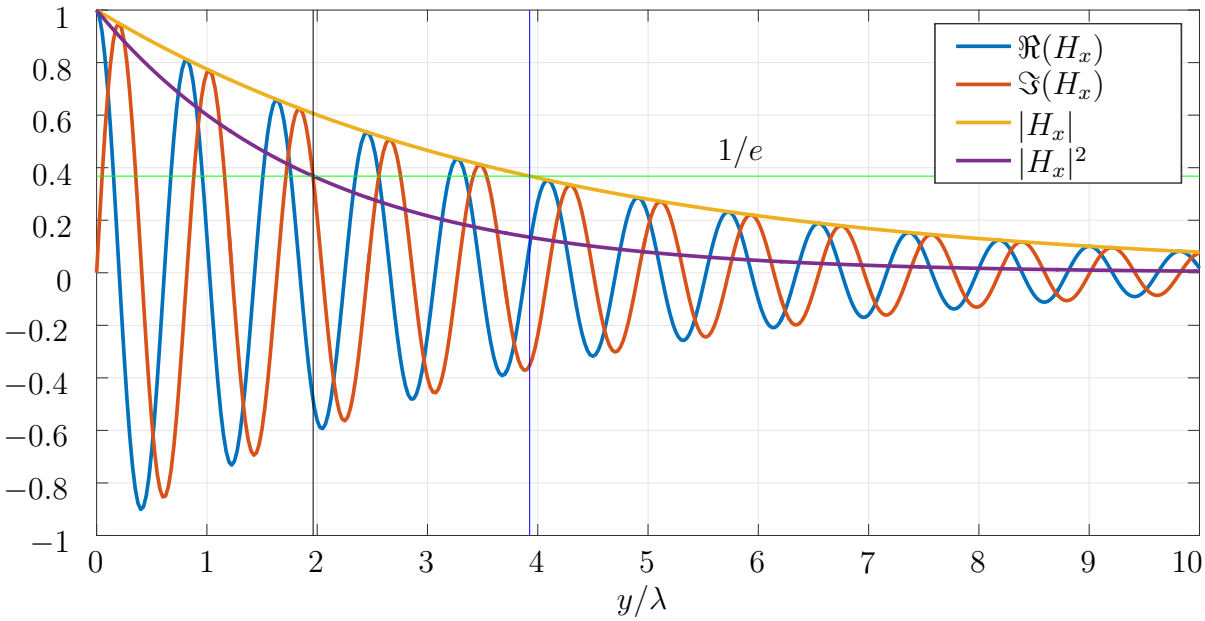

Figure 4.4: Field and amplitude of surface plasmon propagation with highlighted metrics for $z = 0$. The propagation distance is normalized to the free space wavelength.

Similar principle applies to the metric of confinement, i.e. how much field or how much intensity is carried on the interface in the respective materials. Again this is usually defined by the decrease to value of 1/e. For the field the confinement length it's $L_j = 1/\Im(k_{z,j})$ and for the intensity it's $L_j = 1/2\Im(k_{z,j})$. The field and intensity profile is plotted in Figure 4.5. Interestingly, the propagation is usually defined via the intensity $1/[2\Im(k_y)]$ while the confinement through the field as $1/\Im(k_z)$.

In this thesis we will use the definition via decay of field amplitude, i.e. $1/\Im(k_z)$ for confinement and $1/\Im(k_y)$ for propagation.

4.2 Guided conditions, special solutions

4.2.1 Waveguiding condition

We use the Berreman and RCWA formalism to calculate, design, and interpret data in optical measurements, be it in reflection, transmission or ellipsometry. The algorithm however carries much more information than just the observable quantities [84,86,87]. The focus of this thesis is the surface plasmon polariton - the guided wave along the

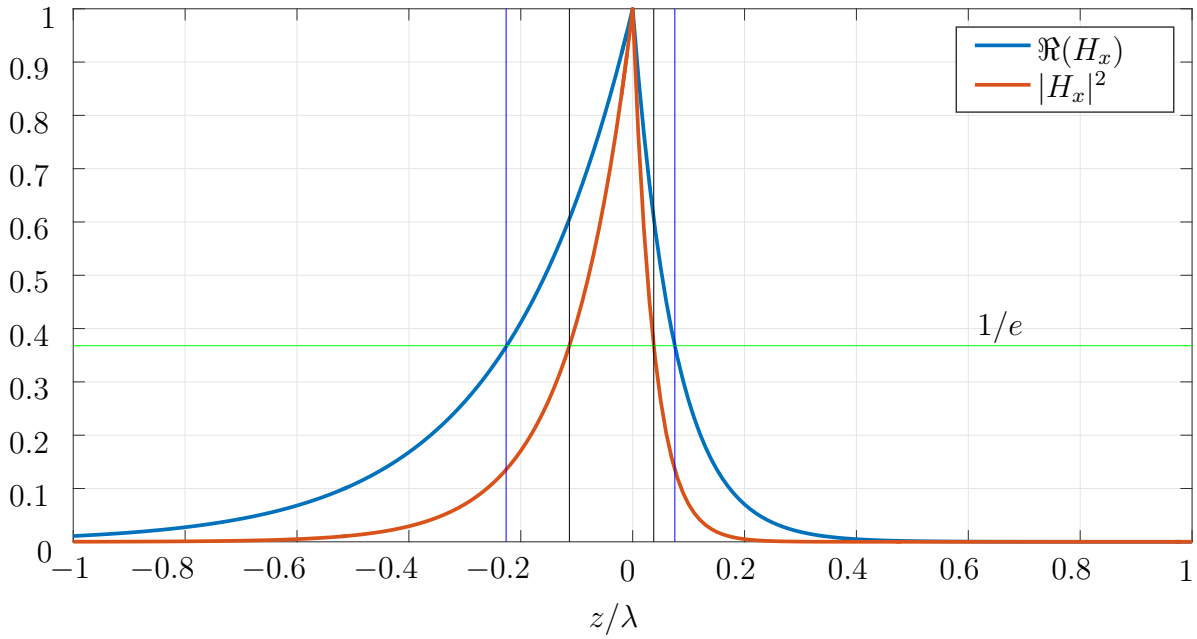

Figure 4.5: Real part of complex amplitude H_x and intensity of surface plasmon confinement with highlighted metrics. The z-axis is normalized to the free space wavelength. Real part of the complex amplitude was chose to illustrate, that the field does not oscillate.

interface. We need to analyze and understand its behavior in multilayers, nanostructures, and gratings. This chapter shows how it is possible to obtain dispersion curves and field profiles for guided waves from the formalism. First subsection illustrates the concept on a single boundary using the M-matrix method and the second part defines the singular value decomposition, used with the S-matrices.

Illustration on M-matrix for single boundary

Recall equations 2.44 and 2.62. Suppose we have one boundary of two materials, ε_1 and ε_2. This gives us two $\mathbf{T}$-matrices $\mathbf{T}^{(0)}$ and $\mathbf{T}^{(1)}$. The formula for the M-matrix

$$\mathbf{M} = [\mathbf{T}^{(0)}]^{-1}\mathbf{T}^{(1)} \tag{4.14}$$

gives

$$\mathbf{M} = \begin{pmatrix} \frac{\sqrt{\varepsilon_1-\nu_y{}^2}+\sqrt{\varepsilon_2-\nu_y{}^2}}{2\sqrt{\varepsilon_1-\nu_y{}^2}} & \frac{\sqrt{\varepsilon_1-\nu_y{}^2}-\sqrt{\varepsilon_2-\nu_y{}^2}}{2\sqrt{\varepsilon_1-\nu_y{}^2}} & 0 & 0 \\ \frac{\sqrt{\varepsilon_1-\nu_y{}^2}-\sqrt{\varepsilon_2-\nu_y{}^2}}{2\sqrt{\varepsilon_1-\nu_y{}^2}} & \frac{\sqrt{\varepsilon_1-\nu_y{}^2}+\sqrt{\varepsilon_2-\nu_y{}^2}}{2\sqrt{\varepsilon_1-\nu_y{}^2}} & 0 & 0 \\ 0 & 0 & \frac{\varepsilon_1\sqrt{\varepsilon_2-\nu_y{}^2}+\varepsilon_2\sqrt{\varepsilon_1-\nu_y{}^2}}{2\sqrt{\varepsilon_1}\sqrt{\varepsilon_2}\sqrt{\varepsilon_1-\nu_y{}^2}} & \frac{\varepsilon_1\sqrt{\varepsilon_2-\nu_y{}^2}-\varepsilon_2\sqrt{\varepsilon_1-\nu_y{}^2}}{2\sqrt{\varepsilon_1}\sqrt{\varepsilon_2}\sqrt{\varepsilon_1-\nu_y{}^2}} \\ 0 & 0 & \frac{\varepsilon_1\sqrt{\varepsilon_2-\nu_y{}^2}-\varepsilon_2\sqrt{\varepsilon_1-\nu_y{}^2}}{2\sqrt{\varepsilon_1}\sqrt{\varepsilon_2}\sqrt{\varepsilon_1-\nu_y{}^2}} & \frac{\varepsilon_1\sqrt{\varepsilon_2-\nu_y{}^2}+\varepsilon_2\sqrt{\varepsilon_1-\nu_y{}^2}}{2\sqrt{\varepsilon_1}\sqrt{\varepsilon_2}\sqrt{\varepsilon_1-\nu_y{}^2}} \end{pmatrix}. \tag{4.15}$$

Any guided wave in the structure means in our definition that no field comes in from the top or bottom, but some can come out. For a TM wave that means the element $M_3 3 \to 0$. Written out it's

$$\frac{\varepsilon_1\sqrt{\varepsilon_2-\nu_y{}^2}+\varepsilon_2\sqrt{\varepsilon_1-\nu_y{}^2}}{2\sqrt{\varepsilon_1}\sqrt{\varepsilon_2}\sqrt{\varepsilon_1-\nu_y{}^2}} = 0. \tag{4.16}$$

After a little math we see that for the condition to be satisfied, our normalized wavevector component ν_y must be

$$\nu_y = \sqrt{\frac{\varepsilon_1\varepsilon_2}{\varepsilon_1+\varepsilon_2}}, \tag{4.17}$$

which is exactly the formula for the dispersion of surface plasmon (4.6a). The general condition for guided wave is

$$M_{11}M_{33} - M_{13}M_{31} = 0, \tag{4.18}$$

which includes both polarizations and mode conversion, but the analytical formulas get long and complicated very fast and the use of computer optimization is necessary.

Since we are using the S-matrix formalism for all the calculations (Section 2.2.1), it is at hand to use it for the waveguiding condition as well. This is done using the singular value decomposition.

Singular Value Decomposition

The principle in calculation of the waveguiding condition - nothing in, something out, is the same in S-matrix formalism. The principle is described as

$$A^{(\mathrm{out})} = SA^{(\mathrm{in})} \tag{4.19}$$

$$A^{(\mathrm{out})} = S\ 0. \tag{4.20}$$

It is possible to solve (4.20) with the condition that determinant $|\mathrm{S}| = \infty$ there is better formalism available [124, 125]. Let us multiply the equation with inverse S

$$\mathrm{S}^{-1} \begin{bmatrix} A_{up}^{(0)} \\ A_{down}^{(N)} \end{bmatrix} = \begin{bmatrix} 0 \\ 0 \end{bmatrix}, \tag{4.21}$$

and do a singular value decomposition, which is

$$\mathrm{S} = \mathrm{U}\Sigma\mathrm{V}^{T}; \quad \mathrm{S}^{-1} = \mathrm{V}\Sigma^{-1}\mathrm{U}^{H} \tag{4.22}$$

Superscript T denotes the transpose, H is the conjugate transpose, U is the matrix of left singular vectors and Σ is the diagonal matrix of singular values (σ_{max} being the maximum one) and V is the matrix of right singular vectors. This leads to

$$\mathrm{S}^{-1}\mathrm{U} = \mathrm{V}\Sigma^{-1}, \tag{4.23}$$

which is the solution to our problem. In optimization we seek the minimum value of $1/\sigma_{max}$. The benefit of the Singular value decomposition is that in addition to the waveguiding condition, we get V^{T}, which is the vector of amplitudes of outgoing modes. This allows us to plot and study the field profile of the modes in the structure.

Surface plasmon at anisotropic interface

Studying surface waves/plasmons at the interface of anisotropic and isotropic materials has usually been directed at the case anisotropic (uniaxial, biaxial) dielectric and isotropic conductor [118, 126, 127], where the orientation of the principal axes of the anisotropic dielectric influence the surface plasmon properties.

Interesting topic in anistotropic surface waves is the Dyakonov (or D'yakonov) waves [118, 122, 128, 129]. They are surface waves guided by one isotropic and one anisotropic dielectric, so they are not surface plasmon (oscillation of free carriers), but can propagate along interface. This purely dielectric (non-absorbing) property would be promising, but their guiding condition is not easily attainable. The isotropic permittivity ε_1 must be between the anisotropic $\varepsilon_{2,xx} > \varepsilon_1 \varepsilon_{2,yy}$) and the direction propagation must be at an azimuthal angle to the principal axes.

Other interesting cases geared towards special functionality (non-reciprocal, tuning applications) are based on multilayers of isotropic dielectric, conductor and magneto-optical material [123, 130].

Interesting question arises with the observed strength of the magneto-optical effect in semiconductors for infrared and terahertz frequencies. Two diagonal components of the permittivity tensor can completely change sign. Which of the diagonal components of permittivity of the conductor is responsible for the plasmonic behavior?

Starting with defining the permittivities, one isotropic material with the tensor ε_1 and one biaxial with $\hat{\varepsilon}_2$, defined as

$$\hat{\varepsilon}_1 = \begin{bmatrix} \varepsilon_1 & 0 & 0 \\ 0 & \varepsilon_1 & 0 \\ 0 & 0 & \varepsilon_1 \end{bmatrix}, \quad \hat{\varepsilon}_2 = \begin{bmatrix} \varepsilon_{2,xx} & 0 & 0 \\ 0 & \varepsilon_{2,yy} & 0 \\ 0 & 0 & \varepsilon_{2,zz} \end{bmatrix}. \tag{4.24}$$

With the **T**-matrix defined in Section 2.1.4, we can replicate the same method as in Eqs. (4.14) to (4.17), giving us the tangential component of the surface plasmon at an isotropic/biaxial interface

$$\nu_y = \sqrt{\frac{\varepsilon_1 \varepsilon_{2,zz}(\varepsilon_{2,yy} - \varepsilon_1)}{\varepsilon_{2,yy}\varepsilon_{2,zz} - \varepsilon_1^2}}. \tag{4.25}$$

This equation is suitable to describe both isotropic conductor/anisotropic dielectric and anisotropic conductor/isotropic dielectric. The components from the anisotropic material that will influence the surface plasmon are $\varepsilon_{2,yy}$ and $\varepsilon_{2,zz}$.

For anisotropic dielectrics this means that by rotating the material, we can change the properties of the surface plasmon [131]. For conductors this gives us guidelines on choosing the direction of anisotropic modulation for the strongest effect. In subwavelength gratings, the orientation of lamells along y-direction modulates the plasmonic components. While (4.25) doesn't fully describe the magneto-optical configuration, it allows us to deduce that the transversal configuration (Figure 2.2) is the most suitable for surface plasmon manipulation - it affects both diagonal plasmon components.

4.3 Plasmonics in Semiconductors

4.3.1 Suitable ranges for SPP generation

An ideal plasmonic material would allow a long propagation length of the SPP along the interface and sufficient confinement into the metallic (conductive) material; in other words short extension into the dielectric. When the difference between the

permittivities ε_1 and ε_2 is large, the SPP can propagate on the distance of many wavelengths, but is poorly guided by the interface (a small penetration depth into the conductor) and most of its energy is carried in the dielectric- this is the Zenneck regime. The opposite is also valid - a heavily confined wave will have a lot of energy traveling in the absorbing material, and thus the propagation length is short.

Noble metals such as gold or silver are used for plasmonic applications in the visible and near-infrared range [4, 7, 50]. By comparing the properties of the SPP on gold in the visible range and on semiconductors in the THz range, one can estimate how suitable the semiconductors are for plasmonic applications in the THz range. There are other metrics usable for describing the figures of merit of surface plasmon [132]. We have opted for the comparison of the propagation length (along the interface) and the penetration (into the conducting material) normalized to the free space wavelength of light. The results are shown in Figure 4.6.

As Figure 4.6 shows, the properties of semiconductors in the THz are almost identical to that of gold and silver in the visible range. For longer wavelengths, the trends on noble metals continue linearly to smaller confinement and longer propagation.

The semiconductors have several advantages. The adjustable doping concentration can significantly change the behavior of semiconductor, as can be seen from comparing the three samples of InSb. Even the p-doped sample is shown to be able of sustaining a surface plasmon for low energies. Therefore, doping can be used to fine-tune the plasmonic properties of semiconductors. Other techniques, such as optical pumping, electric gating, or as demonstrated in the next section, magneto-optics allow for further tuning, switching or modulation of surface plasmons on semiconductors. The gaps in the curves, caused by the phonon, and the rapid change of behavior around them, lead to a surface phonon polariton (i.e. on the undoped InSb) or a combination of both, where the electromagnetic energy is stored not just in the collective oscillation of the free carriers, but also in the vibrations of the lattice.

The bands highlighted in Figure 4.6 correspond to possible communication windows for Terahertz frequencies [2, 3]. Semiconductor plasmonic properties have also been used in Terahertz detectors [133] or as shown in the next section, for Terahertz surface plasmon resonance sensor.

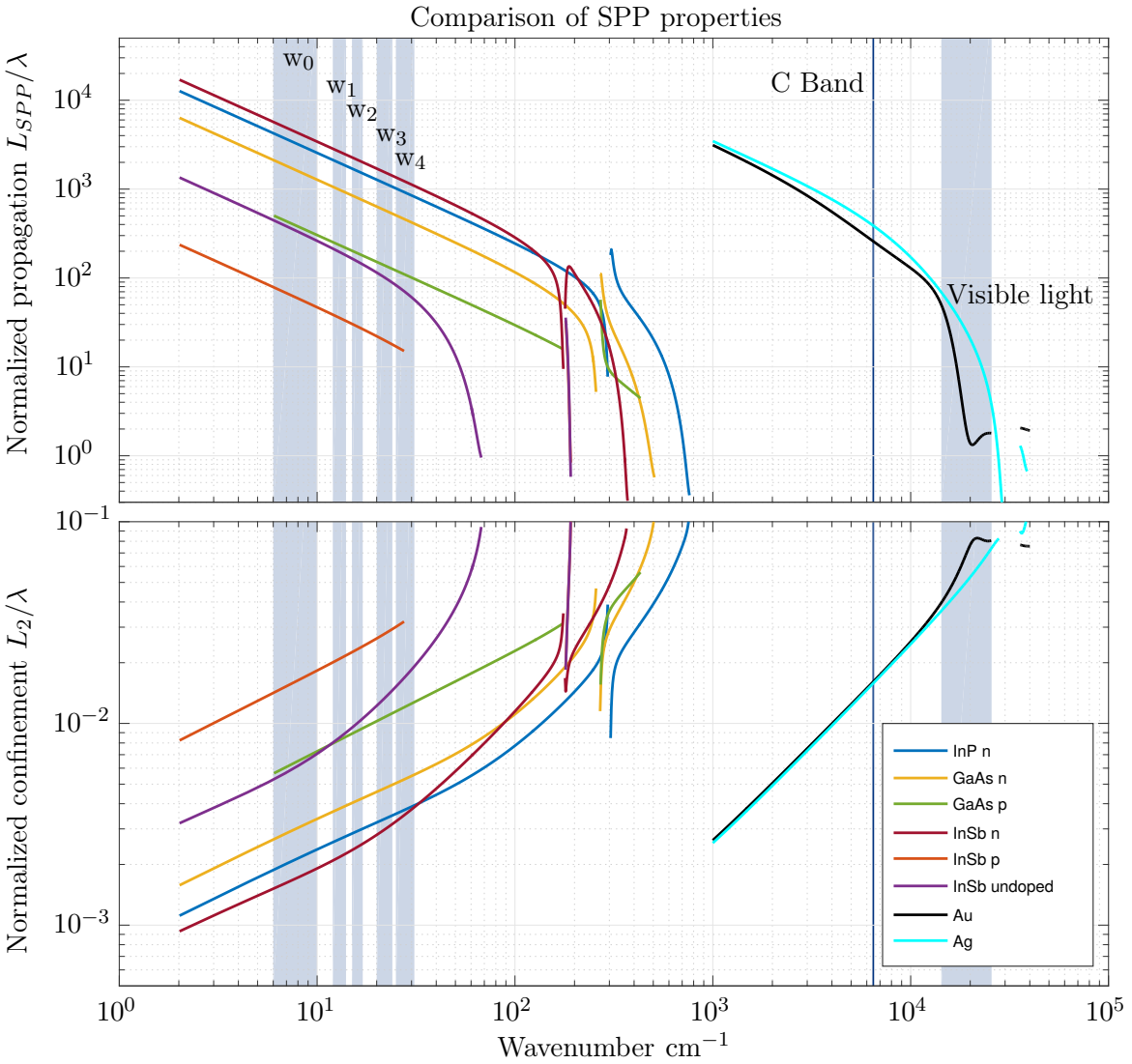

Figure 4.6: Comparison of normalized propagation length (top) and material confinement (bottom) of SPP on selected semiconductors and noble metals. The gaps in the curves are caused by either the phonon (semiconductor) or band absorptions (Au, Ag), where the real part of permittivity is greater than -1. The x-axis is the logarithmic scale of wavenumber, 10^4 cm^{-1} corresponds to wavelength of 1μ m. The y-axis is normalized to the wavelength used (λ), i.e. a number of wavelengths the SPP propagates before decaying to $1/e$. Data for Au and Ag were taken from [1]. Highlighted areas w$_0$-w$_4$ show the bands of THz radiation considered for communications applications due to atmospheric absorbtions [2, 3], compared to the infrared C band and visible light.

4.3.2 Tunable Magnetoplasmonic THz SPR sensor

We have seen in Section 3.4 that both the undoped InSb and InAs have their plasma frequency in the Terahertz domain. This points to a possibility of constructing an SPR sensor based on these materials. Experimental demonstrations such sensor is still missing in the Terahertz domain, with only theoretical designs published [51,54,134]. This sensor will be useful for subwavelength probing of materials in the Terahertz domain with high label-free (without a reporting agent) sensitivity.

The typical configuration of an SPR sensor is based either on the Kretschmann or Otto architecture, both depicted in Figure 4.7. The high refractive index prism is used to match the wavevector of the evanescent wave to the surface plasmon polariton at the interface between the conductor and analyte. In the Kretschmann configuration, the conductor is deposited as thin film on the prism and the analyte is placed on the top. In the Otto configuration, the conductive material is pressed towards the prism, with the dielectric-analyte sandwiched between them.

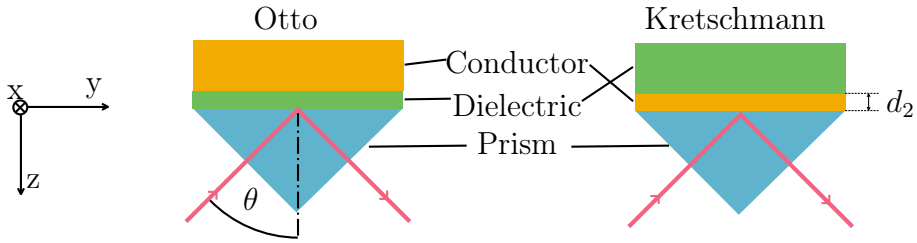

Figure 4.7: Coordinate system and two discussed configurations for SPR excitation.

Experimental Otto configuration

Thick wafers (500 μm) of InSb and InAs (measured in Section 3.4), and a thick layer on Au on glass, were used as the conductors, the dielectric was chose as a thin polymer film (high density polyethylene), about 15 μm thick. They were pressed together using manual anvil on a Silicon prism ($n = 3.4164$ [135]) with the angle of incidence $\varphi = 35°$ - originally an attenuated total reflection system (ATR). The reference was the signal from the empty prism.

The experimental data showing the prism coupled surface plasmon resonance are presented in Figure 4.3.2. Blackmann-Harris three term apodisation [136] is used

to smooth the signal. The left plot in Figure 4.3.2 shows the transversal-magnetic (TM, or p-polarized) reflectivity obtained from the experiment. The sharp decrease in reflectivity for both the InSb and InAs shows the surface plasmon resonance. The gold sample acts only as a reflector. A model was fitted to the measured data, denoted by dashed lines in the plot. Fitted values of the refractive index and the thickness of the dielectric are $n_2 = 1.625$ and $d_2 = 23.4$ μm (with InSb) and $d_2 = 15.8$ μm (with InAs), the difference in thickness caused by the strength of the manual pressing on different samples. Reasonable agreement between the data and the model was achieved. Using the fitted model, it is possible to calculate the field profiles at the resonance. For Au and reference, the wavelength was chosen as the same as for resonance in InSb. The THz field intensity profiles, normalized to the intensity of the wave in the prism, depicted in Figure 4.3.2 (right subplot) show a clear field concentration at the interface of the dielectric and InSb and InAs. The field intensity profiles prove that the observed resonances correspond to surface plasmon polariton. The empty prism provides only evanescent wave penetration and the Au sample (permittivity from [99]) has only skin depth wave confinement, without any field concentration on the interface.

As explained in Section 3.4, the permittivity of semiconductors with low effective mass is easily tuned by an external magnetic field. Section 4.2.1 and Eq. (4.25) show that the largest modulation will be achieved using the transversal magneto-optical configuration, where the magnetic field is along the x-axis, i.e. perpendicular to the plane of incidence. This configuration changes the diagonal (ε_{yy}, ε_{zz}) and off-diagonal (ε_{yz} and ε_{zy}) components of the permittivity tensor. The diagonal components are responsible for the plasmonic behavior while the off-diagonal components, which arise with external magnetic field are responsible for a non-symmetrical (nonreciprocal) response with the change of the orientation of the magnetic field. How the permittivity components change with respect to the magnetic field is described in Section 3.2.1. The modulation in the permittivity of the conductor elicits a change in the observed surface plasmon resonance. Figure 4.3.2 shows such change in the observed spectra with the application of the magnetic flux density $B_x = \pm 0.25$ T in transversal direction by small permanent magnets. The magnets were separated by a custom, 3d printed plastic holder. The semiconductor samples were directly between them. InSb

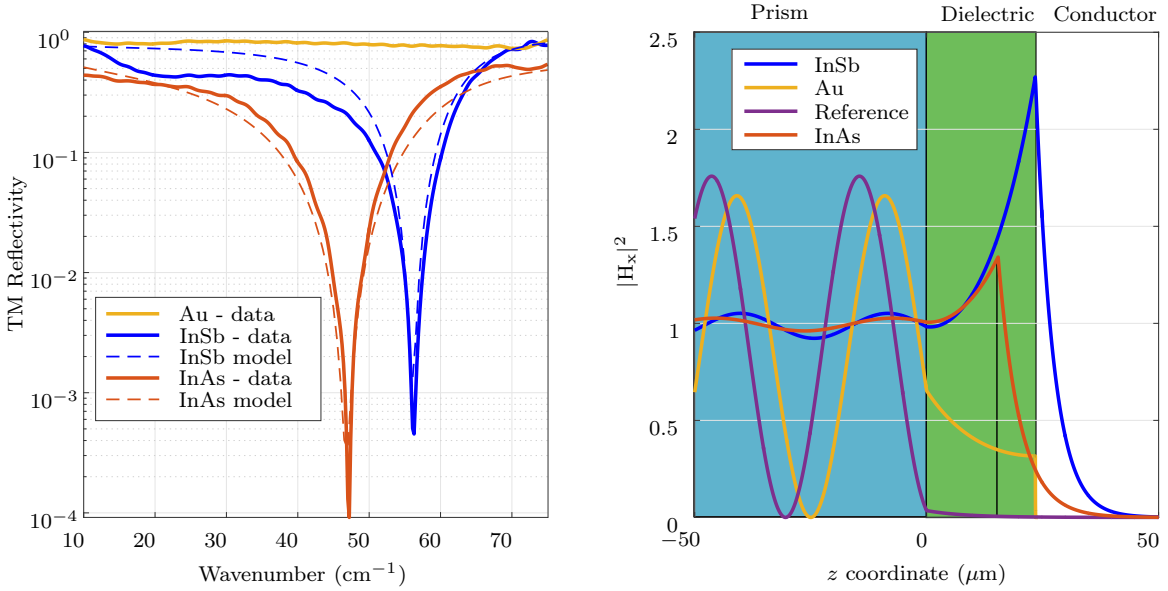

Figure 4.8: Left: Measured TM reflectivity of Otto configuration with different materials and data from a fitted model. The surface plasmon resonance is observed in InSb and InAs samples as sharp decrease in reflected intensity. Right: Calculated field profiles using the fitted model. The thickness of the dielectric for InAs is smaller due to different pressing strength of the manual anvil. The field profiles for semiconductors are calculated at the wavelengths of the resonances. For Au and reference, the wavelength was chosen as the same as for resonance in InSb.

and InAs exhibit strong shift in the frequency position of the plasmonic resonance. The field intensity profiles, calculated at the respective frequencies and normalized to the mean value in the prism, confirm the shift in SPR coupling. The shift, linearly proportional to the magnetic field for smaller fluxes ($< 0.5\ T$), is higher in InSb (160 GHz to each side) than for InAs (100 GHz) due to lower effective mass of carrier of InSb. The use of magnetic tuning of the surface plasmon resonance broadens the possible application of semiconductor based SPR THz sensor. First of all, the magnetic field can be used to fine-tune the resonance frequency. By changing the properties of the semiconductor with magnetic field we are able to find the strongest coupling of SPR for selected thickness and refractive index of the dielectric. This also means that we can scan the frequency based on our available magnetic field range and get a more complete data set of SPR coupling of different strengths and frequency positions. Lastly, using a modulated magnetic field would also permit the use of lock-in system, where the magnetic modulation would serve as a carrier wave. In a lock-in amplifier the detected signal is modulated by a known carrier wave, which drastically reduces noise in the system. The detected signal would be the surface plasmon resonance frequency position and strength, the modulation would be done by an electromagnet driven by alternating current. This type of sensor should bring enhanced sensitivity to the problems studied in the Terahertz regime - pharmaceuticals, explosives, biological samples. The control of the polarization of the surface plasmon resonance through the can prove very useful for studying samples with specific anisotropy or chirality.

The position and the strength of the surface plasmon resonance is intrinsically linked to the refractive index and thickness of the analyte as well as the complex permittivity of the conductor and the angle of incidence in the prism. Figure 4.3.2 shows the position of the strongest surface plasmon resonance based on the analyte refractive index for several cases of the angle of incidence and the magnetic field in InSb. Note that the same effect can be obtained by change of the refractive index of prism, because the tangential component of the prism propagation constant is $\nu_y = n_{\text{prism}} \sin\theta$, $n_{\text{Si}} = 3.4164$. The magnetic tuning offers excitation of SPR over range of frequencies, with fixed thickness - the strength of the resonance will vary, but the excitation remained possible as shown in Figure 4.3.2. Changing the angle of

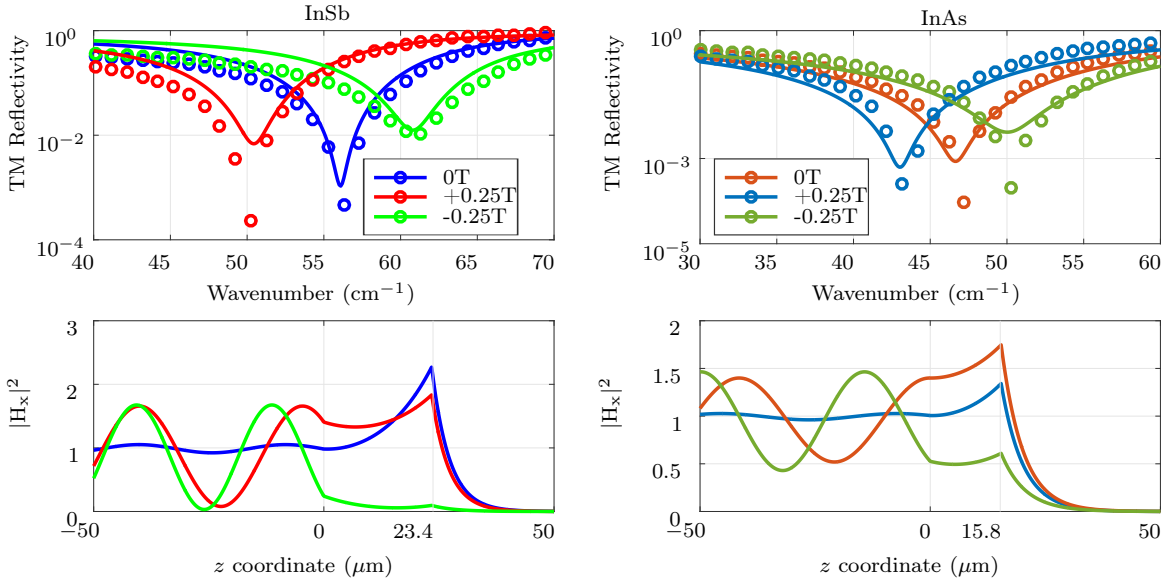

Figure 4.9: Top Left: Measurement and model of SPR on InSb at various external magnetic field in the transversal direction. Bottom Left: Calculated field profiles at respective wavelengths of the InSb SPR for each case, normalized to mean values in the prism. Top Right: Measurement and model of SPR on InAs at various external magnetic field in the transversal direction. Bottom Right: Calculated field profiles at respective wavelengths of the InAs SPR for each case, normalized to mean values in the prism.

incidence or the material of the prism can be used to tune the sensitivity to desired range of refractive index and thickness of the analyte. For example, having angle of incidence 25° confers much higher sensitivity to analyte with a refractive index around 1.3 than configuration with the angle of incidence of 35°, because of the steepest curve of the resonant frequency (Figure 4.3.2 right). The tradeoff is less sensitivity for samples with a higher refractive index, where the thickness would have to very high and the plasma resonance weaker. The actual configuration should be tailored to a need of the sensor.

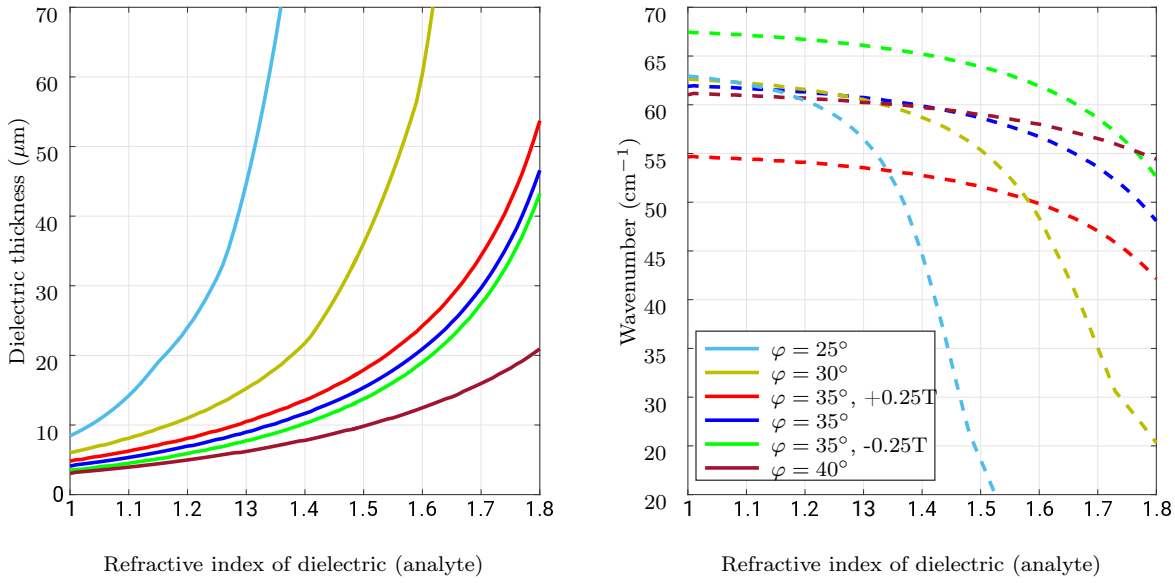

Figure 4.10: The calculated position of InSb SPR (TM reflectivity minimum) for different settings of the Otto configuration as a function of the refractive of the dielectric (analyte). For each refractive index and the angle of incidence, the thickness of the dielectric and resonance wavenumber are obtained simultaneously. For increasing angle of incidence (increasing propagation constant) the optimum is found for thinner dielectric layer (subplot left) and sensitivity to higher refractive indices (subplot right). For example, the highest sensitivity for analyte with refractive index 1.3-1.4 is with the angle of incidence of 25° and the resonances would be found in the range 45-55 cm^{-1}. Blue, red and green curves correspond to values of our measurement setup.

Theoretical Kretschmann configuration

While we have used the Otto configuration for experimental demonstration, it is also possible to excite THz SPR in the Kretschmann configuration. This could offer

more viable solution, similar to commerciall ATR systems. However, it requires the thickness of semiconductor in the range of several μm. Figure 4.3.2 shows such a case, with bulk of dielectric (n=1.625) on top of a layer of InSb on a Silicon prism with the angle of incidence of 35 degrees. The TM Reflectivity sweep of InSb thickness and wavelength shows an interesting property. Two distinct minima are observed, corresponding to plasmonic resonance. Their reflectivities are shown on the left and top right of Figure 4.3.2 with field profiles on the bottom right of Figure 4.3.2. First, a 1.05 μm thick InSb hold a surface plasmon at 6.2 cm^{-1} (186 GHz, 1.61 mm) in Zenneck regime, typical for longer wavelength. The dispersion of this type of surface plasmon is very close to the dispersion of light in the dielectric analyte. Majority of the energy is carried in the dielectric, with a very little confinement in the conductor, as it is shown in the field profile. On the other hand, with the thickness of 6.3 μm, the configurations holds a classic surface plasmon resonance at 65 cm^{-1} (1.95 THz, 153.8 μm), with confinement in both media. This shows that Kretschmann configuration is also valid for THz SPR sensor. The same principles shown for Otto configuration - tuning by magnetic field and changing sensitivity for different refractive index of the analyte, are also present here.

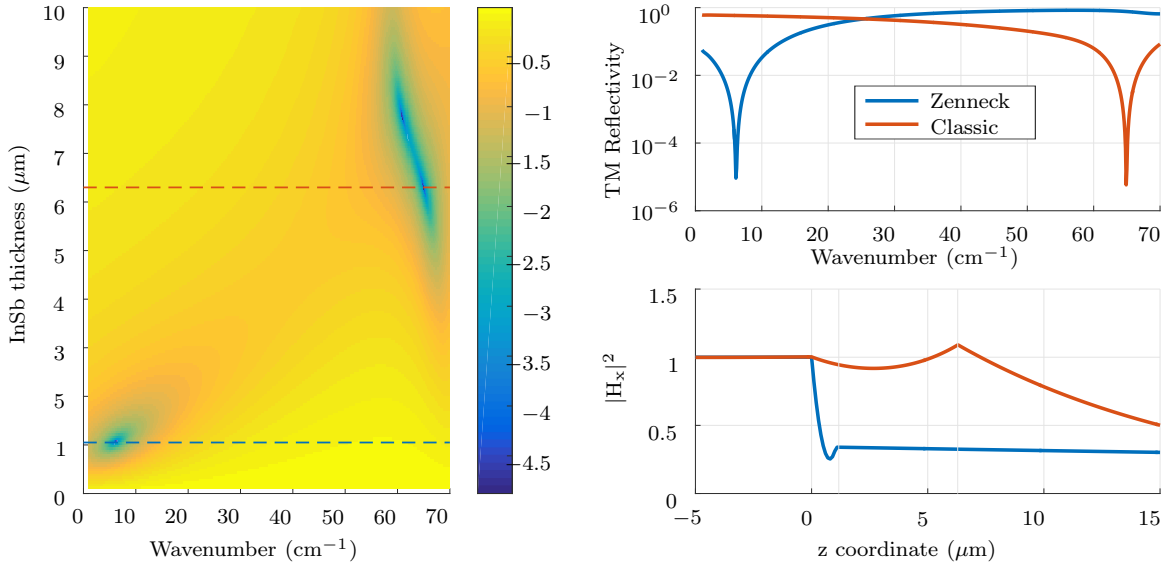

Figure 4.11: Left: Logarithmic contour of TM reflectivity in the Kretschmann configuration. Dielectric refractive index 1.625. Top right: TM reflectivity of 2 Kretschmann configurations, indicated by the dashed lines on the left. Bottom right: Field profile of those configurations, normalized to mean value in the prism.

4.3.3 Effective medium approximation as tuning mechanism

Section 3.4 showed that doping can significantly change the optical behavior of semiconductors in the far-infrared and terahertz range. So far we have only varied the doping levels over different samples, but in practice, different doping levels are the basis of electric and opto-electric semiconductor devices. The p-n junction is the necessary foundation for any diode, transistor, and derived components. This also means, that we can create gratings made from the single material, but the differentiation is done through the doping. The variation can be done in multiple ways. Either during manufacturing, or by photoexcitation [55]. The manufacturing process is straightforward, we increase or alternate different doping levels to create a permittivity profile of a desired shape. With photoexcitation, we create a desired pattern by illumination with light of energy above the bandgap of the semiconductor. Different intensities, created either with spatial light modulator or by interference pattern produce the gratings.

These gratings might find it use as diffraction gratings, variable mirrors or coupling elements. Here we discuss an accompanying idea - what happens when the period of the grating Λ is much smaller that the wavelength λ? This idea is particularly suited to the long wavelengths of terahertz waves, the interference patterns and spatial modulation of doping levels can be brought to the hundreds and tens of nanometers, while the used wavelength are on the order of hundred micrometers. For these long wavelengths, the subwavelength structure behaves as an effective medium, not diffractive, but anisotropic material with properties derived from the materials and geometry of the grating. By utilizing anisotropy instead of bulk modulation, we can define preferential directions of materials properties. With the knowledge of the formulas (Section 2.2.3) and by varying the materials and the geometry, we can create designer materials to suit our needs.

Validity of the quasistatic limit

Before applying the derived formulas of analytical effective media to any applications, we need to determine their correctness. They were derived in the limit when the period of the grating goes to zero. This is unattainable, so we need to determine for which ratio of wavelength and period is the effective medium approximation still valid. This

section answers that with this following example.

Consider a grating at selected period and calculate the measurable parameters using RCWA. In our case the measurable parameters are Mueller matrices at different angles of incidence. Then, using the Mueller matrices and optimization algorithm try to find an anisotropic tensor $\hat{\varepsilon}_{fit}$ that has the same optical response. Finally compare this tensor with analytically derived $\hat{\varepsilon}_{eff}$. When $\Lambda \ll \lambda$ (the quasistatic limit), the $\hat{\varepsilon}_{fit}$ should equal $\hat{\varepsilon}_{eff}$. This approach has been applied to lamellar gratings [76, 94], here we extend it to harmonic grating.

The example chosen for a demonstration is a 10 μm thick harmonic grating of undoped GaAs $\varepsilon_1 = 12.8039 + 0.0049i$ [137] and n-doped GaAs $\varepsilon_2 = -21.2832 + 31.5749i$ on n-doped GaAs (ε_2) substrate at 2 THz (150 μm). The model is studied at the angles of incidence from 0° to 80° with step 5 degrees and at periods from 1 μm to 90 μm with step 10 μm.

The effective medium theory for harmonic gratings predicts the effective medium tensor components as $\varepsilon_{xx,eff} = \varepsilon_{zz,eff} = -4.2392 + 15.7899i$ and $\varepsilon_{yy,eff} = 10.3656 + 19.4961i$. Figure 4.3.3 shows the fitted effective permittivity (real and imaginary parts) with the analytical effective permittivity from (2.122). From the figure, it is obvious that the limit does hold when the ratio Λ/λ is very small. This is according to our expectations and it is perfectly within the limits of manufacturing - a grating with the period of 1 μm is completely feasible. For larger grating periods, the effective medium theory quickly loses the its validity. The validity for grating made of alternating conductive and dielectric material is on the order of ones of percent. This is however the most complicated case, the difference between the permittivities is large. For gratings made only of dielectric materials, the validity goes roughly to 10 percent. [76] The response of the grating becomes too complicated to be described by a single tensor. We now know that the effective medium approximation is a valid model for harmonic semiconductor gratings.

Effective permittivity

In this section we look at how the effective permittivity behaves in different gratings and in different grating geometries. We will use the materials from the example in the previous section, undoped GaAs ($\varepsilon_\infty = 10.8,\ \omega_p = 3.1584 \times 10^8$ rad/s, $\tau = 3.238 \times$

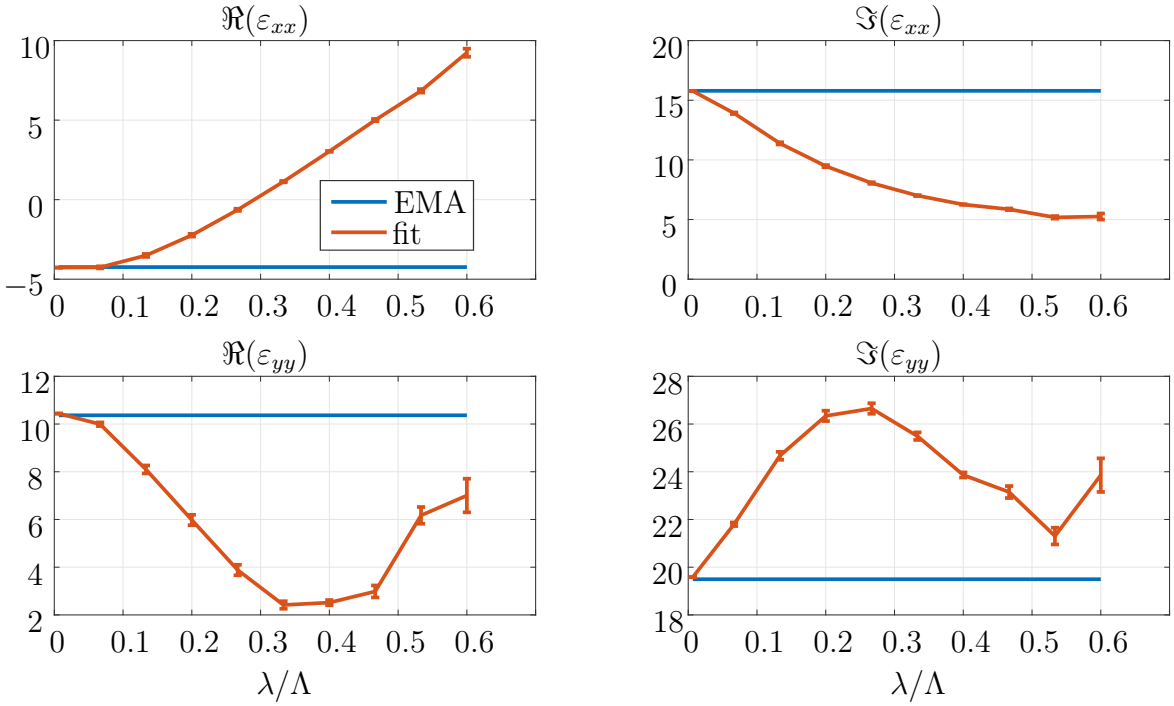

Figure 4.12: Testing of quasistatic limit using RCWA and EMA.

10−13 s), which behaves as a weakly absorbing dielectric and n-doped GaAs($\varepsilon_\infty = 10.8$, $\omega_p = 10^{14}$ rad/s, $\tau = 0.8592 \times 10^{-13}$ s). The n-doped is not a characterized sample, but an practical example. Its plasma frequency lies between our measured sample and the undoped one.

The main examples demonstrated here are the lamellar grating with various fill factors (fill factor times 100 is the percentage of material 2 in the grating) and harmonic grating. We can distinguish between the ordinary permittivity $\varepsilon_{xx,zz}$ and the extraordinary permittivity ε_{yy} perpendicular to the grating lamells. The ordinary permittivity is shown in Figures 4.13 and 4.14. Based on the fill factor of dielectric vs. conductive GaAs, the medium can be either optically conductive (negative real permittivity) or dielectric in the x or z direction, suggesting a strong possibility of modulation. The absorbtions, i.e. the imaginary part is high even for low fill factors. The harmonic gratings behave in the ordinary direction as lamellar one with the fill factor of 0.5.

The extraordinary part (Figures 4.15 and 4.16) shows an interesting behavior. Even small ratios of the dielectric materials move real part of permittivity to the

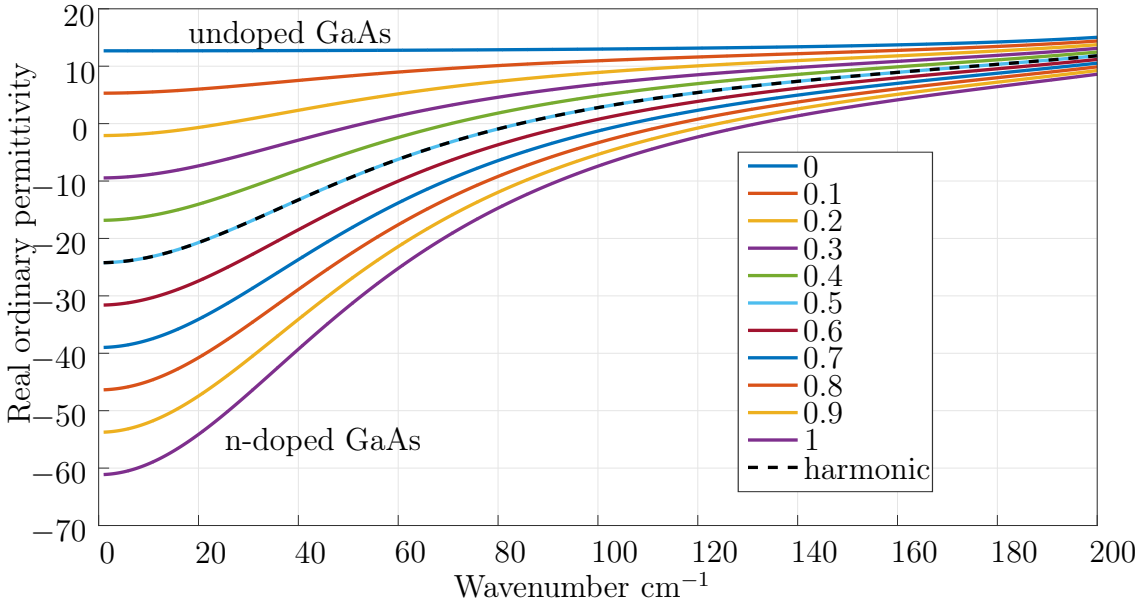

Figure 4.13: Real part of ordinary permittivity ($\varepsilon_{xx,zz}$) for gratings with various fill factors (legend).

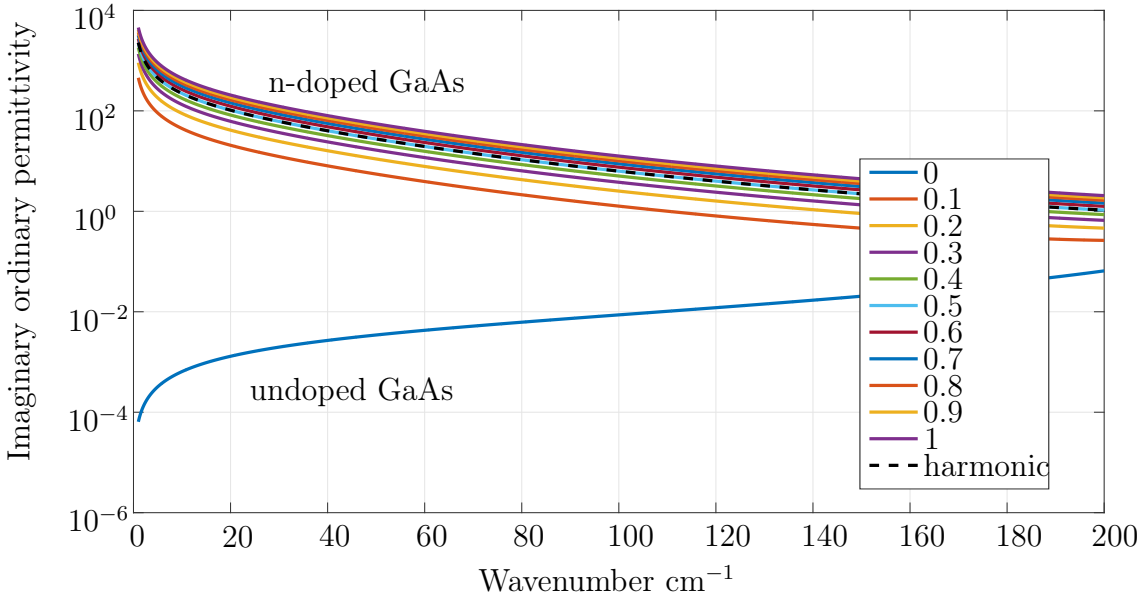

Figure 4.14: Imaginary part of ordinary permittivity ($\varepsilon_{xx,zz}$) for gratings with various fill factors (legend). Even small fill factor of highly absorbing material causes strong absorptions in the effective medium

positive values for longer wavelengths, while the plasmonic behavior is limited to a small frequency bandwidth, which unfortunately is compensated by an increase in absorbtions, so it doesn't really permits an effective use as modulation technique. This behavior can be understood microscopically, as the dielectric lamells restrict movement of electrons in one direction. This effect is different in the harmonic grating, since the permittivity perpendicular to the gratings changes continuously.

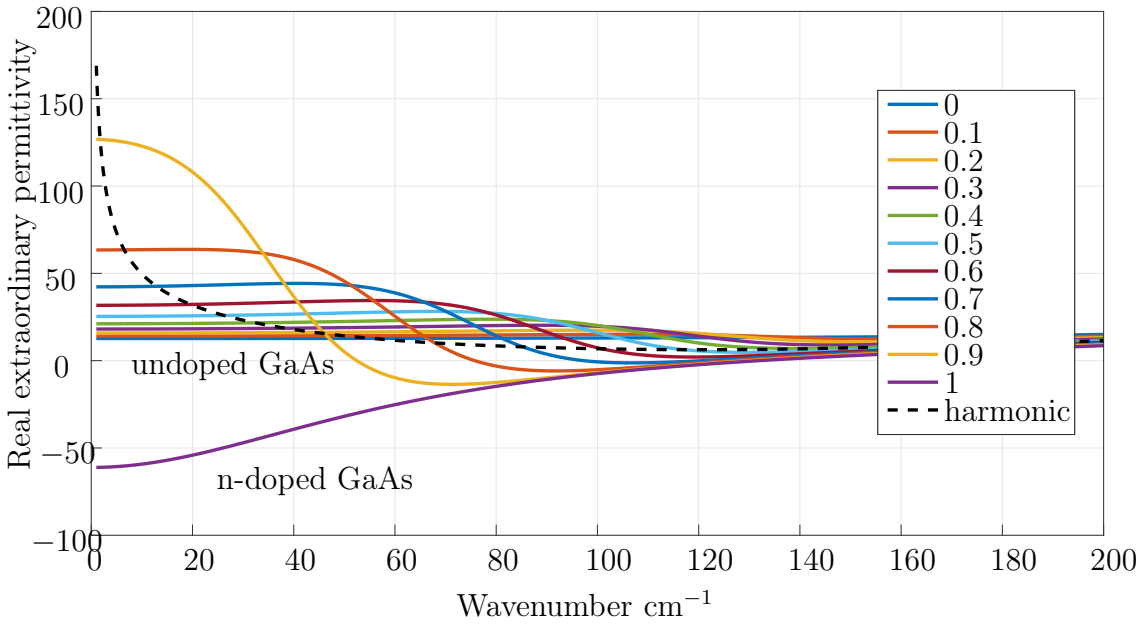

Figure 4.15: Real part of extraordinary permittivity (ε_{yy}) for gratings with various fill factors (legend).

To summarize these finding, both lamellar and harmonic effective gratings allow for a modulation of plasmonic behavior of semiconductors, based on different geometry for lamellar grating. The modulation using harmonic grating must be done through a different doping levels, which in the case of photoexcited interference pattern would be through the illumination intensity.

The effective way to modulate the plasmonic properties would be to put the lamells perpendicular to the x direction, along the y direction, this would make the plasmonic components ε_{yy} and ε_{zz} exhibit the same level of modulation. Such example is shown in the next section.

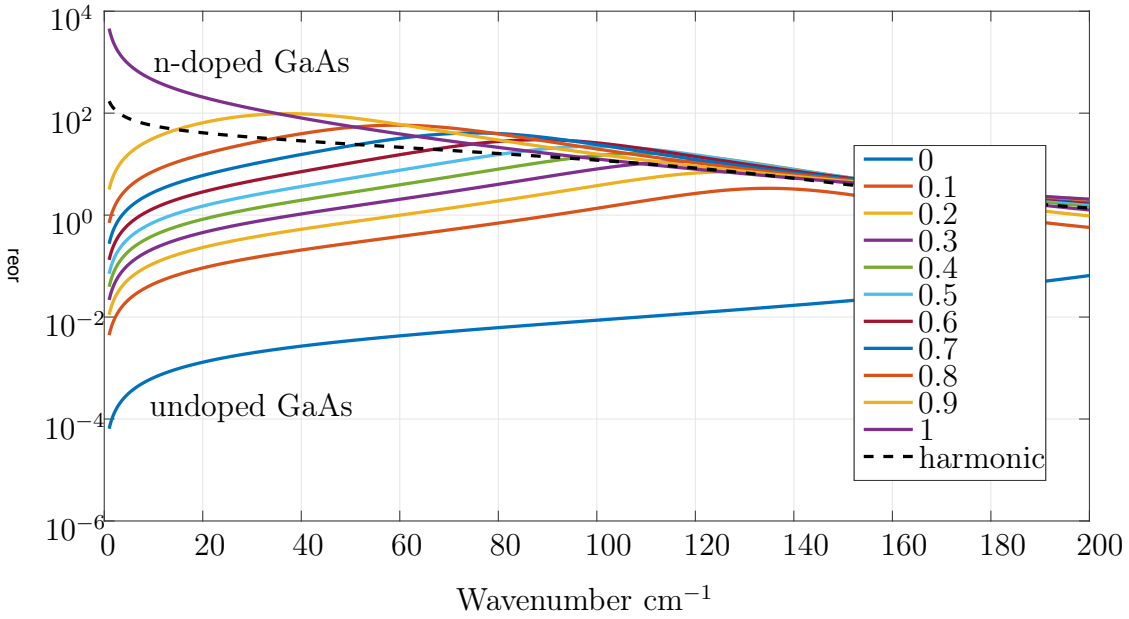

Figure 4.16: Imaginary part of extraordinary permittivity (ε_{yy}) for gratings with various fill factors (legend).

SPR at interface with grating media

We have shown both theoretically and experimentally in Section 4.3.2 that it is possible to excite a terahertz surface plasmon resonance in a tri-layer prism-dielectric-plasmonic semiconductor structure. We will use the same example to illustrate the tunability of surface plasmon resonance via subwavelength modulation of dielectric function.

The structure is the same as in the experimental demonstration. A Silicone prism, $\varepsilon_1 = 3.4164^2$, the angle of incidence of 35°, 8 μm thick dielectric film with the permittivity $\varepsilon_2 = 1.625^2$, and semiconductor grating made of undoped GaAs and n-doped GaAs with permittivity shown in the previous section. We will use the configuration with grating perpendicular to the x direction. The resulting TM reflectivity is shown in Figure 4.17. As with the experimental demonstration, the surface plasmon resonance is clearly present. The strength of the resonance is different for each of the fill factors/gratings, as it has been shown that the absolute SPR minimum requires different thickness of the dielectric. The frequency position of the SPR is clearly easily modulated using different fill factors.

Moreover, an interesting phenomena happens for fill factors lower than 0.2. By the

definition of surface plasmon, we shouldn't be able to excite a resonance here, since upon examining Figure 4.13, these configuration are only absorbing dielectric. There is no SPR visible for the undoped GaAs, but the mixtures of $f = 0.1$ and $f = 0.2$ still exhibit some form of resonance. Here, a more thorough analysis is needed.

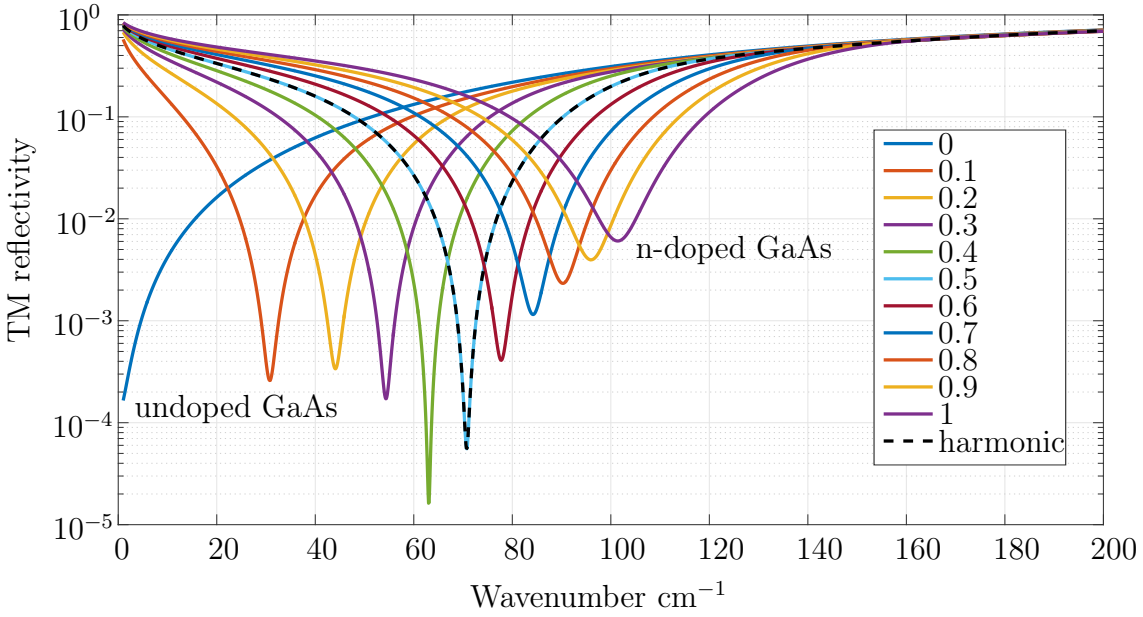

Figure 4.17: TM Reflectivity of effective media with various fill factors (legend) in Otto configuration.

For a surface plasmon resonance, both the field amplitude and the field intensity should be exponential decreasing from the interface, without any oscillations. To understand what happens in the structure at the resonances, we plot both the field (real part of H_x) and the field intensity ($|H_x|^2$). We do this for the case of $f = 0.1$, which has the resonance at 30.8 cm^{-1} and the permittivity is $\varepsilon_{eff} = 6.7924 + 11.8620i$ and the plasmonic case of $f = 0.5$ (also the harmonic grating), which is at 63.1 cm^{-1} with the permittivity $\varepsilon_{eff} = -5.2755 + 17.6923i$. The resulting field and intensities are plotted in Figure 4.3.3. The plasmonic case has both the field and the intensity exponentially decaying from the semiconductor/dielectric interface at $z = 8$ μm. The dielectric/dielectric interface also shows a decay in intensity, but the field has damped oscillating behavior, meaning that this is only a dielectric resonance, a type of anti-reflection coating. This behavior might finds its use, but it is not a surface plasmon. A dielectric/dielectric interface can only guide waves in a special anisotropic configuration of Dyakonov waves, which is not satisfied here.

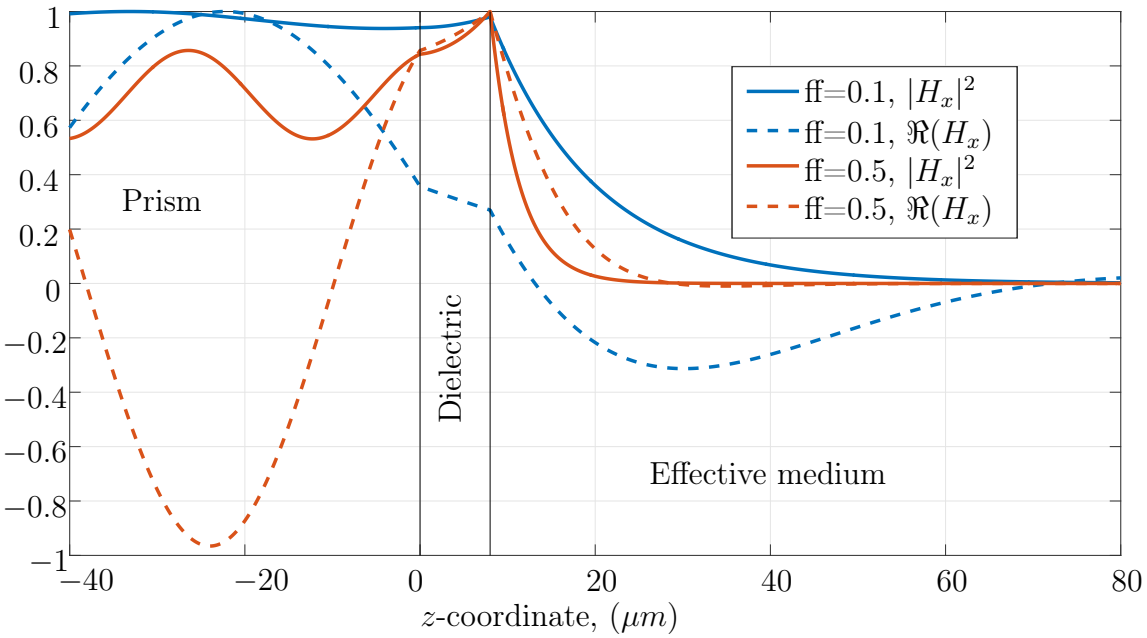

Figure 4.18: Field components and intensities for different wavelengths and fill factors. The field concentration on the interface of the dielectric and effective medium for fill factor 0.5 points to a surface plasmon polariton solution. For fill factor 0.1 the field in the effective medium has oscillating character - it is not a surface plasmon.

This example shows two aspects. First, the spatial doping modulation can create designer materials with desired properties and the effective medium theory well describes this behavior. Second any "solution" to a surface plasmon or guided wave must be carefully analyzed, since the analytic formulae or even observable quantities might show a viable solution (such as the Brewster angle), but the field analysis presents the true nature of the waves.

Chapter 5

Conclusion and Perspectives

In this thesis we have presented a complex picture of semiconductors as plasmonic materials mainly in the Terahertz range. We have characterized III-V semiconductor samples in broad spectral range (Section 3.4) to find their plasmonic properties (Section 3.2.1). Huge magneto-optical effect was measured and analyzed in InSb of various doping levels. The magneto-optical findings were confirmed using electric Hall effect measurement (Section 3.4.3). A spatial modulation of semiconductor properties using subwavelength gratings was explored (Section 2.2.3). Generation of surface magneto-plasmon resonance for Terahertz sensor application was experimentally demonstrated (Section 4.3.2). All these findings were supported by theoretical background in spectroscopy and optical properties (Chapter 3) of anisotropic multilayers and gratings (Chapter 2).

Semiconductors were shown as viable plasmonic materials for Terahertz and far-infrared applications. Their main advantage lies in easy modulation of plasmonic properties using doping, nano-patterning, and external magnetic field. Especially the magneto-optical modulation, joined with the sensor application in surface magneto-plasmon resonance seems most perspective. Such sensors with magnetic modulation would be able to scan broad range of Terahertz frequencies with high sensitivity or be used in a lock-in system, to decrease measurement noise.

I hope this thesis has provided the reader with both the fundamentals and the advanced topics in the fields of plasmonics, semiconductors, spectroscopy and optical modelling.

Appendix A

Publications and Awards

Publications

(I) **Jan Chochol**, Kamil Postava, Michael Čada, Mathias Vanwolleghem, Martin Mičica, Lukáš Halagačka, Jean-François Lampin, and Jaromír Pištora. Plasmonic behavior of III-v semiconductors in far-infrared and terahertz range. *Journal of the European Optical Society-Rapid Publications*, 13(1):13, 2017-05-01.

(II) **Jan Chochol**, Kamil Postava, Michael Čada, Mathias Vanwolleghem, Lukáš Halagačka, Jean-François Lampin, and Jaromír Pištora. Magneto-optical properties of InSb for terahertz applications. *AIP Advances*, 6(11):115021, 2016.

(III) Oleksandr Stepanenko, Tomáš Horák, **Jan Chochol**, Kamil Postava, Jean-François Lampin, and Mathias Vanwolleghem. Compact mid-IR isolator using nonreciprocal magnetoplasmonic InSb mirror. In *2016 41st International Conference on Infrared, Millimeter, and Terahertz waves (IRMMW-THz)*. IEEE, sep 2016.

(IV) **Jan Chochol**, Kamil Postava, Michael Čada, and Jaromír Pištora. Experimental demonstration of magnetoplasmon polariton at insb(inas)/dielectric interface for terahertz sensor application. *Scientific Reports*, Accepted, 2017.

(V) Kamil Postava, **Jan Chochol**, Jaroslav Hamrle, and Jaromír Pištora. Effective medium approximation of anisotropic grating with sinusoidal modulation of optical parameters. In preparation. 2017.

Conference presentations

(I) 2016, Jan Chochol, Kamil Postava, Michael Čada, and Jaromír Pištora. *Free carrier magneto-optical effect of InSb in the terahertz range*, Silesian Cross-Border Workshop on Applied physics, Czech Republic, Oral presentation

(II) 2016, Jan Chochol, Kamil Postava, Michael Čada, and Jaromír Pištora. *Reflection measurement in THz and far-infrared range of magnetically induced anisotropy in InSb*, 5th EOS Topical Meeting on Terahertz Science & Technology, Hungary, Oral presentation

(III) 2016, Jan Chochol, Kamil Postava, Michael Čada, and Jaromír Pištora. *Terahertz magneto-optical activity of III–V semiconductors*, DPG - Annual meeting, Germany, Oral presentation

(IV) 2016, Jan Chochol, Kamil Postava, Michael Čada, and Jaromír Pištora. *Plasmons and magneto-optics on semiconductors*, ASPIRE Annual Conference, Canada, Oral presentation

(V) 2015, Jan Chochol, Kamil Postava, Michael Čada, and Jaromír Pištora. *Grating assisted semiconductor plasmonic waveguides* Photonics North, Canada, Poster

(VI) 2015, Jan Chochol, Kamil Postava, and Michael Čada. *Semiconductor grating waveguides*, ECE Dept. Graduate Conference, Canada, Oral presentation

(VII) 2013, Jan Chochol, Kamil Postava, Jaroslav Hamrle, and Jaromír Pištora. *Modelling of optical responses from layers with harmonic modulation of dielectric function using RCWA*, JEMS, Greece, Poster

Awards

- 2016, *Oral Presentation*, ASPIRE Annual Conference, Halifax, **1st prize** for best presentation, Plasmons and magneto-optics on semiconductors
- 2015, *Oral Presentation*, ECE Dept. Graduate Conference, Halifax, **2nd prize** for best presentation, Semiconductor grating waveguides

Appendix B

Copyright permissions

Creative Commons Licensing Terms

Journal : AIP Advances
Manuscript # : 2016-2624-TR
Title : Magneto-optical properties of InSb for terahertz applications
Authors : Jan Chochol, Kamil Postava, Michael Cada, Mathias Vanwolleghem, Lukáš Halagačka, Jean François Lampin, and Jaromír Pištora
Agreement Date : 31-Oct-2016 09:09 GMT

Please read the Creative Commons Licensing Terms and enter the signature in the text box below to indicate your consent to that Agreement.

Creative Commons Licensing Terms

Authors retain copyright to their *AIP Advances* articles and agree to apply the Creative Commons Attribution 4.0 International (CC BY 4.0) License (http://creativecommons.org/licenses/by/4.0/) to their work. Authors also grant AIP Publishing a license to publish the article and to be acknowledged as the publisher of record (original publisher) of the work. In granting this license to AIP Publishing, the authors represent and warrant that the article is original and does not infringe any copyright or violate any other right of any third parties.

Under the terms of this license, no permission is required to copy, distribute, transmit, or adapt the article content, provided proper attribution is given to the authors as specified.It is imperative that any material used from other sources, including but not limited to figures, tables, and images, and which has been previously copyrighted, be cleared for reuse under the terms of the Creative Commons Attribution 4.0 International (CC BY 4.0) License (http://creativecommons.org/licenses/by/4.0/). Express permission must be obtained from the copyright holder for inclusion of any such materials in an *AIP Advances* article.

You may direct any questions to rights@aip.org.

Please type your FULL First and Last Names (no initials) in the boxes to indicate your consent to the agreement.

First Name Jan Last Name Chochol

☑ I understand and agree to license my work under the Creative Commons Attribution 4.0 International (CC BY 4.0) License, and I have obtained all necessary permissions for inclusion of any previously copyrighted material under the same or similar terms.

local_p_id: 891524
time: 1477904956
ip address: 158.196.16.108

Bibliography

[1] A. D. Rakić, A. B. Djurišić, J. M. Elazar, and M. L. Majewski, "Optical properties of metallic films for vertical-cavity optoelectronic devices," Appl. Opt. **37**, 5271–5283 (1998).

[2] I. F. Akyildiz, J. M. Jornet, and C. Han, "Terahertz band: Next frontier for wireless communications," Phy. Com. **12**, 16–32 (2014).

[3] A. J. Seeds, H. Shams, M. J. Fice, and C. C. Renaud, "TeraHertz photonics for wireless communications," J. of Lightwave Technol. **33**, 579–587 (2015).

[4] S. A. Maier, *Plasmonics: fundamentals and applications* (Springer, 2007).

[5] H. Raether, *Surface Plasmons on Smooth and Rough Surfaces and on Gratings*, vol. 111 of *Springer Tracts in Modern Physics* (Springer Berlin Heidelberg, 1988).

[6] H. A. Atwater, "The promise of plasmonics," Sci. Am **296**, 56–63.

[7] S. Hayashi and T. Okamoto, "Plasmonics: visit the past to know the future," J. Phys. D-Applied Physics **45**, 433001 (2012).

[8] J. Homola, S. S. Yee, and G. Gauglitz, "Surface plasmon resonance sensors: review," Sensor. Actuat. B-Chem. **54**, 3–15 (1999).

[9] P. Berini, "Long-range surface plasmon polaritons," Adv. Opt. **1**, 484 (2009).

[10] N. Zhou, X. Xu, A. T. Hammack, B. C. Stipe, K. Gao, W. Scholz, and E. C. Gage, "Plasmonic near-field transducer for heat-assisted magnetic recording," Nanophotonics **3** (2014).

[11] C. Chen and P. Berini, "Grating couplers for broadside input and output coupling of long-range surface plasmons," Opt. Express **18**, 8006–8018 (2010).

[12] T. J. Heggie, D. A. Naylor, B. G. Gom, E. Bordatchev, and M. G. Trimboli, "Enhanced terahertz transmission through bullseye plasmonics lenses fabricated using micromilling techniques," Plasmonics (2016).

[13] M. Kauranen and A. V. Zayats, "Nonlinear plasmonics," Nat. Photonics **6**, 737–748 (2012).

[14] D. C. Marinica, M. Zapata, P. Nordlander, A. K. Kazansky, P. M. Echenique, J. Aizpurua, and A. G. Borisov, "Active quantum plasmonics," Sci. Adv. **1**, e1501095 (2015).

[15] W. L. Barnes, A. Dereux, and T. W. Ebbesen, "Surface plasmon subwavelength optics," Nature **424**, 824–830 (2003).

[16] T. Nagatsuma, G. Ducournau, and C. C. Renaud, "Advances in terahertz communications accelerated by photonics," Nat. Photonics **10**, 371–379 (2016).

[17] J. F. O'Hara, W. Withayachumnankul, and I. Al-Naib, "A review on thin-film sensing with terahertz waves," J. Infrared Millim. Te. **33**, 245–291 (2012).

[18] X. Yang, X. Zhao, K. Yang, Y. Liu, Y. Liu, W. Fu, and Y. Luo, "Biomedical applications of terahertz spectroscopy and imaging," Trends in biotechnology **34**, 810 – 824 (2016).

[19] H.-B. Liu, H. Zhong, N. Karpowicz, Y. Chen, and X.-C. Zhang, "Terahertz spectroscopy and imaging for defense and security applications," Proc. IEEE **95**, 1514–1527 (2007-08).

[20] E. Pickwell and V. P. Wallace, "Biomedical applications of terahertz technology," J. Phys. D-Applied Physics **39**, R301–R310 (2006).

[21] D. M. Mittleman, R. H. Jacobsen, R. Neelamani, R. G. Baraniuk, and M. C. Nuss, "Gas sensing using terahertz time-domain spectroscopy," Appl. Phys B-Lasers and Optics **67**, 379–390 (1998).

[22] M. Tonouchi, "Cutting-edge terahertz technology," Nat. Photonics **1**, 97–105 (2007).

[23] T.-I. Jeon and D. Grischkowsky, "THz zenneck surface wave (THz surface plasmon) propagation on a metal sheet," Appl. Phys. Letters **88**, 061113 (2006).

[24] D. G. Cooke and P. U. Jepsen, "Optical modulation of terahertz pulses in a parallel plate waveguide," Opt. Express **16**, 15123–15129 (2008).

[25] J. Gómez Rivas, M. Kuttge, H. Kurz, P. Haring Bolivar, and J. A. Sánchez-Gil, "Low-frequency active surface plasmon optics on semiconductors," Appl. Phys. Lett. **88**, 082106 (2006).

[26] M. Rahm, J.-S. Li, and W. J. Padilla, "THz wave modulators: A brief review on different modulation techniques," J. Infrared Millim. Te. **34**, 1–27 (2013).

[27] P. Kühne, C. M. Herzinger, M. Schubert, J. A. Woollam, and T. Hofmann, "Invited Article: An integrated mid-infrared, far-infrared, and terahertz optical Hall effect instrument," Rev. Sci. Instrum. **85**, 071301 (2014).

[28] D. M. Bolle, A. V. Nurmikko, and G. S. Heller, "Application of surface magnetoplasmons on semiconductor substrates," Tech. rep., Brown Univ., Providence, RI. (1983).

[29] B. Hu, Q. J. Wang, and Y. Zhang, "Slowing down terahertz waves with tunable group velocities in a broad frequency range by surface magneto plasmons," Opt. Express **20**, 10071 (2012).

[30] E. D. Palik and J. K. Furdyna, "Infrared and microwave magnetoplasma effects in semiconductors," Rep. Prog. Phys. **33**, 1193 (1970).

[31] M. Schubert, T. Hofmann, and C. M. Herzinger, "Generalized far-infrared magneto-optic ellipsometry for semiconductor layer structures: determination of free-carrier effective-mass, mobility, and concentration parameters in n-type GaAs," J. Opt. Soc. Am. A **20**, 347–356 (2003).

[32] M. Schubert, T. Hofmann, and J. Sik, "Long-wavelength interface modes in semiconductor layer structures," Phys. Rev. B **71** (2005).

[33] T. Hofmann, C. M. Herzinger, C. Krahmer, K. Streubel, and M. Schubert, "The optical hall effect," physica status solidi (a) **205**, 779–783 (2008).

[34] D. M. Mittleman, J. Cunningham, M. C. Nuss, and M. Geva, "Noncontact semiconductor wafer characterization with the terahertz Hall effect," Appl. Phys. Lett. **71**, 16 (1997).

[35] F. Kadlec, C. Kadlec, and P. Kuzel, "Contrast in terahertz conductivity of phase-change materials," Solid State Commun. **152**, 852–855 (2012).

[36] P. Kužel and H. Němec, "Terahertz conductivity in nanoscaled systems: effective medium theory aspects," Journal of Physics D: Applied Physics **47**, 374005 (2014).

[37] T.-I. Jeon and D. Grischkowsky, "Characterization of optically dense, doped semiconductors by reflection THz time domain spectroscopy," Appl. Phys. Lett. **72**, 3032 (1998).

[38] D. Grischkowsky, S. Keiding, M. Van Exter, and C. Fattinger, "Far-infrared time-domain spectroscopy with terahertz beams of dielectrics and semiconductors," J. Opt. Soc. Am. B **7**, 2006–2015 (1990).

[39] Y. Ino, R. Shimano, Y. Svirko, and M. Kuwata-Gonokami, "Terahertz time domain magneto-optical ellipsometry in reflection geometry," Phys. Rev. B **70** (2004).

[40] T. N. Stanislavchuk, T. D. Kang, P. D. Rogers, E. C. Standard, R. Basistyy, A. M. Kotelyanskii, G. Nita, T. Zhou, G. L. Carr, M. Kotelyanskii, and A. A. Sirenko, "Synchrotron radiation-based far-infrared spectroscopic ellipsometer with full mueller-matrix capability," Rev. Sci. Instrum. **84**, 023901 (2013).

[41] C. Kittel, *Introduction to Solid State Physics* (Wiley, 2004).

[42] B. Lax, J. G. Mavroides, H. J. Zeiger, and R. J. Keyes, "Cyclotron resonance in Indium Antimonide at high magnetic fields," Phys. Rev. **122**, 31 (1961).

[43] E. D. Palik, R. Kaplan, R. W. Gammon, H. Kaplan, R. F. Wallis, and J. J. Quinn, "Coupled surface magnetoplasmon-optic-phonon polariton modes on InSb," Phys. Rev. B **13**, 2497 (1976).

[44] W. G. Spitzer and H. Y. Fan, "Determination of optical constants and carrier effective mass of semiconductors," Phys. Rev. **106**, 882 (1957).

[45] M. E. Brodwin and R. J. Vernon, "Free-carrier magneto-microwave Kerr effect in semiconductors," Phys. Rev. **140**, A1390 (1965).

[46] S. B. Singh, R. M. Mehra, and P. C. Kothari, "Magneto-microwave Kerr effect in n-type Indium Antimonide," J. Phys. D-Applied Physics **8**, L96 (1975).

[47] C. Pidgeon, "Free Carrier Optical Properties of Semiconductors," in "Optical properties of solids," , M. Balkanski and T. Moss, eds. (North-Holland Pub. Co., Amsterdam, 1980), Handbook on semiconductors, chap. 5, pp. 223–328.

[48] M. S. Kushwaha, "Plasmons and magnetoplasmons in semiconductor heterostructures," Surf. Sci. Rep. **41**, 1–416 (2001).

[49] H. Nguyen, J. Park, S. Kang, and M. Kim, "Surface plasmon resonance: A versatile technique for biosensor applications," Sensors **15**, 10481–10510 (2015-05-05).

[50] G. V. Naik, V. M. Shalaev, and A. Boltasseva, "Alternative plasmonic materials: Beyond Gold and Silver," Adv. Mater. **25**, 3264–3294 (2013).

[51] T. Srivastava, A. Purkayastha, and R. Jha, "Graphene based surface plasmon resonance gas sensor for terahertz," Opt. Quant. Electron. **48** (2016).

[52] Y. Huang, S. Zhong, H. Yao, and D. Cui, "Tunable ultrasensitive terahertz sensing based on surface plasmon polariton of doped monolayer graphene," physica status solidi (a) **214**, 1600550 (2016).

[53] F. Miyamaru, M. W. Takeda, T. Suzuki, and C. Otani, "Highly sensitive surface plasmon terahertz imaging with planar plasmonic crystals," Opt. Express **15**, 14804–14809 (2007).

[54] J. Shibayama, K. Shimizu, J. Yamauchi, and H. Nakano, "Surface plasmon resonance waveguide sensor in the terahertz regime," J. Lightwave Technol. **34**, 2518–2525 (2016).

[55] T. P. Steinbusch, H. K. Tyagi, M. Schaafsma, G. Georgiou, and J. Gómez Rivas, "Active terahertz beam steering by photo-generated graded index gratings in thin semiconductor films," Opt. Express **22**, 26559 (2014-11-03).

[56] E. Hendry, F. J. Garcia-Vidal, L. Martin-Moreno, J. G. Rivas, M. Bonn, A. P. Hibbins, and M. J. Lockyear, "Optical control over surface-plasmon-polariton-assisted THz transmission through a slit aperture," Phys. Rev. Letters **100** (2008).

[57] T. H. Isaac, J. Gómez Rivas, and E. Hendry, "Optical control over transmission of terahertz radiation through arrays of subwavelength holes of varying size," Phys. Rev. B **80** (2009-11-25).

[58] G. Georgiou, H. K. Tyagi, P. Mulder, G. J. Bauhuis, J. J. Schermer, and J. G. Rivas, "Photo-generated THz antennas," Scientific Reports **4** (2014).

[59] H. K. Tyagi and J. Gómez Rivas, "Photo-generated THz plasmonic waveguides," J. Opt. **16**, 094011 (2014-09-01).

[60] V. V. Kruglyak, S. O. Demokritov, and D. Grundler, "Magnonics," J. Phys. D-Applied Physics **43**, 264001 (2010).

[61] E. N. Montbach and P. J. Bos, "Control of dispersion in form birefringent-based holographic optical retarders," Opt. Engineering **44**, 124001–1–6 (2005).

[62] R. L. Sutherland, V. P. Tondiglia, L. V. Natarajan, and T. J. Bunning, "Phenomenological model of anisotropic volume hologram formation in liquid-crystal-photopolymer mixtures," J. Appl. Phys. **96**, 951–965 (2004).

[63] V. A. Stoica, Y.-M. Sheu, D. A. Reis, and R. Clarke, "Wideband detection of transient solid-state dynamics using ultrafast fiber lasers and asynchronous optical sampling," Opti Express **16**, 2322–2335 (2008).

[64] R. Liu, G. D. Sanders, C. J. Stanton, C. S. Kim, J. S. Yahng, Y. D. Jho, K. J. Yee, E. Oh, and D. S. Kim, "Femtosecond pump-probe spectroscopy of propagating coherent acoustic phonons in $In_xGa_{1-x}N$-GaN heterostructures," Phys. Rev. B **72**, 195335 (2005).

[65] M. Maldovan, "Sound and heat revolutions in phononics," Nature **503**, 209ÂÂĄÂš217 (2013).

[66] T. P. M. Alegre, A. Safavi-Naeini, M. Winger, and O. Painter, "Quasi-two-dimensional optomechanical crystals with a complete phononicbandgap," Opt. Express **19**, 5658–5669 (2011).

[67] M. Neviere and E. Popov, *Light propagation in periodic media, Differential theory and design* (Marcel Dekker, Inc., New York, 2003).

[68] G. Bao, L. Cowsar, and W. Masters, eds., *Mathematical Modeling in Optical Science* (SIAM, Philadelphia, 1987).

[69] A. Sihvola, *Electromagnetic Mixing Formulas and Applications*, IEE Publication Series (Institution of Engineering and Technology (IET), 2000).

[70] D. E. Aspnes, "Local-field effects and effective-medium theory: A microscopic perspective," Am. J. of Phys. **50**, 704–709 (1982).

[71] W. I. Bragg and A. B. Pippard, "The form birefringence of macromolecules," Acta Cryst. **6**, 865–867 (1953).

[72] M. Abe, "Derivation of nondiagonal effective dielectric-permeability tensors for magnetized granular composites," Phys. Rev. B **53**, 7065–7075 (1996).

[73] H. Kikuta, Y. Ohira, H. Kubo, and K. Iwata, "Effective medium theory of two-dimensional subwavelength gratings in the non-quasi-static limit," J. Opt. Soc. Am. A **15**, 1577–1585 (1998).

[74] H. Kikuta, H. Yoshida, and K. Iwata, "Ability and limitation of effective medium theory for subwavelength gratings," Opt. Rev. **2**, 92ÂÂĄÂš–99 (1995).

[75] P. Lalanne and J. Hugonin, "High-order effective-medium theory of subwavelength gratings in classical mounting: application to volume holograms," J. Opt. Soc. Am. A **15**, 1843–1851 (1998).

[76] M. Foldyna, R. Ossikovski, A. De Martino, B. Drevillon, K. Postava, D. Ciprian, J. Pistora, and K. Watanabe, "Effective medium approximation of anisotropic lamellar nanogratings based on fourier factorization," Opt. Express **14**, 3114–3128 (2006).

[77] A. Emoto, M. Nishi, M. Okada, S. Manabe, S. Matsui, N. Kawatsuki, and H. Ono, "Form birefringence in intrinsic birefringent media possessing a subwavelength structure," Appl. Opt. **49**, 4355–4361 (2010).

[78] G. Cambell and R. K. Kostuk, "Effective-medium theory of sinusiodally modulated volume holograms," J. Opt. Soc. Am. A **12**, 1113–1117 (1995).

[79] J. Chochol, K. Postava, M. Cada, M. Vanwolleghem, M. Micica, L. Halagacka, J.-F. Lampin, and J. Pistora, "Plasmonic behavior of III-V semiconductors in far-infrared and terahertz range," J. Europ. Opt. Soc.-Rapid Publ. **13**, 13 (2017).

[80] J. Chochol, K. Postava, M. Cada, M. Vanwolleghem, L. Halagacka, J.-F. Lampin, and J. Pistora, "Magneto-optical properties of InSb for terahertz applications," AIP Advances **6**, 115021 (2016).

[81] O. Stepanenko, T. Horak, J. Chochol, K. Postava, J.-F. Lampin, and M. Vanwolleghem, "Compact mid-IR isolator using nonreciprocal magnetoplasmonic InSb mirror," in "2016 41st International Conference on Infrared, Millimeter, and Terahertz waves (IRMMW-THz)," (IEEE, 2016).

[82] J. Chochol, K. Postava, M. Cada, and J. Pistora, "Experimental demonstration of magnetoplasmon polariton at InSb(InAs)/dielectric interface for terahertz sensor application," Scientific Reports (Accepted 2017).

[83] K. Postava, J. Chochol, J. Hamrle, and J. Pistora, "Effective medium approximation of anisotropic grating with sinusoidal modulation of optical parameters," (In preparation 2017).

[84] D. W. Berreman, "Optics in stratified and anisotropic media: 4×4 -matrix formulation," J. Opt. Soc. Am. **62**, 502–510 (1972).

[85] B. E. Saleh, M. C. Teich, and B. E. Saleh, *Fundamentals of photonics*, vol. 22 (Wiley New York, 1991).

[86] P. Yeh, "Optics of anisotropic layered media: A new 4×4 matrix algebra," Surf. Sci. pp. 41–53 (1980).

[87] S. Visnovsky, *Optics in Magnetic Multilayers and Nanostructures (Optical Science and Engineering)* (CRC Press, 2006).

[88] M. Born and E. Wolf, *Principles of Optics* (Pergamon, Oxford, 1975), 5th ed.

[89] L. Li, "Formulation and comparison of two recursive matrix algorithms for modeling layered diffraction gratings," J. Opt. Soc. Am. A **13**, 1024–1035 (1996).

[90] L. Li, "Use of fourier series in the analysis of discontinuous periodic structures," J. Opt. Soc. Am. A **13**, 1870–1876 (1996).

[91] W. Stork, N. Streibl, H. Haidner, and P. Kipfer, "Artificial distributed-index media fabricated by zero-order gratings," Opt. Lett. **16**, 1921–1923 (1991).

[92] S. M. Rytov, "Electromagnetic properties of a finely stratified medium," Sov. Phys. JETP **2**, 466–475 (1956).

[93] P. Lalanne and D. Lemercier-Lalanne, "Depth dependence of the effective properties of subwavelength gratings," J. Opt. Soc. Am. A **14**, 450–458 (1997).

[94] M. Foldyna, K. Postava, R. Ossikovski, A. De Martino, and E. Garcia-Caurel, "Effective spectral optical functions of lamellar nanogratings," J. Europ. Opt. Soc.-Rapid Publ. **1**, 06015 (2006).

[95] V. Kruglyak and R. Hicken, "Magnonics: Experiment to prove the concept," J. Magn. Magn. Mater. **306**, 191–194 (2006).

[96] M. Fox, *Optical Properties of Solids (Oxford Master Series in Physics)* (Oxford University Press, 2010).

[97] P. Yu and M. Cardona, *Fundamentals of Semiconductor: Physics and Materials Properties* (Springer Berlin Heidelberg, 2013).

[98] M. A. Ordal, L. L. Long, R. J. Bell, S. E. Bell, R. R. Bell, R. W. Alexander, and C. A. Ward, "Optical properties of the metals Al, Co, Cu, Au, Fe, Pb, Ni, Pd, Pt, Ag, Ti, and W in the infrared and far infrared," Appl. Opt. **22**, 1099 (1983).

[99] M. A. Ordal, R. J. Bell, R. W. Alexander, L. L. Long, and M. R. Querry, "Optical properties of fourteen metals in the infrared and far infrared: Al, Co, Cu, Au, Fe, Pb, Mo, Ni, Pd, Pt, Ag, Ti, V, and W," Appl. Opt. **24**, 4493 (1985).

[100] M. Cada, D. Blazek, J. Pistora, K. Postava, and P. Siroky, "Theoretical and experimental study of plasmonic effects in heavily doped Gallium Arsenide and Indium Phosphide," Opt. Mater. Express **5**, 340 (2015).

[101] L. Van der Pauw, "A method of measuring specific resistivity and Hall effect of discs of arbitrary shape," Philips Res. Rep. **13**, 1–9 (1958).

[102] R. W. Collins and J. Koh, "Dual rotating-compensator multichannel ellipsometer: instrument design for real-time Mueller matrix spectroscopy of surfaces and films," J. Opt. Soc. Am. A **16**, 1997–2006 (1999).

[103] H. Rippel and R. Jaacks, "Performance data of the double pendulum interferometer," Microchim. Acta **95**, 303–306 (1988).

[104] P. Griffiths, J. De Haseth, and J. Winefordner, *Fourier Transform Infrared Spectrometry*, Chemical Analysis: A Series of Monographs on Analytical Chemistry and Its Applications (Wiley, 2007).

[105] Y. Lee, *Principles of Terahertz Science and Technology*, Lecture Notes in Physics (Springer US, 2009).

[106] X. Zhang and J. Xu, *Introduction to THz Wave Photonics*, SpringerLink : Bücher (Springer US, 2009).

[107] T. Seifert, S. Jaiswal, U. Martens, J. Hannegan, L. Braun, P. Maldonado, F. Freimuth, A. Kronenberg, J. Henrizi, I. Radu, E. Beaurepaire, Y. Mokrousov, P. M. Oppeneer, M. Jourdan, G. Jakob, D. Turchinovich, L. M. Hayden, M. Wolf, M. MĂźnzenberg, M. KlĂ¤ui, and T. Kampfrath, "Efficient metallic spintronic emitters of ultrabroadband terahertz radiation," Nat. Photonics **10**, 483–488 (2016).

[108] H. Jamshidi and T. J. Parker, "The far infrared optical properties of InP at 6 and 300 K," Int. J. Infrared Millimeter Waves **4**, 1037–1044 (1983).

[109] W. Zawadzki, "Electron transport phenomena in small-gap semiconductors," Adv. Phys. **23**, 435–522 (1974).

[110] R. T. Holm, "Indium Antimonide (InSb)," in "Handbook of Optical Constants of Solids," , E. D. Palik, ed. (Academic Press, Burlington, 1997), pp. 491 – 502.

[111] J. Gómez Rivas, J. A. Sanchez-Gil, M. Kuttge, P. Haring Bolivar, and H. Kurz, "Optically switchable mirrors for surface plasmon polaritons propagating on semiconductor surfaces," Phys. Rev. B **74** (2006).

[112] E. D. Palik, S. Teitler, and R. F. Wallis, "Free Carrier Cyclotron Resonance, Faraday Rotation, and Voigt Double Refraction in Compound Semiconductors," J. Appl. Phys. **32**, 2132 (1961).

[113] B. Johs and J. S. Hale, "Dielectric function representation by B-splines," Phys. Status Solidi A **205**, 715–719 (2008).

[114] K. Postava, Y. Z. Gao, X. Y. Gong, L. Halagacka, J. Pistora, A. Nakaoka, and T. Yamaguchi, "Spectroscopic ellipsometry of anodized layer on single crystal InAsSb layer grown by melt epitaxy," Phys. Status Solidi C **5**, 1316–1319 (2008).

[115] M. Cada and J. Pistora, "Optical plasmons in semiconductors," in "Proceedings, ISMOT, Prague," (2011), pp. 20–23.

[116] H. Raether, *Excitation of plasmons and interband transitions by electrons*, no. 88 in Springer tracts in modern physics (Springer, Berlin, 1980). OCLC: 5494643.

[117] J. B. Khurgin, "How to deal with the loss in plasmonics and metamaterials," Nat. Nanotechnol **10**, 2–6 (2015).

[118] F. Chiadini, V. Fiumara, A. Scaglione, and A. Lakhtakia, "Compound guided waves that mix characteristics of surface-plasmon-polariton, Tamm, Dyakonovâ-Tamm, and UllerâZenneck waves," J. Opt. Soc. Am. B **33**, 1197 (2016).

[119] C. Fisher, L. C. Botten, C. G. Poulton, R. C. McPhedran, and C. M. de Sterke, "Efficient end-fire coupling of surface plasmons in a metal waveguide," J. Opt. Soc. Am. B **32**, 412 (2015).

[120] J. M. Sanz, D. Ortiz, R. A. de la Osa, J. M. Saiz, F. González, A. S. Brown, M. Losurdo, H. O. Everitt, and F. Moreno, "Metals for uv plasmonics," in "Research in Optical Sciences," (Optical Society of America, 2014), p. OW4D.3.

[121] J. M. McMahon, G. C. Schatz, and S. K. Gray, "Plasmonics in the ultraviolet with the poor metals Al, Ga, In, Sn, Tl, Pb, and Bi," Phys. Chem. Chem. Phys. **15**, 5415–5423 (2013).

[122] O. Takayama, L. Crasovan, D. Artigas, and L. Torner, "Observation of Dyakonov surface waves," Phys. Rev. Letters **102** (2009).

[123] L. Halagacka, M. Vanwolleghem, K. Postava, B. Dagens, and J. Pistora, "Coupled mode enhanced giant magnetoplasmonics transverse Kerr effect," Opt. Express **21**, 21741 (2013).

[124] D. A. Bykov and L. L. Doskolovich, "Numerical methods for calculating poles of the scattering matrix with applications in grating theory," J. Lightwave Technol. **31**, 793–801 (2013).

[125] L. Li, "Note on the S-matrix propagation algorithm," J. Opt. Soc. Am. A **20**, 655–660 (2003).

[126] J. Jacob, A. Babu, G. Mathew, and V. Mathew, "Propagation of surface plasmon polaritons in anisotropic MIM and IMI structures," Superlattices Microstr. **44**, 282–290 (2008).

[127] R. F. Wallis, J. J. Brion, E. Burstein, and A. Hartstein, "Theory of surface polaritons in anisotropic dielectric media with application to surface magnetoplasmons in semiconductors," Phys. Rev. B **9**, 3424 (1974).

[128] M. I. Dâyakonov, "New type of electromagnetic wave propagating at the interface," Zh. Eksp. Teor. Fiz **94**, 119–123 (1988).

[129] O. Takayama, L.-C. Crasovan, S. K. Johansen, D. Mihalache, D. Artigas, and L. Torner, "Dyakonov surface waves: A review," Electromagnetics **28**, 126–145 (2008).

[130] J. Pistora, M. Lesnak, O. Vlasin, and M. Cada, "Surface plasmon resonance sensor with a magneto-optical structure," Opt. Appl. **40**, 883 (2010).

[131] P. Darebnik, "Study and application of surface plasmons in terahertz spectral range," Master's thesis, Charles university (2016).

[132] P. Berini, "Figures of merit for surface plasmon waveguides," Opt. Express **14** (2006).

[133] T. Otsuji, "Trends in the research of modern terahertz detectors: plasmon detectors," IEEE Transactions on Terahertz Science and Technology **5**, 1110–1120 (2015).

[134] D. M. Hailu, S. Alqarni, B. Cui, and D. Saeedkia, "Terahertz surface plasmon resonance sensor for material sensing," in "Proc. SPIE," , P. Cheben, J. Schmid, C. Boudoux, L. R. Chen, A. DelĂˇge, S. Janz, R. Kashyap, D. J. Lockwood, H.-P. Loock, and Z. Mi, eds. (2013), p. 89151G.

[135] R. H. Giles, "Characterization of material properties at terahertz frequencies," Tech. rep., DTIC Document (1995).

[136] F. Harris, "On the use of windows for harmonic analysis with the discrete Fourier transform," Proc. IEEE **66**, 51–83 (1978).

[137] O. Madelung, U. RĂśssler, and M. Schulz, *Gallium arsenide (GaAs), intrinsic carrier concentration, electrical and thermal conductivity*, no. 41A1b in Landolt-BĂśrnstein - Group III Condensed Matter (Springer Berlin Heidelberg, 2002).